แบบจำลองไฟไนต์เอลิเมนต์ของพฤติกรรมเฉือนทะลุของแผ่นพื้นคอนกรีตสมรรถนะสูงมากเสริมเส้นใยเหล็กโดยพิจารณาอิทธิพลของการเรียงตัวของเส้นใย

นายตุ๊ก นู เหงียน

วิทยานิพนธ์นี้เป็นส่วนหนึ่งของการศึกษาตามหลักสูตรปริญญาวิศวกรรมศาสตรมหาบัณฑิต
สาขาวิชาวิศวกรรมโยธา ภาควิชาวิศวกรรมโยธา
คณะวิศวกรรมศาสตร์ จุฬาลงกรณ์มหาวิทยาลัย
ปีการศึกษา 2558

FINITE ELEMENT MODELING OF PUNCHING SHEAR BEHAVIOR OF ULTRA HIGH PERFORMANCE FIBER REINFORCED CONCRETE SLABS CONSIDERING EFFECT OF FIBER ORIENTATION

Mr. Thuc Nhu Nguyen

A Thesis Submitted in Partial Fulfillment of the Requirements
for the Degree of Master of Engineering Program in Civil Engineering
Department of Civil Engineering
Faculty of Engineering
Chulalongkorn University
Academic Year 2015

Thesis Title	FINITE ELEMENT MODELING OF PUNCHING SHEAR BEHAVIOR OF ULTRA HIGH PERFORMANCE FIBER REINFORCED CONCRETE SLABS CONSIDERING EFFECT OF FIBER ORIENTATION
By	Mr. Thuc Nhu Nguyen
Field of Study	Civil Engineering
Thesis Advisor	Associate Professor Withit Pansuk, Ph.D.

Accepted by the Faculty of Engineering, Chulalongkorn University in Partial Fulfillment of the Requirements for the Master's Degree

.....Dean of the Faculty of Engineering

(Associate Professor Supot Teachavorasinskun, D.Eng.)

THESIS COMMITTEE

.....Chairman

(Associate Professor Jaroon Rungamornrat, Ph.D.)

.....Thesis Advisor

(Associate Professor Withit Pansuk, Ph.D.)

.....Examiner

(Pitcha Jongvivatsakul, Ph.D.)

.....External Examiner

(Professor Piti Sukontasukkul, Ph.D.)

ตุ๊ก นู เหงียน : แบบจำลองไฟไนต์เอลิเมนต์ของพฤติกรรมเฉือนทะลุของแผ่นพื้นคอนกรีตสมรรถนะสูงมากเสริมเส้นใยเหล็กโดยพิจารณาอิทธิพลของการเรียงตัวของเส้นใย (FINITE ELEMENT MODELING OF PUNCHING SHEAR BEHAVIOR OF ULTRA HIGH PERFORMANCE FIBER REINFORCED CONCRETE SLABS CONSIDERING EFFECT OF FIBER ORIENTATION) อ.ที่ปรึกษาวิทยานิพนธ์หลัก: วิทิต ปานสุข, 117 หน้า.

การศึกษานี้นำเสนอผลการศึกษาเชิงตัวเลขของพฤติกรรมเฉือนทะลุของแผ่นพื้นคอนกรีตสมรรถนะสูงมากเสริมเส้นใยเหล็กที่ไม่มีเหล็กรับแรงเฉือนโดยพิจารณาอิทธิพลของการเรียงตัวของเส้นใยและเปรียบเทียบกับผลการทดสอบ

ปัจจุบันคอนกรีตสมรรถนะสูงมากเสริมเส้นใยเหล็กได้กลายเป็นความสำเร็จใหม่ในงานคอนกรีตเทคโนโลยีเนื่องจากคุณสมบัติเชิงกลที่ดีขึ้นวิศวกรโยธาสามารถจัดการกับปัญหาแรงเฉือนทะลุของแผ่นพื้นบางที่กำลังใช้งานอย่างกว้างขวางในอาคารต่างๆจากการศึกษาในอดีตนักวิจัยพบว่ากำลังรับแรงของวัสดุก่อนและหลังการแตกร้าวนั้นขึ้นอยู่กับการเรียงตัวของเส้นใยซึ่งจะเปลี่ยนแปลงไปตามทิศทางและวิธีการเทคอนกรีตโดยงานศึกษาในอดีตส่วนใหญ่นั้นมุ่งเน้นเกี่ยวกับผลกระทบต่อพฤติกรรมของคานแต่ในงานวิจัยนี้ได้ทำการพิจารณาผลกระทบของขั้นตอนการเทและปริมาณเส้นใยที่มีต่อพฤติกรรมเฉือนทะลุของแผ่นพื้นท้องเรียบ

แบบจำลองวัสดุถูกเสนอเพื่อจำลองผลกระทบของการเรียงตัวของเส้นใยโดยพิจารณาจากแบบจำลองจากงานวิจัยในอดีตและผลทดสอบในงานวิจัยนี้ตำแหน่งต่างๆบนแผ่นพื้นซึ่งมีระยะทางที่แตกต่างกันจากตำแหน่งเทคอนกรีตทำให้เกิดการเรียงตัวของเส้นใยที่ต่างกันส่งผลให้ใช้แบบจำลองวัสดุที่ต่างกันโดยเฉพาะแบบจำลองส่วนรับแรงดึงแบบจำลองวัสดุที่เสนอได้ใช้ในการวิเคราะห์ด้วยระเบียบวิธีไฟไนต์เอลิเมนต์ABAQUS/Explicitโดยใช้แบบจำลองคอนกรีตดาเมจพลาสติกซิตีเพื่อจำลองพฤติกรรมเฉือนทะลุของแผ่นพื้นท้องเรียบ

ความเหมาะสมของแบบจำลองวัสดุและแบบจำลองไฟไนต์เอลิเมนต์ได้รับการยืนยันด้วยการเปรียบเทียบกับผลการทดสอบส่งผลให้แบบจำลองสามารถใช้เพื่อพิจารณาผลกระทบของการเรียงตัวของเส้นใยสำหรับงานวิจัยในอนาคตและการใช้งานโครงสร้างคอนกรีตสมรรถนะสูงมากเสริมเส้นใยเหล็กต่อไป

ภาควิชา วิศวกรรมโยธา ลายมือชื่อนิสิต .....

สาขาวิชา วิศวกรรมโยธา ลายมือชื่อ อ.ที่ปรึกษาหลัก .....

ปีการศึกษา 2558

5770519021 : MAJOR CIVIL ENGINEERING

KEYWORDS: FINITE ELEMENT MODEL / PUNCHING SHEAR / FIBER ORIENTATION / UHPFRC

THUC NHU NGUYEN: FINITE ELEMENT MODELING OF PUNCHING SHEAR BEHAVIOR OF ULTRA HIGH PERFORMANCE FIBER REINFORCED CONCRETE SLABS CONSIDERING EFFECT OF FIBER ORIENTATION. ADVISOR: ASSOC. PROF. WITHIT PANSUK, Ph.D., 117 pp.

The present study represents a numerical study on the punching shear behavior of ultra-high performance steel fiber reinforced concrete (UHPFRC) slabs without shear reinforcement, particularly considering the effect of fiber orientation, validated by experimental results.

In recent decades, ultra-high performance steel fiber reinforced concrete (UHPFRC) has been a new achievement in concrete technology. Due to its superior mechanical properties, civil engineers can address the problem of punching shear of thin slabs that are currently widely used in buildings. By processing some studies, researchers have found that the strength capacity of the material before cracking and the post-cracking resistance strongly depend on the orientation of the fibers, which heavily rely on the casting direction and casting method. While most of previous studies focused on the effect on the behavior of beams, the present research particularly considers how the casting procedures as well as the volume content of the fiber affect the punching shear behavior of flat slabs.

Based on models from the previous research and this research's experimental results, constitutive model of material was proposed to capture the effects of fiber orientation. Different parts of the slab according to different distances from casting positions produce different fiber orientations, and lead to different material models, particularly tensile constitutive models. The material models were applied to finite element analysis in ABAQUS/Explicit, using Concrete Damage Plasticity model to simulate the punching shear behavior of the flat slabs.

The appropriation of proposed material models and finite element modeling procedure were validated by comparing to experimental results. Consequently, these models can be used further to consider the effect of fiber orientation in future researches and utilizations of UHPFRC structures.

Department: Civil Engineering Student's Signature .....

Field of Study: Civil Engineering Advisor's Signature .....

Academic Year: 2015

ACKNOWLEDGEMENTS

This research was carried out at the Concrete Laboratory, Chulalongkorn University. It would like to thank to the AUN/SEED-Net scholarship, International school of Engineering and Department of Civil Engineering for their essential supports.

First of all, I would like to express my deepest gratitude to my thesis advisor, Assoc. Prof. Dr. Withit Pansuk for having given me the opportunity to undertake this work and learn lots of interesting new things both in the study and daily life, for the freedom he gave me to realize my ideas, for his guidance, and for creating an excellent work environment at Concrete Laboratory during my research. I am especially grateful my Ajahn for presenting his kindness all the time, and for encouraging me in all the things I have done since the first meet.

Furthermore, I would like to thank the rest of my thesis defense committee: Assoc. Prof. Dr. Jaroon Rungamornrat, Prof. Dr. Piti Sukontasukkul, and Dr. Pitcha Jongvivatsakul for the time and the effort they put into reading and judging the thesis and for their valuable comments.

Many thanks are also due to all of my friends at Concrete Laboratory for the friendship and the pleasant atmosphere you all have created. Every member of this laboratory have be a great family and company. All of the memories we made will always come by and bring me a smile. In this context, I would also express my thank to Mr. Thi and Ms. Chung for their kind help, valuable advice and encouragement me during my study.

I owe words of appreciation to Dr. Dinh The Hung from Ho Chi Minh city University of Technology for his first help and continuous support throughout these years. His thoughtful efforts have given me the opportunity to study in Chulalongkorn University.

I give specials thank to all of my Vietnamese friends here in Ratchathewi Apartment and Chulalongkorn University. I could never feel at home without them. Their companionship during these all years means so much for me that I cannot express here in one page. In addition, I wish to express my thanks to Ms. Thao for her helps and encouragements even in the hardest time.

Finally, I owe the greatest thanks to my parents and my siblings. I know without your unconditional love, support and encourage, I wouldn't have been able to make it this far.

CONTENTS

Page

Page

Page

LIST OF TABLES

LIST OF FIGURES

CHAPTER 1

INTRODUCTION

1.1. Background

Reinforced concrete slabs have been used in a variety of structural engineering applications; many types of slabs have been designed to be suitable for each type of structure. Flat slab is a type of slabs, used by engineers in many buildings due to its advantages over other reinforced concrete floor systems. The most important advantages of flat slabs are: reduction in building height, increase the used space, ease of formwork installation and reinforcement placement. The capacity of a reinforced concrete flat slab is demonstrated by its punching shear strength. It is brittle failure and can lead to collapses of the entire structure. Several ways can be used to increase the punching shear capacity of flat slabs such as increasing slab thickness, constructing drop panels and/or column heads or both, using a high strength concrete, placing shear reinforcement in the punching shear zone and adding discrete fibers. Some of them can be combined with design to reach the expected slabs.

Ultra-high performance steel fiber reinforced concrete (UHPFRC) have developed to design structural elements in combination properties of self-compacting, fiber reinforcing and ultra-high strength. The mechanical characteristics of UHPFRC are improved not only in strength and ductility under compression, but also in tensile strength and ductility under tensile loading. Although many researches have been performed to investigate the properties of UHPFRC members, the shear behavior, especially in punching shear for slabs remain largely unknown.

In actual construction, concrete can be cast in any positions of structures, as shown on Figure 1.1. For conventional concrete, this kind of issue does not effect to the behavior of structures. But for FRC composites, particularly for UHPFRC, with adding fiber and self-compacting properties, fiber become a main factor effect to properties

of structures as fiber volume content or fiber orientation which affected by casting positions and direction. So with each kind of structure, each casting method lead to different behavior and capacity. Hence, researchers and engineers need to find out and capture these effects in design and construction application. And many experiments were conducted to show that fiber orientation, casting position and flow of fresh concrete were significant impact on creating behaviors of the composites structures. But the punching shear behavior has not been figured out.

Figure 1.1: Casting method applied in real constructions

In actual construction, concrete can be cast in any positions of structures, as shown on Figure 1.1. For conventional concrete, this kind of issue does not effect to the behavior of structures. But for FRC composites, particularly for UHPFRC, with adding fiber and self-compacting properties, fiber become a main factor effect to properties of structures as fiber volume content or fiber orientation which affected by casting positions and direction. So with each kind of structure, each casting method lead to different behavior and capacity. Hence, researchers and engineers need to find out and capture these effects in design and construction application. And many experiments were conducted to show that fiber orientation, casting position and flow of fresh concrete were significant impact on creating behaviors of the composites structures. But the punching shear behavior has not been figured out.

To add more experimental knowledge to this matter, in this study, the punching shear of the slabs was investigated with various casting directions and volumes of fiber to consider the effect of fiber distribution and orientation. The fiber orientation

significantly effects to tensile behavior of UHPFRC. By controlling the casting position and direction, the fiber orientation and distribution in slabs was different, it led to the different in characteristic, especially in the punching shear strength of each slab.

By applying to the concrete damage plasticity (CDP) model in ABAQUS, the finite element method was used to simulate the UHPFRC slabs, the punching shear resistance of slabs from the model were compared with the experimental result. ABAQUS package is based on finite element method, can be used to solve both static and dynamic problems by linear or nonlinear analysis. CDP is one of the concrete models, uses the concepts of isotropic damaged elasticity in combination with isotropic tensile and compressive plasticity to represent the inelastic behavior of concrete.

The UHPFRC slab is composed of three main materials: concrete, steel reinforcement and steel fiber, with different material properties. Depending on the application, all materials, especially concrete, behave nonlinear. Cracking of concrete is the key foundation of material nonlinearity, and usually happens at lower levels of applied load because of low resistance in tensile stresses of concrete. Therefore, to capture the actual behavior of UHPFRC slabs, nonlinear models should be used. Another problem is how to simulate the properties of this material in differences of fiber distribution by changing the casting position and direction as mentioned above.

1.2. Research objective and scope

The objectives of this study are as follows:

- To provide the procedure and input required parameters to utilize commercially available software to simulate UHPFRC, especially in UHPFRC flat slabs. The material models will be introduced to capture the nonlinear properties this material and the effect of fiber orientation.
- To validate the finite element model in the commercial software of Concrete Damage Plasticity model in ABAQUS/Explicit.

- Using the CDP model to investigate the punching shear behavior of UHPFRC slab with low volume of fiber if changing fiber orientation and casting position.

To get the above objective, this research will perform:

- From experimental results and previous researches, determining properties parameters of each material: tensile strength, compressive strength, Young's modulus, Poisson's ratio of concrete, and the stress-strain curve of steel bar in tensile.
- Determining the appropriate nonlinear material models for UHPFRC from previous researches, controlled by experimental results, to present the compression, tension hardening and softening model which can capture the effect of fiber volume, fiber distribution and orientation.
- Using concrete damage plasticity (CDP) model in ABAQUS/Explicit to simulate UHPFRC slabs under concentrated loading and punching shear failure.
- The results from the model will be compared to experimental results, including ultimate load, load-displacement behavior, cracks pattern, and strain in reinforcing steel.
- Changing fiber orientation corresponding to distance from casting position to figure out the effect of fiber orientation.

1.3. Thesis organization

This Master-thesis consists of five chapters; its structure is shown in Figure 1.2. Start of each chapter is an introduction part to introduce and literature the whole information of the chapter, and following by sub-chapters which concentrate in main detail of chapter. **Chapter 1** provides background, objective and scope, and summary outline of the research.

In **Chapter 2**, previous researches relate to research purpose of this study are presented and summarized, including mechanical properties of UHPFRC and its constitutive model using for analysis, how is effect of fiber orientation to these models, and finally is the finite element models for punching shear behavior of slabs.

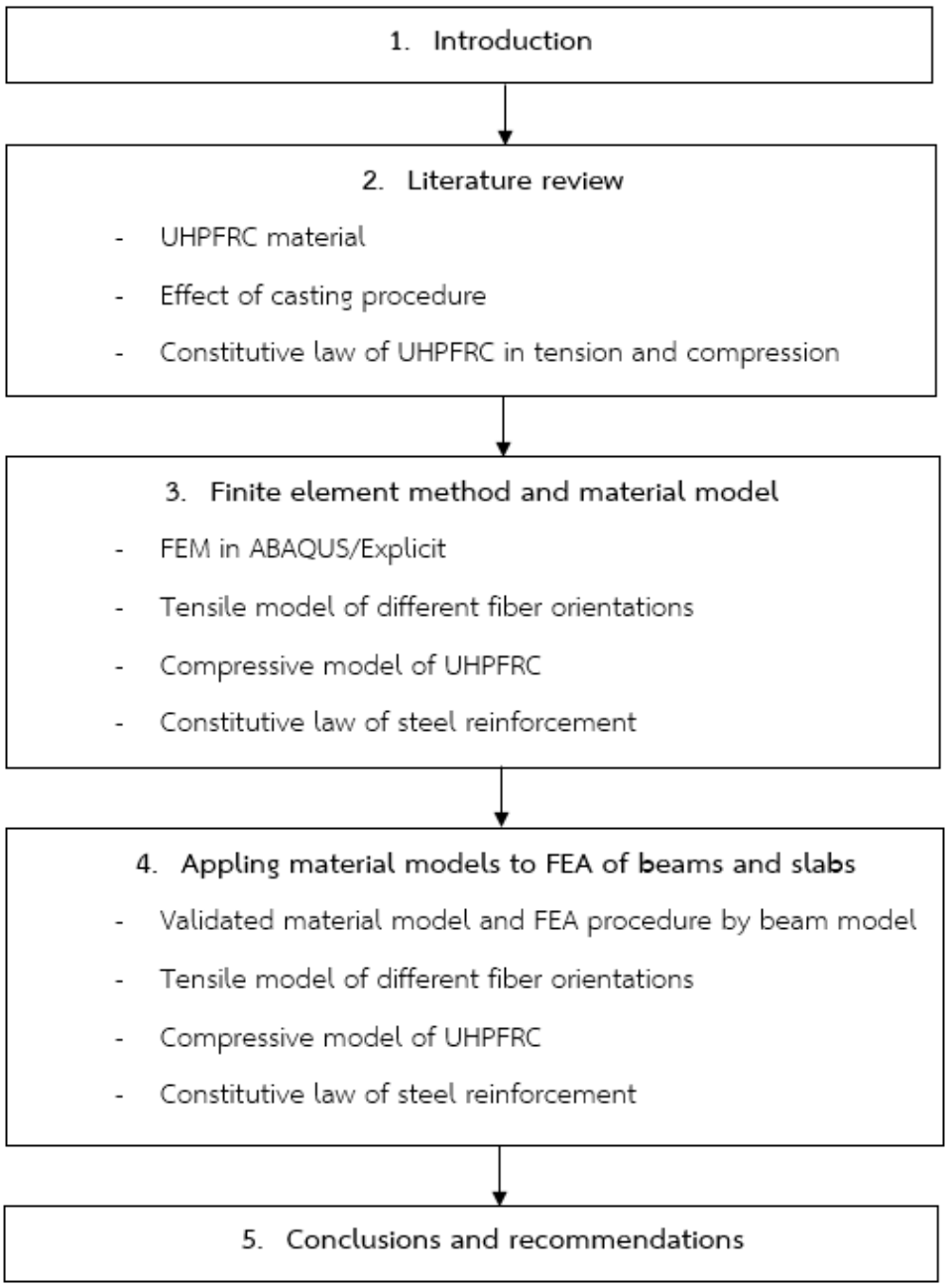

Figure 1.2: Structure of Master-Thesis

In **Chapter 3**, finite element method applied in ABAQUS/Explicit and material model of UHPFRC are detailed. This part describes how ABAQUS/Explicit solve the problem, including concrete damage plasticity model (CDP) and its applied finite element method. Furthermore, material model that applied to model in next part are introduced and proposed, such as tensile model of different fiber orientation, compressive behavior of UHPFRC, and constitutive model of tensile steel reinforcement.

Chapter 4 shows applying finite element analysis in ABAQUS/Explicit to simulate behavior of the beams and slabs. Firstly, material model which proposed before were used for modelling of beam to validate the accuracy of that model. Then, that model would be applied to simulate the punching shear behavior of slabs to consider the effect of casting positions and fiber orientations. Finally, the slab models will be developed for parametric studies.

In **Chapter 5**, the conclusions on the effect of casting position or fiber orientation on punching shear behavior of slabs will be made. Based on the results of this research, the recommendation in modelling and utilization of that effect on UHPFRC will be provided as well.

CHAPTER 2

LITERATURE REVIEW

2.1. Introduction

UHPFRC is Advance Cementitious Materials (ACM) with specifically tailored properties. UHPFRC has its place in the group of High Performance Fiber Reinforced Cement Composites (HPFRCC). HPFRCC is a kind of Fiber Reinforced Concrete (FRC) that present strain-hardening properties in tensile behavior of material. Furthermore, UHPFRC with a dense matrix consequently show a very low permeability that compared to ordinary concretes and HPFRCC [1].

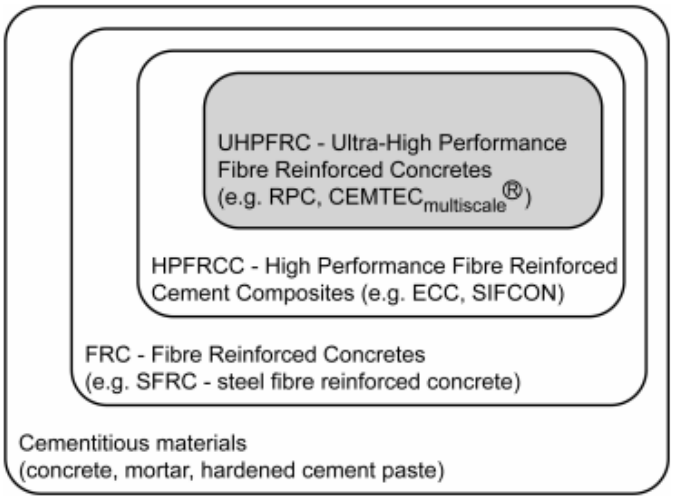

Figure 2.1: Definition of UHPFRC [1]

By the time, many studies have been carried out to investigate the properties and utilizable abilities of UHPFRC in construction. The mechanical characteristic of this material shown a good behavior, especially in tensile behavior.

2.2. Mechanical properties of UHPFRC

The mechanical properties of UHPFRC are presented in this subchapter, such as compressive and tensile behavior, modulus of elasticity, shear strength and bond strength through the previous researches.

2.2.1. Compression properties

Improved from HSRC and SFRC, UHPFRC reach a very high compressive strength- typical values in excess of 150 MPa at 28 days without heat treatment. Because of that, Young's modulus is also high: E= 45 to 65 GPa at 28 days. In another study, it has been reported that the Young's modulus of RPC paste can rise to 75 GPa for very high paste densities, in comparison to approximately 30 GPa achieved in ordinary cement pastes [2].

Normally, the compressive properties are tested by uniaxial compressive test of cylinders or cubes. From this test, compressive strength, ultimate strain, stress-strain relationship in compression or modulus of elastic is determined directly. Many previous studies also derived the relation of modulus of elasticity and compressive strength based on the experimental result, this expression is useful to get modulus of elastic in design. Some of this relationship expressions presented after in this section.

UHPFRC is combined HSC with FRC, so it has a high strength from HSC and increase the ductility under compression because of adding fiber from FRC. By creating the new mixture from them, it makes UHPFRC improve mechanical strengths, fracture, toughness, and durability.

From stress-strain curve shown in Figure 2.2 shown that UHPFRC not only significantly increase in strength when comparing to OC and HSC, but also improve the post peak behavior, as mentioned, it is because of the improvement in the ductility property of UHPFRC.

The compressive strength is slightly improved by fiber addition. An increase of 5-10 % in average compressive strength for fiber quantities of up to 4% V_f is reported in previous researches [3]. Following [Spasojevic 2008], the compressive strength is

reached at a strain in the range of 3-5 ‰. The post-peak behavior is mainly influenced by fiber content, fiber type and interaction of fibers and matrix.

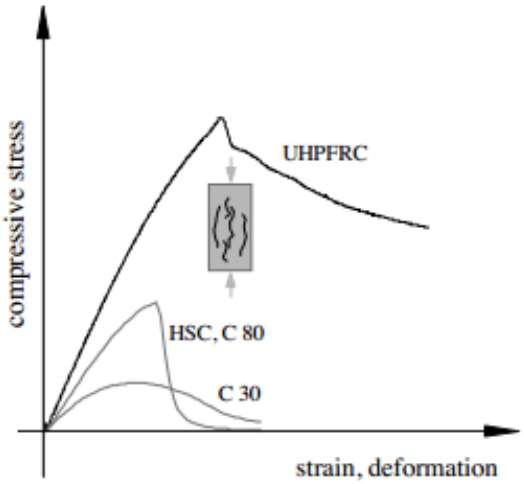

Figure 2.2: Typical response of UHPFRC in compression in comparison to normal strength and high-strength concrete [3]

Stress-strain relationship

Carreira (1985) proposed the comprehensive stress-strain relationship for unconfined normal strength concrete, this equation satisfies all the conditions previously stated [4].

$$\sigma_c = f_c^{'} \frac{\beta.\eta}{\beta - 1 + \eta^{\beta}} \tag{2.1}$$

$$\beta = \frac{1}{1 - \frac{f_c^{'}}{\varepsilon_0 . E_{it}}} \; ; \; for \; \beta \geq 1 \; and \; \varepsilon \leq \varepsilon_u \tag{2.2}$$

After Carreira (1985), many researchers modified that expression to more accurately predict their experimental results for SFRC or HSFRC. The difference in type of fibers, volume fracture of fibers and the aspect ratio of fibers were considered in each research, therefore, they got a slight difference in their proposal. And most of them were expressed in term of the measured compressive strength of their UHPFRC mixture. The following table shows the modified stress–strain relationship equations in the literature.

Table 2.1: The literature overview of the compressive stress-strain model

Researcher	Models	Parameters
Ezeldin *et al.* (1992) [5]	$\sigma_c = f_c^{'} \frac{\beta.\eta}{\beta - 1 + \eta^{\beta}}$ $f_c^{'} = f_{cp}^{'} + 11.232RI$ $\beta = 1.093 + 0.2429RI^{-0.926}$ $E_c = E_{cp} + 9936RI$ $\varepsilon_0 = \varepsilon_{0p} + 1427 \times 10^{-6} RI$	$f_c^{'}$ is the measured compressive strength; E_{cp}, $f_{cp}^{'}$, ε_{0p} are the modulus of elasticity, compressive strength, and corresponding strain of plain concrete, respectively.
Hsu and Hsu (1994) [6]	$\sigma_c = f_c^{'} \frac{n.\beta.\eta}{n\beta - 1 + \eta^{n\beta}}$ for $0 \le \eta \le \frac{\varepsilon_d}{\varepsilon_0}$ $\sigma_c = f_c^{'} \frac{n.\beta.\eta}{n\beta - 1 + \eta^{n\beta}}$ for $\eta \ge \frac{\varepsilon_d}{\varepsilon_0}$ $\beta = \left(\frac{f_c^{'}}{11.84(100V_f)^3 + 58.61} \right)^3 - 26V_f + 2.74$ $E_{it} = a_2 f_c^{'} + C_2$ $\varepsilon_0 = a_1 f_c^{'} + C_1$	$f_c^{'}$ is the measured compressive strength; n is a material parameter, depends on the strength of material; ε_d is the strain at $0.6 f_c^{'}$ in the descending; a_1, a_2, C_1 and C_2 are constant, given in research.
Mansur *et al.* (1999) [7]	$\sigma_c = f_c^{'} \frac{\beta.\eta}{\beta - 1 + \eta^{\beta}}$ for $0 \le \eta \le 1$ $\sigma_c = f_c^{'} \frac{k_1.\beta.\eta}{k_1\beta - 1 + \eta^{k_2\beta}}$ for $\eta \ge 1$ Where, $\beta = \frac{1}{1 - \frac{f_c^{'}}{\varepsilon_0.E_{it}}}$ $E_{it} = \left(10300 - 40000V_f\right) f_c^{'1/3}$ $\varepsilon_0 = \left(0.0005 + 0.000072RI\right) f_c^{'0.35}$	$f_c^{'}$ is the measured compressive strength; k_1, k_2 are constant, difference in cylindrical specimens and horizontally cast prisms.

Researcher	Models	Parameters
Nataraja *et al*. (1999) [8]	$\sigma_c = f_c^{'} \frac{\beta.\eta}{\beta - 1 + \eta^{\beta}}$ $f_c^{'} = f_{cp}^{'} + 6.9133RI$ $\beta = 0.5811 + 0.8155RI^{-0.7406}$ $\varepsilon_0 = \varepsilon_{0p} + 0.00192RI$	$f_c^{'}$ is the measured compressive strength; $f_{cp}^{'}, \varepsilon_{0p}$ are the compressive strength and corresponding strain of plain concrete, respectively.
*Note: $RI = V_f l_f / d_f$; V_f is volume fraction of fibers; l_f / d_f is aspect ratio of fibers.		

In the Table 2.1, Nataraja *et al*. [8] proposed the stress-strain curve in compression for SFRC with compressive strength ranging from 30 to 50 MPa, fibers were used with three dosages of 0.5%, 0.75% and 1.0%. Testing with the same volume fraction of fibers, the empirical equation of Hsu and Hsu [6] represented the complete stress-strain relationships of HSFRC with compressive strength exceeding 10,000 psi (70 MPa). Mansur *et al*. [7] also provided the equation for HSFRC, the compressive strength ranges from 70 to 120 MPa, different percentages of steel fibers is considered in this study. While equation of Eldin *et al.* [5] were proposed for both SFRC and HSFRC, tested with difference in volume fraction of fibers. The aspect ratio was considered to empirical equations in most of the study, shown the effect of this factor to compressive stress- strain relationship.

In 1989, based on the experimental results, Soroushian and Lee proposed compression stress-strain relationship for SFRC, it included a curvilinear ascending branch and then a bilinear descending part:

$$\sigma = -f_c^{'}\eta^2 + 2f_c^{'}\eta \text{, for } \eta \le 1 \quad (2.3)$$

$$\sigma = z(\eta - 1)\varepsilon_0 + f_c^{'} \ge f_0 \text{, for } \eta > 1 \quad (2.4)$$

Where: $f_c^{'} = f_{cp}^{'} + 3.6RI$; (2.5)

$$f_0 = 0.12f_c^{'} + 14.8RI; \quad (2.6)$$

$$z = -343f_{cp}^{'}\left(1 - 0.66\sqrt{RI}\right) \le 0; \quad (2.7)$$

$$\varepsilon_0 = 0.0007RI + 0.0021; \quad (2.8)$$

This empirical relationship is also expressed in term of the measured compressive strength, the strain corresponding to the maximum stress, the volume fraction of fibers and the aspect ratio.

In 1999, Barros and Figueiras [9] proposed other formula for SFRC with hook-end fibers. The relationship is represented by the following equation:

$$\sigma_c = f_c^{'} \frac{\eta}{(1-p-q)+q\eta+p\eta^{(1-q)/p}} \quad (2.9)$$

$$q = 1-p-\frac{E_c}{E_{cp}},\ p+q \in]0,1[,\ \frac{1-q}{p} > 0 \quad (2.10)$$

Where, ***p*** is calculated based on results from their experiment, and in this study, it depends on the type of fiber and fiber dosage.

Modulus of elastic

As mentioned above, the modulus of elasticity can be calculated by the empirical equations in relationship with compressive strength. Eq. 2.11, 2.12, 2.13 were proposed by ACI Committee 318 [10], ACI Committee 363 [11] and Ma et al. [12] respectively.

$$E = 4730\sqrt{f_c^{'}} \quad (2.11)$$

$$E = 3320\sqrt{f_c^{'}} \quad (2.12)$$

$$E = 19,000\sqrt[3]{\frac{f_c^{'}}{10}} \quad (2.13)$$

Eq. 2.11 presents the simplest and most widely relationship that used for plain concrete. While for concretes up to 83 MPa, modulus of elastic can be determined Eq. 2.12, and Eq. 2.13 was proposed by Ma *et al.* which can be used for UHPFRC containing no coarse aggregates.

In another study, to represent behavior of UHPFRC at strength above 25 MPa, Graybeal [13] adjust the scalar factor in Eq. 13 to a value shown in Eq. 16 as follows [13].

$$E = 3840\sqrt{f_c'} \quad (2.14)$$

Poisson's ratio

For other parameters, the Poisson's ratio of UHPFRC was reported in some researches. In the report of Celik Ozyildirim [14], the values of Poisson' ratio of UHPC were from 1.7 to 2.0, the average value is 1.8. In another study of Eldin [15], this value is around 2.0 and not change much for concrete with compressive strength ranging from 124 to 151 MPa.

2.2.2. Tensile properties

The tensile behavior shows a big improvement of UHPFRC when comparing to HSC and FRC. Adding fiber to concrete help concrete increase resistance after cracks occur, so the softening branch represent that property in FRC. Up to UHPFRC, after first crack, the stress keeps increasing in strain- hardening branch. The Figure 2.3 shown the difference between FRC, HSFRC, ECC and UHPFRC.

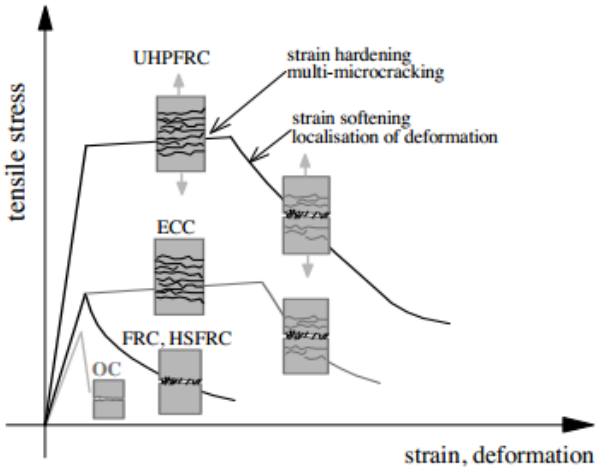

Figure 2.3: Typical behavior of UHPFRC in tension in comparison to the other types of concrete and composites [3].

HSFRC and FRC are undergoing strain softening suddenly after the first cracks while ECC and UHPFRC present strain hardening behavior. In addition, UHPFRC distinct from ECC by the advance of very high tensile strength.

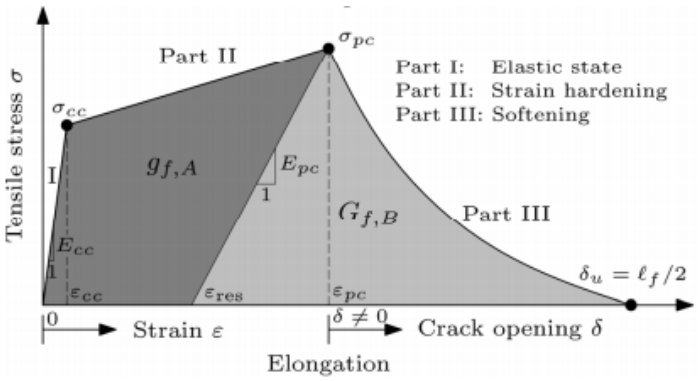

Figure 2.4: Stress- strain tensile idealized model [16]

For the design model, the tensile behavior of UHPFRC can be represented in three main parts [17]:

- Part I: **strain based elastic part**, determined by the initial tensile behavior up to cracking strength $\boldsymbol{\sigma_{cc}}$, which is defined as an assumed point of transition from ideal linear elastic to best fitted linear strain-hardening behavior, and determined by the associated strain $\boldsymbol{\varepsilon_{cc}}$ and the elastic modulus E_{cc};
- Part II: **strain based strain hardening part**, determined by increasing stress after first crack until post-cracking strength $\boldsymbol{\sigma_{pc}}$, associated with strain $\boldsymbol{\varepsilon_{pc}}$. Therefore, the post-cracking strain of UHPFRC is higher than the cracking strength. During this stage, multiple cracks occur, however, the macroscopic deformation is still uniform, and can be expressed by the strain $\boldsymbol{\varepsilon}$ [1];
- Part III: **crack opening based softening part**, crack localization occur and softening behavior is observed [1]. Normally, the stress-crack opening is used to represent this stage.

The tensile behavior of UHPFRC is affected by the quantity and properties of the fibers, their interaction between the fiber and matrix, and the fiber distribution and orientation. A further increase of the fiber quantity leads to a further increase of tensile behavior [18], presented in figure 2.5.

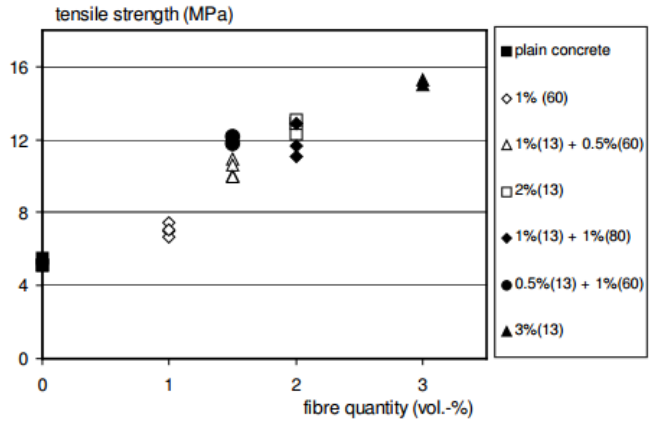

Figure 2.5: Uniaxial tensile strengths of the applied concretes with one or two different types of fibers [18]

Consider the effect of types of fibers, in research of Wille et al. [19] and Park et al [20], twisted fibers showed the better tensile behavior comparing to hooked fibers and smooth fibers with same volume fraction of fibers.

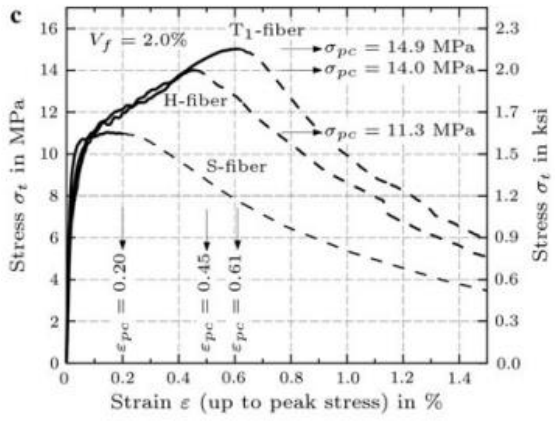

Figure 2.6: The tensile response of UHPFRC mixes with different types of fibers [19]

Stress-strain relationship in tension

Taking into account the effect of fiber content, based on RILEM TC 162-TDF (2002) [21], Barros (2005) and Tlemat (2006) performed the inverse finite element analysis to fit with their experimental results.

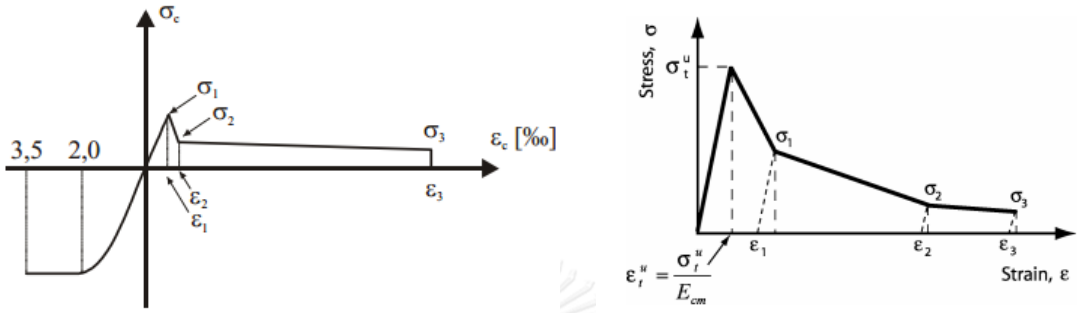

(a) (b)

Figure 2.7: Stress-strain diagram (a) from RILEM TC 162-TDF and (b) Tlemat (2006)

Besides the design curves in recommendation, many other researchers study in this problem. Naaman et al. 2006 [22] suggested the generalized typical stress-elongation of FRC composites for modeling purposes. The curve is modeled by multiple linear curves, including seven main points.

In this study, analytical expressions were developed to predict the stress at first cracking (point 1) and at ultimate post-cracking (point 3). At point 1, the coordinates can be estimated by one of the following equations:

$$\begin{aligned} &\sigma_{cc} \approx \sigma_{mu} \\ &\varepsilon_{cc} \approx \varepsilon_{mu} \approx 0.0002 \\ &\sigma_{cc} \approx E_c \varepsilon_{cc} \\ &\sigma_{cc} = \sigma_{mu}\left(1-V_f\right) + \alpha \bar{\tau} V_f \frac{l_f}{d_f} \end{aligned} \qquad (2.15)$$

In which: σ_{mu} is the tensile strength of plain concrete, ε_{mu} is the tensile strain of unreinforced matrix at peak stress, E_c is the elastic modulus, $\bar{\tau}$ is the average bond strength at the fiber-matrix interface and α is the product of several coefficients.

The researcher also suggested the minimum strain capacity at peak stress, ε_{pc}, should be equal or exceeding 0.5%, to ensure that the strain-hardening FRC composite contribute sufficiently to the nominal resistance and to ductility, while inducing significant multiple cracking along the ascending part of the load-elongation response of the member [22].

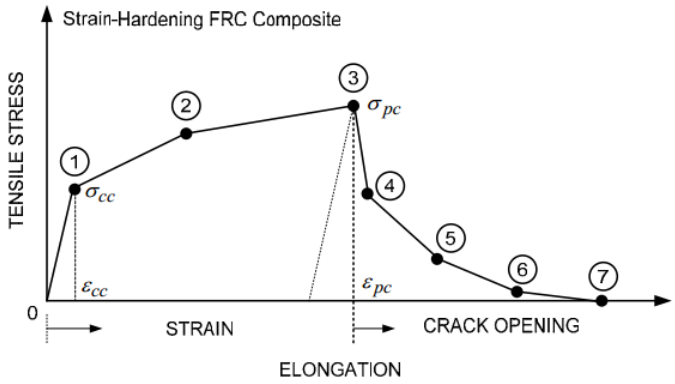

Figure 2.8: Generalized typical stress-elongation response of FRC composites suggested for modeling purposes [22]

After Naaman (2006), Wille et al. (2011) [19] and Wille et al. (2014) [17], continued to perform many experiments and proposed the accurate expressions for stress-elongation relationship of their UHPFRC mixture with different types of fibers and volumes fraction of fibers. The idealized relationship was shown in Figure 2.4, which simplified from their previous research, defined by only three points. Elastic state is up to cracking strength σ_{cc} which represent the development of micro cracks and activation of fibers. After cracks occurred, strain hardening behavior start with inelastic strain and multiple cracking until the material reaches the peak at σ_{pc}. Finally, softening part shown reduction of tensile stress from σ_{pc} to 0. Cracking strength σ_{cc} is affected by the tensile strength of the matrix, type and dosage of fiber.

$$\sigma_{cc} = \sigma_{ct} + \alpha\tau V_f \frac{l_f}{d_f} \tag{2.16}$$

Where: σ_{ct} is the tensile strength of the matrix only, and $\alpha\tau$ is a combination of fiber group effect and bond behavior before cracking.

Same as cracking strength, elastic modulus was calculated from elastic modulus of matrix and steel fiber:

$$E_{cc} = (1 - V_f)E_c + V_f E_s \tag{2.17}$$

The post-cracking tensile strength can be predicted by following equation:

$$\sigma_{pc} = \lambda \times \tau \times \frac{l_f}{d_f} V_f \tag{2.18}$$

Where: **λ** is the group effect, averaged embedded length, fiber orientation and spalling effect during the pull out of largely inclined fibers. In this research, it mainly represents the effect of averaged embedded length and group effect.

The strain corresponding to post- cracking strength, ε_{pc}, is observed from experimental results.

For the softening curve, Spasojevic (2008) [3] proposed the expression for stress- crack opening curve which come up from the empirical model of Stang (1992) [23]:

$$\sigma(w) = \sigma_{pc} \times \frac{1}{\left(1 + \frac{w}{w_{n,w}}\right)^p} \tag{2.19}$$

Where both parameters, w_n and p, were determined from data fitting.

2.3. Orientation of fiber and its effect on structural behavior

Mechanical properties of UHPFRC are greatly linked to the fiber content, types of fibers, fiber distribution and orientation, etc. ; adding fiber to the matrix improve the tensile behavior and enhancement of toughness [24], and fiber distribution and orientation significantly affect the tensile behavior of material [25]. Many researches performed the experiments relate to fiber distribution and orientation, to better understand about the methods to determine and what effect to fiber distribution and

orientation, also clearly what it effect to mechanical properties of FRC composites [25-30].

Ferrara (2010) [31] exploited the correlation among fresh state performance, fiber distribution and strain hardening properties of FRCC for the intended application at an industrial level. Slab-specimens, with dimensions 1 x 0.5 x 0.03 m, were cast, with fresh concrete flowing parallel either to their long and short side. From those slabs, beams were then sawn with their axis either parallel or vertical to the flow direction.

The beams were bended in 4-point bending to inspect the effect of fiber distribution, if any. The schematic of the slabs in casting and beam sawing are shown in Figure 2.9 as follows.

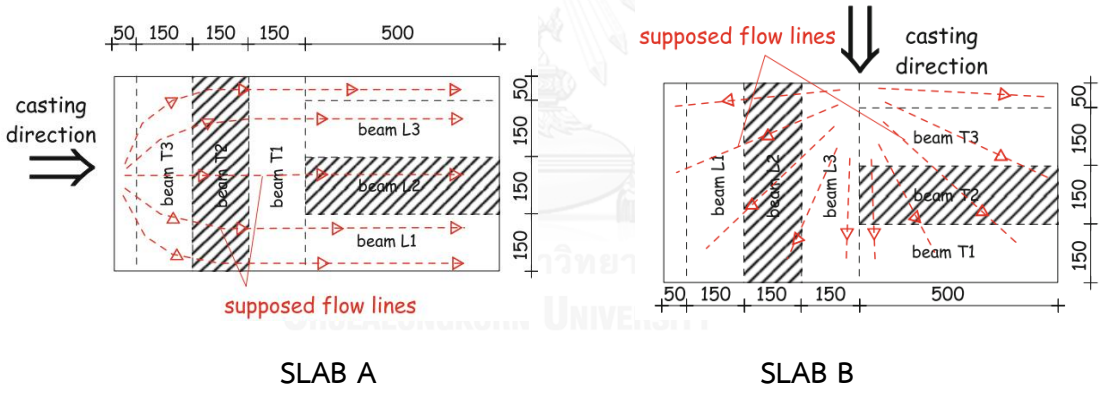

Figure 2.9: Schema of the slabs include casting direction and beam sawing [31]

Figure 2.10 shows results from 4-point bending test of sawn beams. The results had clearly shown the positive of orienting the fibers along the casting flow direction which effected to mechanical properties. For slab A, where the slab was filled to formwork in a direction parallel to the long side of the slab, fibers likely align to casting direction.

As the results, the beams, which cut with their axis parallel to casting direction were demonstrated significant improvement in flexural behavior with strain-hardening

and higher bending load capacity, compared to the beam cut with their axis perpendicular to flowing direction. For slab B, there were not much different among the beam because of the radial spread of fresh concrete when they filled to formwork at the middle of the long side of slab.

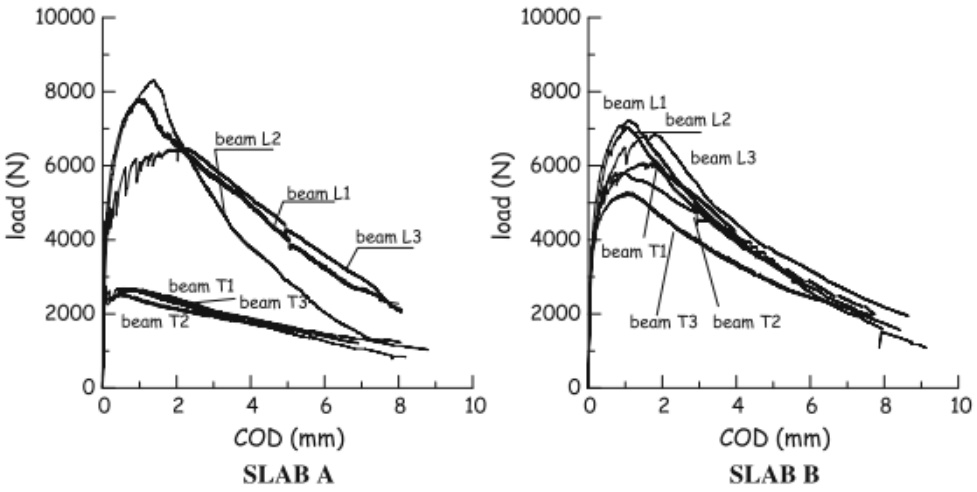

Figure 2.10: Load-COD curves from beams tests [31]

In other research, Barnett (2010) [32] investigated the distribution and orientation of fibers in UHPFRC panels with 2% of fiber, which cast in three different manners: poured at a single point at the center of the panel, poured into the mold at several points around the perimeter of the panel, and, poured randomly (as shown in Figure 2.11).

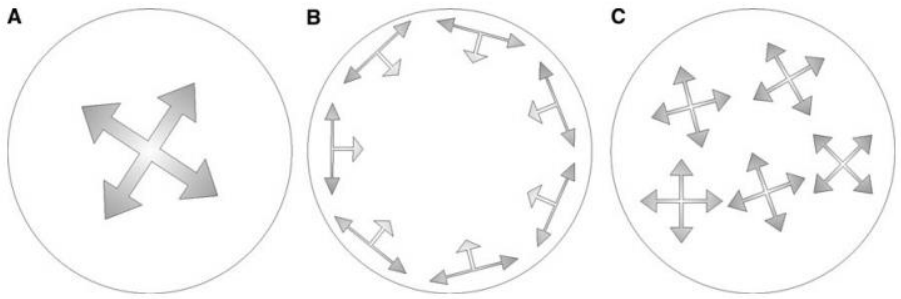

Figure 2.11: Schematics of flow of concrete according to casting methods. **A** Centre. **B** Perimeter. **C** Random

Round-panel specimens 550 mm in diameter and 25 or 50 mm thick were manufactured for these tests. This study used nondestructive electrical resistivity technique to qualitatively investigate the distribution of fibers in the panels, and controlled by direct observation of fibers with X-ray CT imaging. The results were shown in Figure 2.12, drew fiber orientation of each slab equivalent to each casting method. It clearly demonstrated that fiber tended to align parallel to flowing direction.

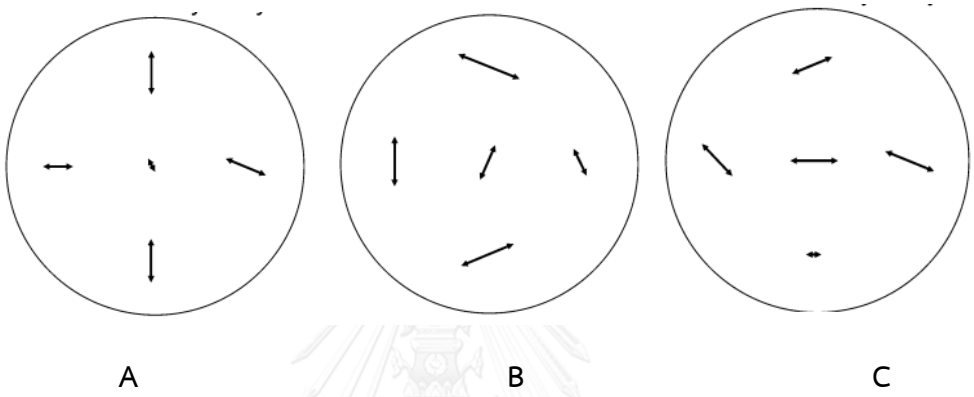

Figure 2.12: Fiber orientation induced in each type of slabs

To check mechanical properties of the material and effect of induced fiber orientation, the round slabs were bended under concentrated loading at the middle of slabs, following the procedure of ASTM C1550. The load-deflection responses observed from the test are shown in Figure 2.13. It clearly demonstrated that the slabs cast at middle shown the best performance with the highest load capacity and ductility of the panels. It was explained by that the better distribution and orientation of fiber led to increase the total number of fibers bridging the radial cracks formed during loading.

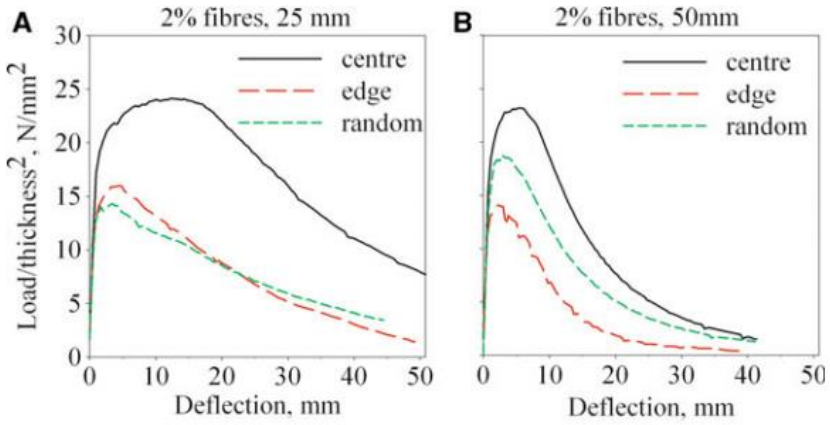

Figure 2.13: Load-deflection curves from flexural test

In Tanikella's study, a slab of length 5.3 m, width 4m and a thickness of 10 cm was cast by pouring fresh SCC from one corner of the slab. Specimens were sawn from the slab (as schema in Figure 2.15) and counted fibers in each to fiber the distribution of fiber. The result showed that fiber distribution cannot be assumed as uniform, and it was affected by many factor such as flow of concrete and disturbance of the casting process for large scale specimen. The research also observed flow of SCC in the full scale slab as shown in Figure 2.14.

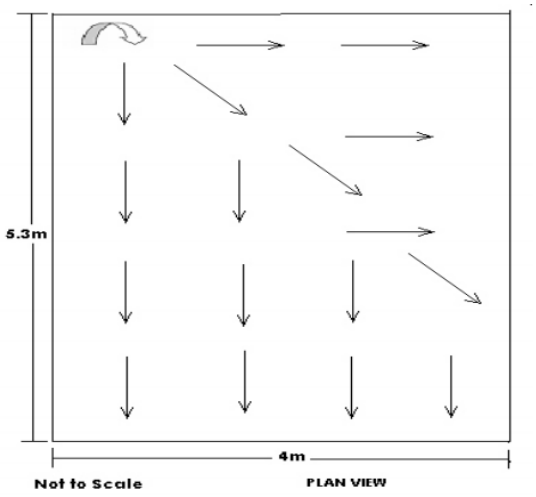

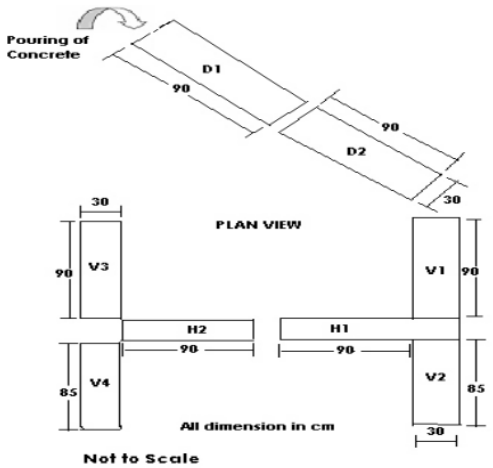

Figure 2.14: Observed flow of SCC

Figure 2.15: Sawn specimens from the slab

2.4. Tensile model in consideration of fiber distribution

Mechanical properties of UHPFRC are greatly linked to the fiber content, types of fibers, fiber distribution and orientation, etc. ; adding fiber to the matrix improve the tensile behavior and enhancement of toughness [24], and fiber distribution and orientation significantly affect the tensile behavior of material [25]. Many researches performed the experiments relate to fiber distribution and orientation, to better understand about the methods to determine and what effect to fiber distribution and orientation, also clearly what it effect to mechanical properties of FRC composites [25-30]. And theoretical studies regarding the effect of fiber orientation also investigated to find the correlation between fiber distribution and tensile properties in post- crack stage [33-35], or both pre- crack and post crack stage [24, 36].

Relating to the theoretical studies, the ideal of consideration fiber bridging action based on the study of **Li (1993)** [34]. In this research, the composite bridging stress is estimated by combining aggregate bridging, fiber bridging and the pre-stress already present in fibers before cracking. The formula is shown as follows, Figure 2.16 show the contribution of each part of the model.

$$\sigma_c(w) = \sigma_a(w) + \sigma_f(w) + \sigma_{ps}(w) \tag{2.20}$$

Where: $$\sigma_a(w) = \sigma_{mu} \times \frac{1}{1+\left(\frac{w}{w_{n,w}}\right)^p} \tag{2.21}$$

$$\sigma_f(\delta) = \frac{4V_f}{\pi d_f^2} \int_{\theta=0}^{\pi/2} \int_{z=0}^{L_f/2} P(\delta)\, p(\theta)\, p(z) dz d\theta \tag{2.22}$$

$$\sigma_{ps}(w) = \sigma_{ps}^0 (\mathrm{w}^* - w) / \mathrm{w}^* \tag{2.23}$$

In which, $\sigma_a(w)$ is the aggregate bridging stress, $\sigma_f(w)$ is fiber bridging stress; θ is the orientation angle and z is the centroid distance from the matrix crack. The value of

fiber bridging stress depends on the orientation of fibers, therefore, fiber orientation affects the tensile behavior of FRC composites.

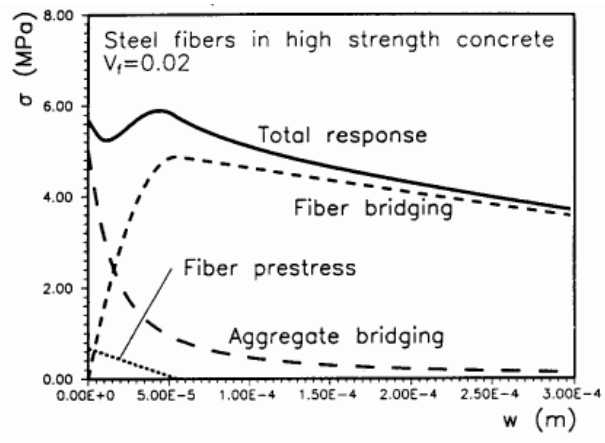

Figure 2.16: Contribution of three parts of model

Based on the research of Li (1993), and combined with experimental results, Wuest (2007) [37, 38] developed a model to predict tensile hardening response of UHPFRC. After reached agreement with experimental results, fiber orientation parameter was considered as a parametric study (Figure 2.17).

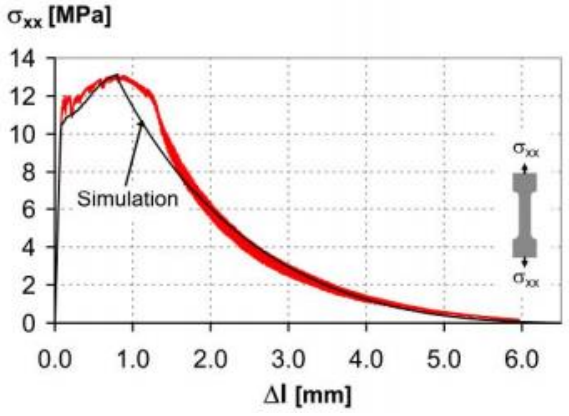

Figure 2.17: Simulation results compared to experimental results

In 2013, from experiment results and previous research, **Delso et al.** [36] proposed the empirical tensile model based on fiber orientation for UHPFRC with 4% content of fibers.

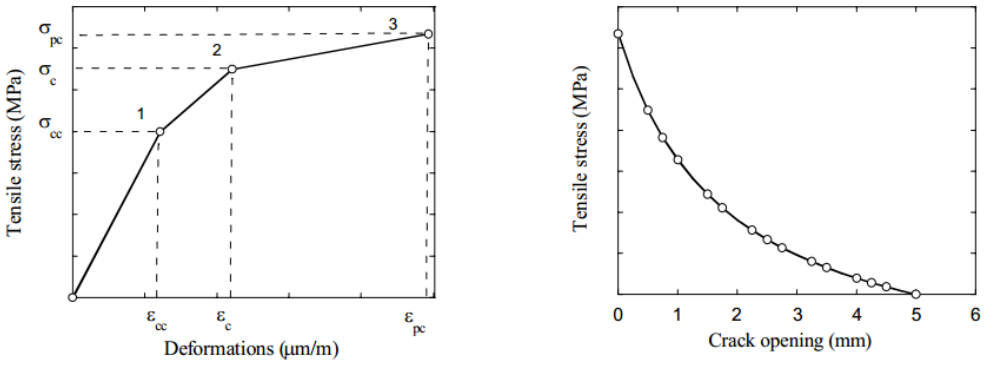

Figure 2.18: Empirical tensile model: (a) Pre- peak behavior, b) Post- peak behavior

The values of σ_{cc}, σ_{c}, σ_{pc}, ε_{cc}, ε_{c}, ε_{pc} and the descending curve are shown in Table 2.2. Delso used this model to predict the bending behavior of UHPFRC beam by finite element calculations with good agreement with testing results. But this model just limits for UHPFRC with particular values of fiber content, so the application of this model to other mixtures still unknown.

Table 2.2: Equation of the empirical tensile model based on the average fiber orientation angle

	Stress	Strain
(a)	$\sigma_{cc} = \begin{cases} 50.18\cos\theta - 35.38; & \theta < 37^o \\ 2.79\cos\theta + 2.28; & \theta \geq 37^o \end{cases}$	$\varepsilon_{cc} = \dfrac{\sigma_{cc}}{E_c}$
	$\sigma_{c} = \begin{cases} 55.79\cos\theta - 37.27; & \theta < 38^o \\ 19\cos\theta - 8.4; & 47^o \geq \theta \geq 38^o \end{cases}$	$\varepsilon_{c} = \begin{cases} 62\sigma_c - 3.128; & \theta < 38^o \\ 929\cos\theta - 511; & 47^o \geq \theta \geq 38^o \end{cases}$
	$\sigma_{pc} = \begin{cases} 172\cos\theta - 128.69; & \theta < 37^o \\ 20\cos\theta - 7.23; & 54.5^o \geq \theta \geq 37^o \end{cases}$	$\varepsilon_{pc} = \begin{cases} \dfrac{(\sigma_{pc} - 4.551)}{0.0031}; & \theta < 37^o \\ 6698\cos\theta - 4120; & 47^o \geq \theta \geq 38^o \\ 300; & 54.5^o \geq \theta \geq 47^o \end{cases}$
(b)	$\sigma(w) = \dfrac{\sigma_{pc}}{1 + \left(\dfrac{w}{1+\cos\theta}\right)\left(\dfrac{\frac{l_f}{2} - w}{\frac{l_f}{2}}\right)}$	l_f: fiber length (mm) w: crack opening (mm) θ : average fiber orientation angle (°)

Another research, **Frettlöhr** [39, 40] proposed constitutive law in tension of UHPFRC, the model based on the correlation between the uniaxial tensile strength $f_{ct}(\eta)$ and one dimensional tensile strength , which specified in term of the fiber orientation.

$$\chi(\eta) = \frac{f_{ct}(\eta)}{f_{ct,1D}} = 0.0014e^{(5.97\eta+0.22)} + 0.32\eta \qquad (2.24)$$

Where: $\chi(\eta)$ is a ratio of fiber orientation related tensile strength $f_{ct}(\eta)$ to one-dimensional tensile strength $f_{ct,1D}$. Frettlöhr (2011) calculated value of the one dimensional tensile strength, $f_{ct,1D}$, which fits very well to the value of previous research [39].

Ascending and descending branch of the stress-crack opening law are represented by following equations, respectively.

$$\frac{\sigma(w)}{f_{ct}} = \left(1 - \frac{f_{ct,el}}{f_{ct}}\right)\frac{w}{w(f_{ct})} + \frac{f_{ct,el}}{f_{ct}} \quad for\ w < w(f_{ct}) \qquad (2.25)$$

$$\frac{\sigma(w)}{f_{ct}} = \left(1 - \frac{2.(w - w(f_{ct})}{\eta l_f}\right)^2 \quad for\ w \geq w(f_{ct}) \qquad (2.26)$$

In which, w is crack opening, l_f is fiber length, $f_{ct,el}$ is tensile stress at the elastic limit, and $w(f_{ct})$ is crack opening corresponding to $f_{ct}(\eta)$, which calculated by following equation:

$$w(f_{ct}) = w(f_{ct}).(1.65\eta - 0.66) \quad for\ f_{ct} > f_{ct,el} \qquad (2.27)$$

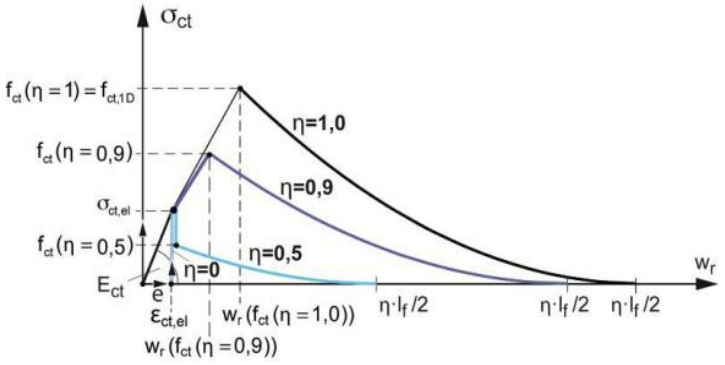

Figure 2.19: Tension behavior of UHPFRC for different fiber orientation factors η

2.5. Punching shear model

Punching shear failure is a type of brittle failure, caused by high shear stress in slab- column connection area of flat slabs. This brittle failure occurs without warning and may lead to progressive collapse of slab and structure. Because of that reasons, many researches were performed the test to get the best understanding in this type of failure, and proposed empirical expressions to predict the punching shear capacity of flat slabs.

Punching shear model for flat slabs without shear reinforcement, is firstly proposed by Kinnunen & Nylander in 1960 [41], and based on it, after that, Muttoni & Schwartz had further developed the model by considering the appearance of the critical shear crack theory [42, 43]. In design purposes, ACI 318-11 and EC2 2004 offered equations to calculate the punching shear strength, which form can be easy to apply in design. For FRC composites, the empirical formula proposed by many researches [44-46], which considered the addition of fibers.

In another technique, finite element method (FEM) is a strong method which used for analysis and predict the punching shear behavior of flat slabs [47-54]. Nonlinear analysis commercial software have become more and more popular in recent years as engineers effort to more realistically simulate the behavior of structures subjected to all types of loading [54].

Relating to reinforced concrete (RC) slabs, many researchers used the FEM to model the punching behavior with different constitutive models [47, 49, 54]. In research of Polak (1998) [49], a global analysis finite element model was developed to predict flexural and punching shear behavior and failure of RC slabs with and without shear reinforcement, which based on layered, degenerate shell elements, allows the analysis of slabs for shear without a complex and time-consuming analysis using three-

dimensional elements [49]. The model got load-displacement curves and took into account the effect of shear reinforcement, showed the good agreement with their experimental results.

Based on the support of computer, Alam (2012) [54] used the finite element software DIANA to develop the finite element model, based on total strain crack models. The input for these models includes two portions: (1) the basic properties such as modulus of elasticity, Poisson's ratio, strength in compression and tension, and (2) the description of the tensile, shear and compressive behavior of concrete and reinforced bar. The Mohr Coulomb yield criterion is used in this analysis [54]. By supporting of another finite element software, Genikomsou (2015) [47] and Wosatko (2015) [51] modeled the RC slabs under punching shear by damage plasticity model in ABAQUS. And punching shear failure was also simulated for concrete column footings by using another software package ANSYS by Vacev (2015) [50].

Most of the model which presented above, the bond between bars and concrete were assumed by perfect bond. The nonlinear material model is used for conventional concrete and reinforced bars. The different thing is the constitutive model which applied to concrete model. For ANSYS package, they use the constitutive model for tri-axial behavior of concrete from Willam and Warnke (1975) [55]; or for ABAQUS, they use the damage-plasticity model which proposed by Lubliner *et al.* (1989) [56] and developed by Lee *et al.* (1998) [57].

The problem is how to perform the numerical analysis, by applying the finite element method. That is the procedure how commercial software solve our problem. And we should notice herein that results from these models and experiments showed good agreement. But the most important aspect in numerical modeling of RC structures is the accuracy of material modeling [47].

Developing for punching shear behavior of FRC composites, Ragab (2013) [53] studied punching shear of SFRCC slabs by using nonlinear analysis in ANSYS package. The thing different from the previous model for RC slabs is that fibrous concrete was represented as new material with new elastic modulus, tensile strength and compressive strength.

In 2015, Teixeira [52] performed the numerical simulation according to the Reissner-Mindlin theory under the FEM to simulate the punching shear behavior of SFRC slabs. In this model, the post-cracking behavior of SFRC attained by inverse analysis by fitting the numerical to experimental curves observed from the punching shear tests [58], based on RILEM TC 162-TDF [21]. This material model took into account the effect of fiber content, represented in post-cracking stage. The slab was discretized to fifteen layers, and assigned the different post-cracking model to capture the segregation problem (Figure 2.20).

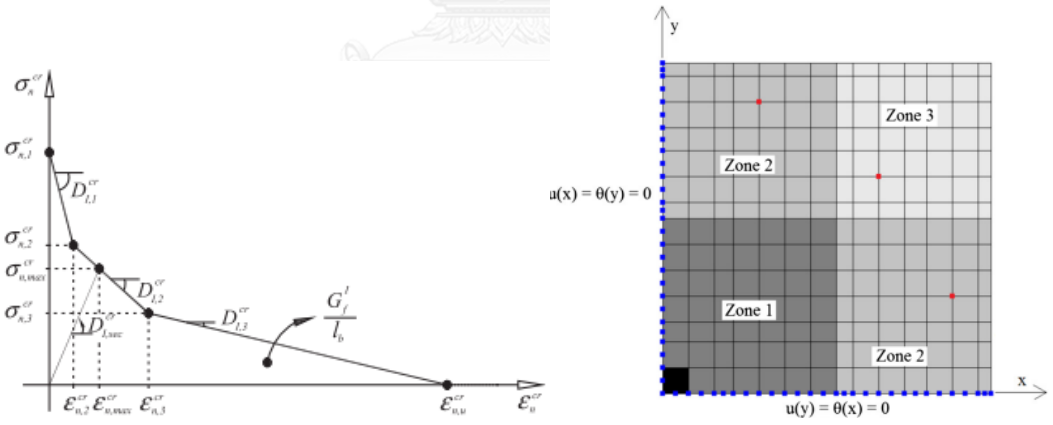

Figure 2.20: From Teixeira model: (a) Post-cracking model in tension of SFRC, and (b) modeling of slab

CHAPTER 3

FINITE ELEMENT MOTHOD AND MATERIAL MODEL

3.1. Introduction

This chapter introduces the finite element procedure in ABAQUS through concrete damage plasticity (CDP) model which shows how program solves this problem by numerical method, and propose a constitutive model of material. Constitutive model includes information such as elastic modulus, compressive behavior, and the most important data is tensile stress-strain relationship which consider the effect of fiber orientation. This material model was verified by applying to model I-beam from previous experiment by CDP. After getting reasonable result when compared to experimental results, finite element model of punching shear behavior of the slabs was performed.

3.2. Finite element method- Concrete damage plasticity (CDP) model [59]

In this study, finite element model which performed to model the punching shear behavior of UHPFRC slabs is the concrete damage plasticity in ABAQUS package. This software is used both for linear and nonlinear analysis of static and dynamic problems.

The model is a continuum, damage, plasticity-based, model for concrete. There are two main failure mechanism, tensile cracking and compressive crushing of the concrete material, are assumed in this model. The uniaxial tensile and compressive response of material is characterized by damaged plasticity, as shown in Figure 3.1 and Figure 3.2.

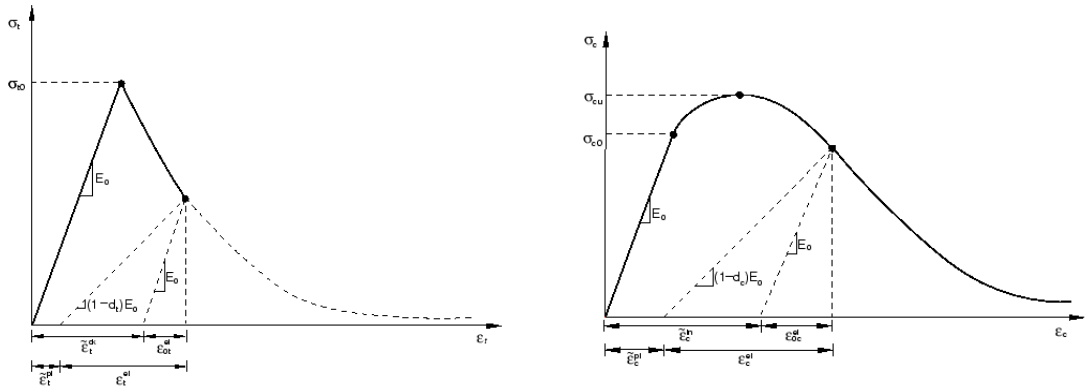

(a) (b)

Figure 3.1: Response of concrete to uniaxial loading in (a) tension and (b) compression

As shown in Figure 3.1, when the concrete structure is unloaded from any point on the strain softening part of the stress-strain responses, the unloading response is weakened: the elastic stiffness of the material appears to be damaged (or degraded). The degradation of the stiffness of elasticity is governed by two damage variables, d_t and d_c, which are assumed to be functions of the plastic strains, temperature, and field variables.

If E_0 is the initial (undamaged) elastic stiffness of the material, the relationship between stress and strain under uniaxial tension and compression loading are, respectively:

$$\sigma_t = (1 - d_t)E_0(\varepsilon_t - \tilde{\varepsilon}_t^{pl}),$$
$$\sigma_c = (1 - d_c)E_0(\varepsilon_c - \tilde{\varepsilon}_c^{pl}). \qquad (3.1)$$

Where, d_t and d_c, are two damage variables which represent the degradation of the elastic stiffness.

Then the effective tensile and compressive cohesion stresses are defined as following equations, which used to determine the size of the yield (or failure) surface:

$$\bar{\sigma}_t = \frac{\sigma_t}{(1-d_t)} = E_0(\varepsilon_t - \tilde{\varepsilon}_t^{pl}),$$
$$\bar{\sigma}_c = \frac{\sigma_c}{(1-d_c)} = E_0(\varepsilon_c - \tilde{\varepsilon}_c^{pl}). \quad (3.2)$$

If the damage parameters are specified, plastic strains will be automatically calculated from cracking strain (in tension) and inelastic strain (in compression) to represent the damage outside the elastic range. If this damage parameter absent, plastic strains will be set equal to from cracking strain and inelastic strain.

$$\tilde{\varepsilon}_t^{pl} = \tilde{\varepsilon}_t^{ck} - \frac{d_t}{(1-d_t)}\frac{\sigma_t}{E_0}.$$
$$\tilde{\varepsilon}_c^{pl} = \tilde{\varepsilon}_c^{in} - \frac{d_c}{(1-d_c)}\frac{\sigma_c}{E_0}. \quad (3.3)$$

The model in CDP adopt the yield function of Lubliner et al. (1989), with the modifications proposed by Lee and Fenves (1998) to account for different evolution of strength under tension and compression. The evolution of the yield surface is controlled by the hardening variables, $\tilde{\varepsilon}_t^{pl}$ and $\tilde{\varepsilon}_c^{pl}$. In terms of effective stresses, the yield function takes the form:

$$F = \frac{1}{1-\alpha}\left(\bar{q} - 3\alpha\bar{p} + \beta(\tilde{\boldsymbol{\varepsilon}}^{pl})\langle\hat{\bar{\sigma}}_{\max}\rangle - \gamma\langle-\hat{\bar{\sigma}}_{\max}\rangle\right) - \bar{\sigma}_c(\tilde{\varepsilon}_c^{pl}) = 0, \quad (3.4)$$

Where,

$$\alpha = \frac{(\sigma_{b0}/\sigma_{c0}) - 1}{2(\sigma_{b0}/\sigma_{c0}) - 1};\ 0 \le \alpha \le 0.5,$$
$$\beta = \frac{\bar{\sigma}_c(\tilde{\varepsilon}_c^{pl})}{\bar{\sigma}_t(\tilde{\varepsilon}_t^{pl})}(1-\alpha) - (1+\alpha),$$
$$\gamma = \frac{3(1-K_c)}{2K_c - 1}. \quad (3.5)$$

Yield surfaces in the deviatoric plane, corresponding to different values of K_c.

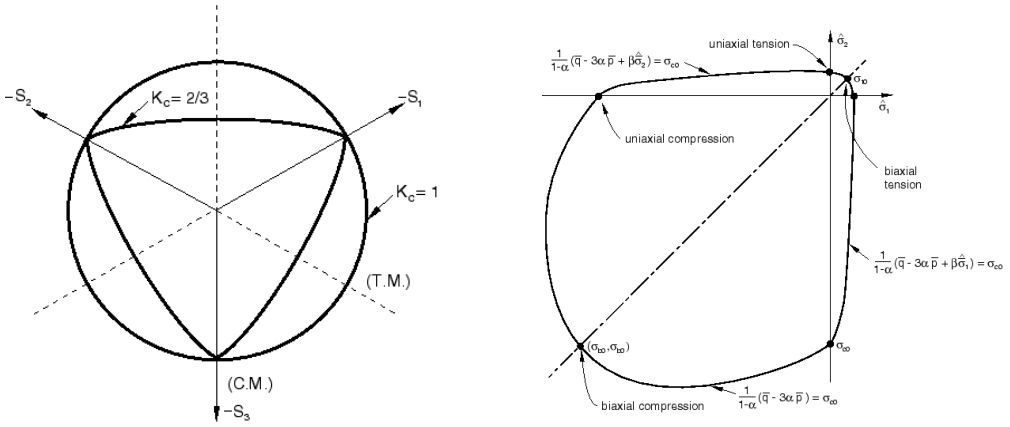

(a) (b)

Figure 3.2: Yield surfaces (a) in deviatoric plane, and, (b) in plane stress

The crucial to the computational efficiency of the explicit procedure is the use of diagonal element mass matrices because the inversion of the mass matrix that is used in the computation for the accelerations at the beginning of the increment is triaxial:

$$\ddot{\mathbf{u}}^{(i)} = \mathbf{M}^{-1} \cdot (\mathbf{F}^{(i)} - \mathbf{I}^{(i)}), \tag{3.6}$$

where ***M*** is the diagonal lumped mass matrix, ***F*** is the applied load vector, and $\mathbf{I}$ is the internal force-vector. The explicit procedure requires no iterations and no tangent stiffness matrix.

Many kinds of structural elements are provided in ABAQUS to model concrete such as shell/plate element, solid 3D element or beam/truss element. While the formulation of shell element is based on the two principle stress (i.e. σ_1 and σ_2) without σ_3 in yield criteria and, solid element could represent full shear and normal stress in 3D. For punching failure, it often occurs at locations where large bending moment and shear forces are concentrated, the effect of σ_3 could be significant. The reinforced concrete element is, therefore recommended to use three-dimensional solid element.

The three most commonly used solid elements are shown in the Figure 3.3. In ABAQUS/Explicit, the 20-node brick element is not provided, therefore, the other two kinds of element are used in this study to represent reinforced concrete.

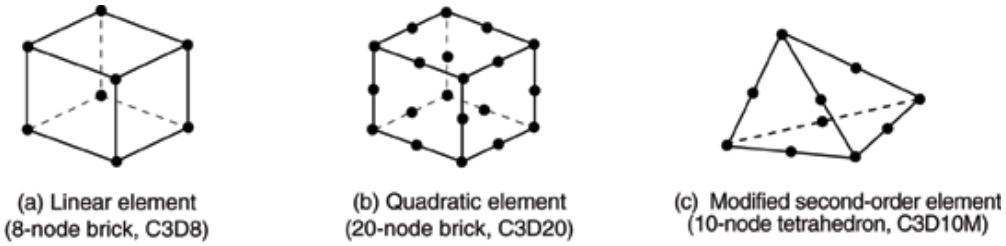

Figure 3.3: Linear brick, quadratic brick, and modified tetrahedral elements

Steel bar reinforcement could be simulated by 2-node and 3-node truss elements embedded in the concrete element at the specified location in the structure. This truss element can carry axial load only. Those truss elements are embedded in a set of solid elements, used to constrain the translational degrees of freedom of the embedded nodes. The stiffness of steel reinforced concrete element is simply obtained by combining stiffness matrices of concrete and steel together. The other method to model steel reinforcement is that model the bar as 3D bar and introduce the interface between the bar and concrete, then it will behave as the 3D elements as same as concrete.

3.3. Tensile model of UHPFRC considering effect of fiber orientation

3.3.1. Background

In the CDP model in ABAQUS, stress-strain behavior in tension of material is important data, is a decisive factor to model behavior of beam or slab under shear failure. In this study, the curves input in each model were varied, depending on distance from casting positions, or fiber orientation in different expressions. Analytical model from previous studies were used, and based on the experimental data to obtain own model and input data for this research.

From the previous chapter, the understanding about tensile behavior of UHPFRC was provided, such as an improvement from conventional concrete or FRC, the effect of adding fiber, type or volume fraction of fiber, and especially the fiber orientation. Comparing to FRC or ordinary concrete, UHPFRC reaches a high tensile strength, presence of hardening part and upgrade post-cracking behavior. Each kind of fiber, hook end, twist or straight fiber presents the difference not only in tensile strength but also in the length of hardening part. Or increasing volume content of fiber with suitable value help concrete increase significantly tensile strength of material. Each factor has their own impact on the behavior of UHPFRC in tension. This study focused on considering effect of casting position through fiber orientation coefficient, and a part of the fiber volume content effect.

The research of **Li** (1993) [34] presented an expression for the tensile behavior of UHPFRC, combined from 3 parts: aggregate bridging, fiber bridging and the pre-stress already present in fibers before cracking. From this model, **Wuest** (2007) [37, 38] investigated data from experiments, and applied to Li's model. Comparing to the experimental result, analytical results were accurate for the mixtures with more than 3 % fiber content.

In **Delso**'s research [36], the tensile model (presented in the previous part) was applied to model bending behavior of beams by finite element analysis. The model showed agreement results when comparing to experimental data. However, this model will be shortly validated with the results of other experiment, and also adapted to consider fiber density when using UHPFRC with different fiber dosages [36].

Wille and Namaan (2011, 2014) [17, 19] proposed idealized simplified response of strain-hardening of UHPFRC, as mentioned before in previous part. Formula for calculating cracking strength and tensile strength also presented based on many experimental results with different types and volume fraction of fiber.

Frettlöhr (2011) proposed a tensile model of UHPFRC considering effect of fiber orientation based on the correlation between the uniaxial and one dimensional tensile properties of mixtures, includings strength and crack-opening, as presented in literature review part.

In experiment of Pansuk [60], stress-strain curves in tension were observed in the case with different volume content of fiber, as present in the experimental program chapter. Because researcher created the homogeneous distribution of fiber throughout the whole tensile specimen, so the data from this experiment was considered to be random distribution of fiber. The analytical model which proposed as previous part should reach agreement with these experimental result.

In both models of **Frettlöhr** and **Namaan**, tensile model was composed of three parts: elastic, strain hardening and softening. The first two parts were represented by linear behavior, the third part, post-peak behavior was shown as non-linear curve. In this study, the combination of **Frettlöhr**'s and **Namaan**'s model was proposed, and found to be appropriate for the description tensile behavior of UHPFRC with different fiber orientation coefficient. The detail of proposed model presented as follows.

3.3.2. Tensile stress-strain curve for random distribution of fiber

The first part of tensile model was defined by the cracking point, including modulus of elastic E_c and cracking stress f_{cr}. The formula from Graybeal's research [13] was used to calculate the modulus of elasticity of UHPFRC material. The cracking stress of UHPFRC was assumed to be same as the value of ordinary concrete [61, 62], shown as following expression.

$$E = 3840\sqrt{f_c'}$$

$$f_{cr} = 0.31\sqrt{f_c'} \qquad (3.7)$$

Strain hardening is typical behavior of the length of strain hardening part that depend on the value of strain at peak stress, ε_{pc}, normally exceeds 0.25% and ranges from 0.3 to 0.5 % as conclusion from Wille's and Namaan's researches based on a large amount number of experiments. Furthermore, the tensile strength would be adopted from experiment for each UHPFRC mix.

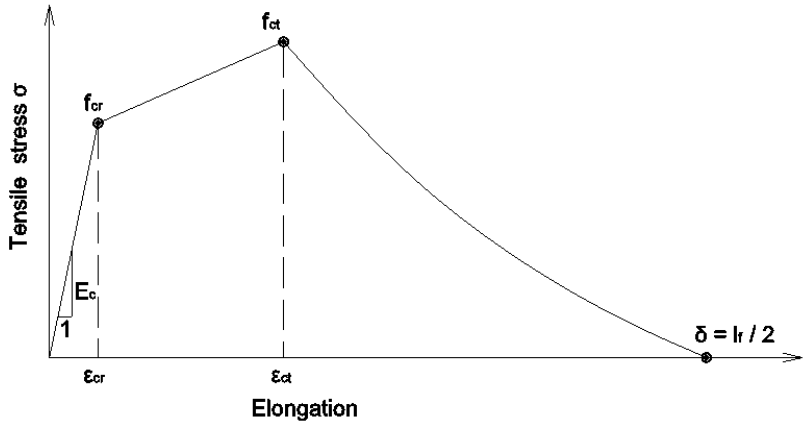

Figure 3.4: Proposed constitutive law in tension

Softening part of constitutive model starts at peak stress, then its stress reduces significantly to zero at the point that all fibers completely pull out from concrete. In the design applications, many analytical models were proposed for this part to complete tensile stress-strain or stress-crack opening curve by researchers such as Li

(1993) [34], Stang (1995) [63], SpaSojević (2008) [3], or **Frettlöhr** (2011) [39]. Most of the models is an exponential function of crack opening with different exponent values.

Analytical expressions of the descending branch of **Frettlöhr**'s study as shown in literature review part, which capture these effects, were chosen to evaluate the effect of fiber orientation as the purpose of the study. In this constitutive law, after reaching the peak point, tensile stress start reducing part and come to zero at the point crack opening δ equal $\eta l_f/2$. However, in most of the previous study [17, 19, 22, 36, 37], the tensile stress was proposed to end at the cracking opening of $l_f/2$, therefore, this value is used in this study by modifying the formula of descending part of **Frettlöhr**'s study. This modified expression gave a good agreement with experimental curves from beam test of Pansuk [60].

$$\frac{\sigma(w)}{f_{ct}} = \left(1 - \frac{(\mathrm{w} - \mathrm{w}(f_{ct})}{l_f / 2}\right)^2 \quad for\ w \geq \mathrm{w}(f_{ct}) \tag{3.8}$$

The tensile stress-strain curves were created based on those selected models, combined with using experimental result. The strain ε_{pc} could be change within the range that mentioned before as a material parameter to find out the suitable value for material.

3.3.3. Considering effect of fiber orientation

Fiber orientation was introduced to the model through tensile strength $f_{ct}(\eta)$ and crack opening corresponding to $f_{ct}(\eta)$, $w(f_{ct})$.

$$\chi(\eta) = \frac{f_{ct}(\eta)}{f_{ct,1D}} = 0.0014e^{(5.97\eta + 0.22)} + 0.32\eta \tag{3.9}$$

$$\gamma(\eta) = \frac{\mathrm{w}(f_{ct})}{\mathrm{w}(f_{ct,1D})} = \left(1.65\eta - 0.66\right) \quad for\ f_{ct} > f_{ct,el} \tag{3.10}$$

Each value of fiber orientation coefficient draws the point of maximum tensile stress, including tensile strength and corresponding crack opening (see Figure 2.21). For the random distribution of fiber, the fiber orientation coefficient was obtained, then one dimensional tensile strength was calculated from expression of $\chi(\eta)$ when tensile strength was from the experimental result.

Descending branch of the stress-crack opening law are represented by following Equation 3.9 as mentioned in the previous part.

Subsequently, with material properties for random distribution of fiber, tensile constitutive model could be created for each value of fiber orientation factor. As mentioned in literature, the fiber orientation coefficients are different at different distances from casting position. As a result, the constitutive model is possible to define at each position if there is a relation between fiber orientation and distance; and this relation could be found in Grunewald's study [64] as presented in the previous chapter.

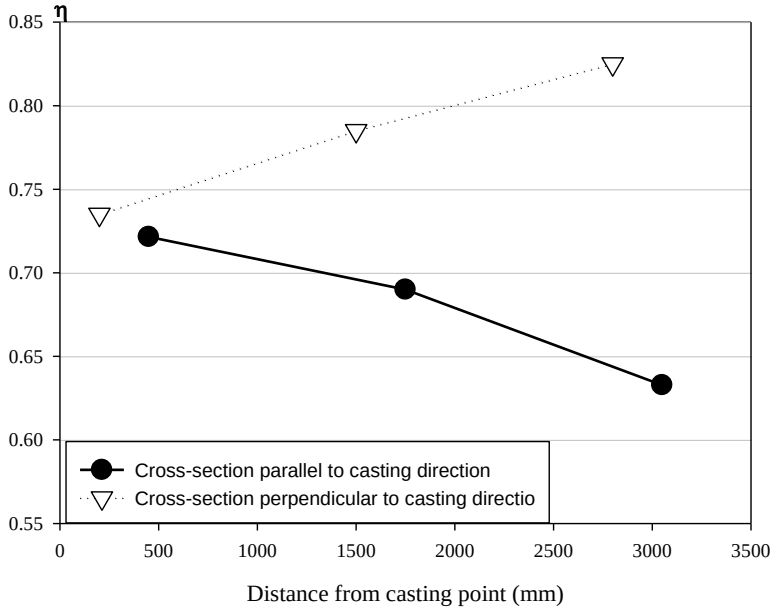

Figure 3.5: Fiber orientation in the beam at different distances from casting position

Figure 3.5 shows the fiber orientation of two different groups (including the section parallel and perpendicular to casting direction) at different distance from casting point. The result showed that while the cross-sections perpendicular to casting direction increase effective fibers as far as casting points, those values reduce for cross-sections parallel to casting direction. To see exactly trend of those increase or decrease, and, to predict fiber orientation coefficient at other points with different distances, regression was performed for each group of sections. Consider the data in detail, it showed that linear regression can be used to represent the relation among three points. Therefore, linear regression will be performed and applied afterward. The fiber orientation at each point and regression line formula of each group section are shown in following table.

Table 3.1: Different fiber orientation coefficients at different cutting sections

Parallel sections		**Perpendicular sections**	
Distance d (mm)	η	Distance d (mm)	η
450	0.722	200	0.735
1750	0.680	1500	0.785
3050	0.633	2800	0.825
$\eta = -3.41\times10^{-5}d + 0.730$		$\eta = 3.46\times10^{-5}d + 0.739$	

The regression line equations of the two groups show the opposite slope values but almost same magnitudes, and alike value of the second constant. These slopes could be used to represent distance-fiber orientation relationship. To be applicable later, following formula is proposed to calculate fiber orientation factor from different distances:

$$\eta = 3.46\times10^{-5}d + \eta_{random} \quad (3.11)$$

$$\eta = -3.41\times10^{-5}d + \eta_{random} \quad (3.12)$$

Where: η_{random} =0.707, is fiber orientation factor for random distribution of fiber.

First formula is for calculating fiber orientation coefficient of the sections perpendicular to casting direction, the second is for of the sections parallel to casting direction. These two formulas will be applied to calculate tensile stress-strain curve as a main part of the modeling process. However, those slopes can be changed as a material parameter to investigate the effect on punching shear behavior.

The tensile constitutive law now can be created for each point by the function of distance. Following figure shows tensile curves of different distances from casting position of the I-beams.

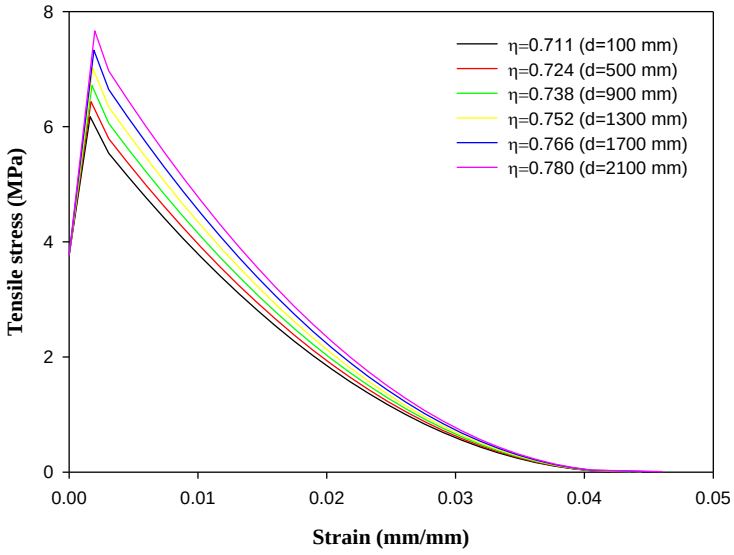

Figure 3.6: An example of tensile stress-strain curves of a UHPFRC material with different fiber orientation factors

3.4. Material models of UHPFRC: other parameters

3.4.1. Compressive behavior

There were many analytical models to demonstrate compressive behavior presented in literature chapter. Three models from research of Soroushian and Lee (1989), Barros and Figueiras (1999), and Mansur (1999) were plotted in Figure 3.7.

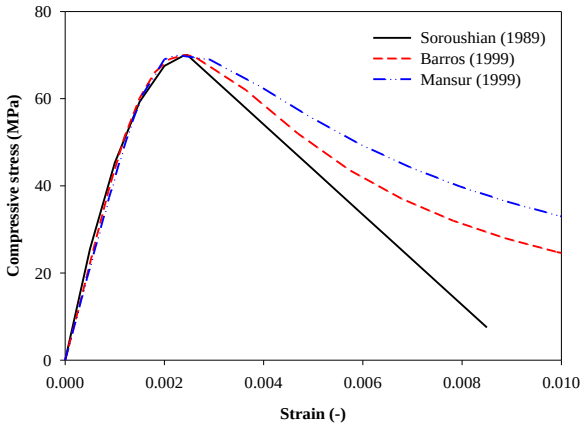

Figure 3.7: An example of different compressive constitutive models

It is clearly seen that three curves are closed to each other in ascending portion, but then be different in descending branch. All of this model could be applied for fiber reinforced concrete. However, the model from Mansur (1999) gave a higher range of compressive strength that can be exceeded 70 MPa accordance with the strength of the presented study. Therefore, the analytical models of Mansure study were used for the finite element analysis. The formulas of model were shown as follows:

$$\sigma_c = f_c^{'} \frac{\beta.n}{\beta - 1 + n^{\beta}} \quad for \ 0 \le n \le 1 \tag{3.13}$$

$$\sigma_c = f_c^{'} \frac{k_1.\beta.n}{k_1\beta - 1 + n^{k_2\beta}} \quad for \ n \ge 1 \tag{3.14}$$

With: $n = \frac{\varepsilon}{\varepsilon_0}$, $\beta = \frac{1}{1 - \frac{f_c^{'}}{\varepsilon_0.E_{it}}}$

$$k_1 = \left(\frac{50}{f_c^{'}}\right)^3 \left[1 + 2.5\ RI^{2.5}\right]$$

$$k_2 = \left(\frac{50}{f_c^{'}}\right)^{1.3} \left[1 - 0.11 RI^{-1.1}\right] \tag{3.15}$$

$$E_{it} = \left(10300 - 40000 V_f\right) f_c^{'\,1/3}$$

$$\varepsilon_0 = \left(0.0005 + 0.000072\, RI\right) f_c^{'\,0.35}$$

Where, $f_c^{'}$ is the measured compressive strength; k_1, k_2 are constant, difference in cylindrical specimens and horizontally cast prisms; $RI = V_f l_f / d_f$; V_f is the volume fraction of fibers; l_f / d_f is the aspect ratio of fibers. The compressive strength, the proportion of fiber V_f and fiber aspect ratio were provided from experiment and presented in the next part of the thesis.

3.4.2. Steel reinforcement

The constitutive model of steel was simply presented by bilinear elastic-perfectly plastic model (Figure 3.8), defined by modulus of elasticity, Poisson's ratio and plastic behavior of steel. Those data could follow the result from tensile test of steel bar. The properties of steel used in each experiment are given in the part of each model.

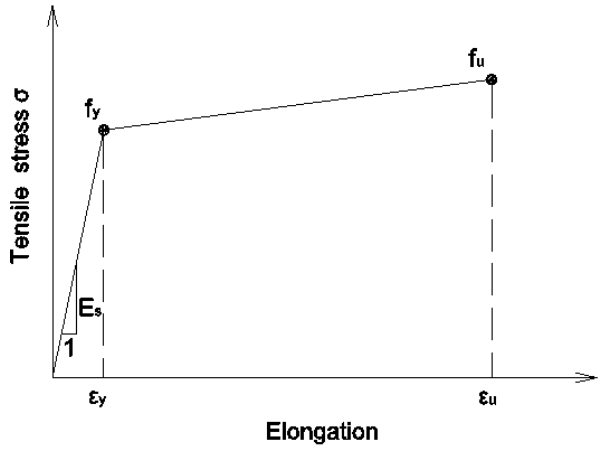

Figure 3.8: Constitutive model of steel reinforcement

CHAPTER 4

FINITE ELEMENT ANALYSIS

4.1. Introduction

The material model that presented before are applied to the finite element analysis to discover the effect of fiber orientation on punching shear behavior of slabs. Beforehand, the material model was validated by an experiment of Pansuk [63] which used same fiber volume content and provided the fiber orientation effect on shear behavior of I-beam.

The experiment was performed by previous study of Tung [65], the experimental results can help to define material properties and actual punching shear behavior of UHPFRC slabs. The results of compressive and splitting tensile test were used to determine the material input parameters. The results from punching shear test, including load-displacement responses, failure cones shape and sizes, stress in steel reinforcements, would be used to compare with FEA results.

4.2. Validation of material constitutive laws and FEA on I-Beam

This subchapter focused on applying the proposed material model to CDP model in ABAQUS /Explicit to simulate shear behavior of UHPFRC I-Beam, which its experiments were performed by Pansuk (2007) [60]. The results from analysis were validated by experimental results.

4.2.1. Experimental procedure and results

In this experiment, three beams of I-shape sections were designed to fail by shear failure under three-point bending test, and cast with different fiber contents (0%, 0.8% and 1.6%).

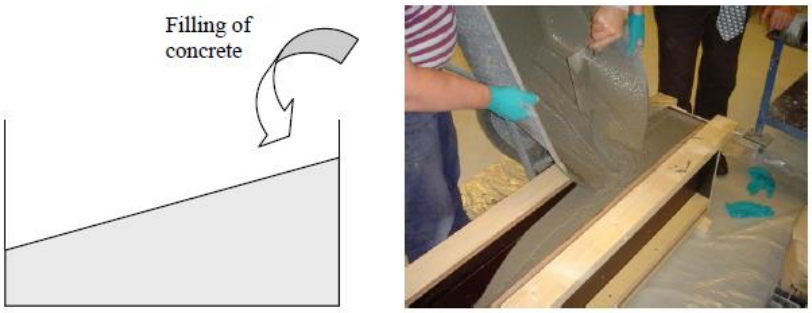

Figure 4.1: Filling method “Flow” according to RILEM [21]

Referring to RILEM [21], the “flow-method” (Figure 4.1) consisted of filling the concrete from one side into the mold and allowed the concrete to level itself was applied in the casting of beam specimens in this study. By applying that method, concrete flowed along the beam from casting position, then led fibers align to the flow direction.

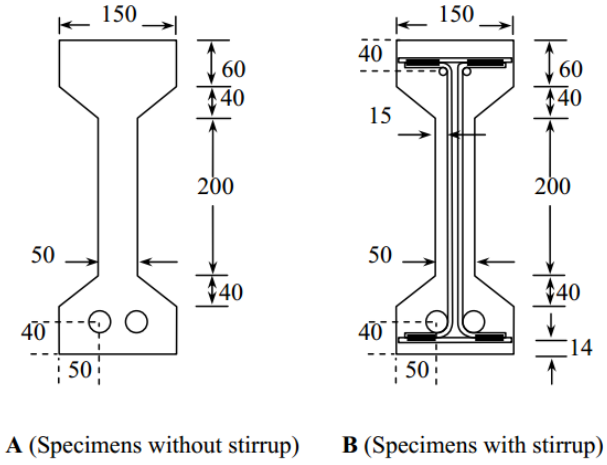

Figure 4.2: Cross sections (unit: mm)

Two parameters investigated in the testing program were the volume fraction of fiber and the presence of stirrup in the beams. The beams of 2400 mm in total length have a span of 2000 mm, 400 mm in total depth and 350 mm in effective depth. Cross sections of all specimens are shown in Figure 4.2. The stirrup was installed with the spacing of 150 mm. The full detail of the dimensions, arrangement of reinforcing steel and loading condition are shown in Figure 4.3.

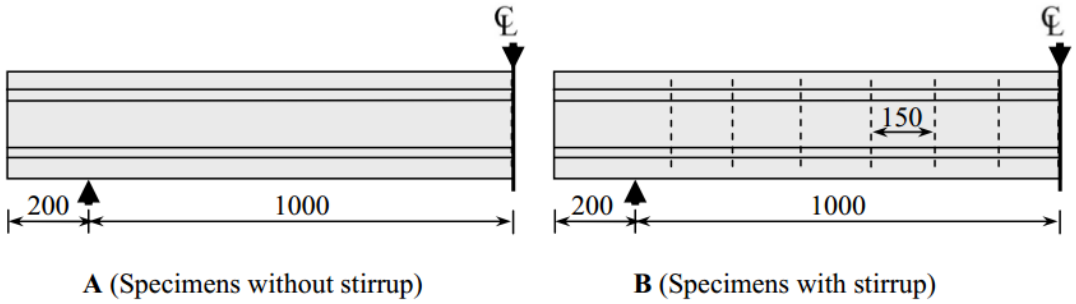

Figure 4.3: Test setup and stirrup placement (unit: mm) [60]

Material properties

In testing properties of material, compressive and splitting tensile tests were conducted by load-controlled in the hydraulic machine to collect these properties; and the direct tensile test was conducted as the control test obtain the uniaxial tensile properties.

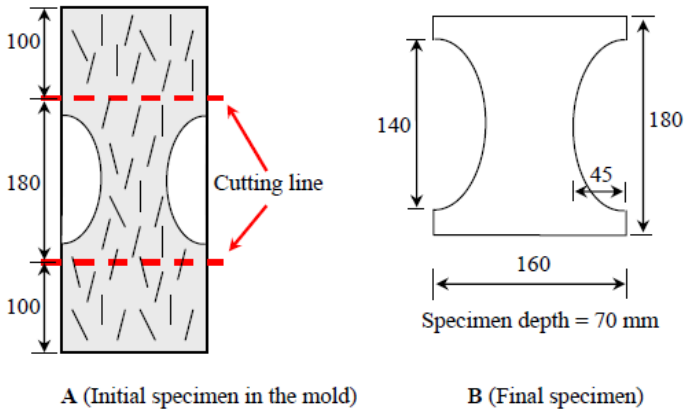

Figure 4.4: Specimens for the direct tensile tests

In uniaxial tensile test, in order to get the homogeneous distribution of fiber throughout the whole tensile specimen, the concrete was cast in the molds that were longer and higher than the final specimens (Figure. 4.4). The initial height of the specimens was 380 mm as shown in Figure. 4.4**A**. The final specimens for testing were obtained by cutting off the 100-mm-high pieces from both top and bottom of the initial specimen. The results from the direct tensile test are shown in Figure. 4.5.

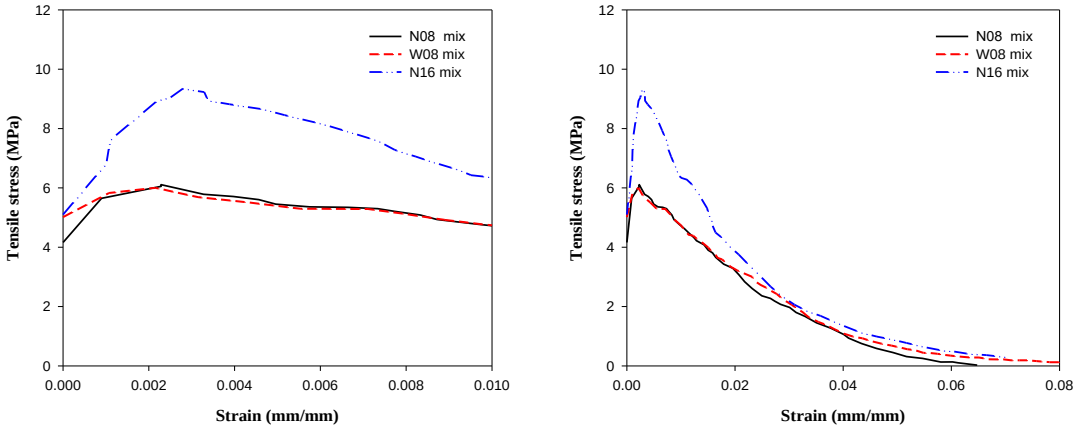

(a) Hardening part of stress-strain curve (b) Whole stress-strain curve

Figure 4.5: Stress-strain response from direct tensile tests of different mixes

Experimental results

From the test results, all the tested beams without stirrup failed by shear, the beam with stirrup failed by flexural mode. Figure 4.6 shows experimental applied load-displacement responses for all beams. The graph illustrates clearly the effect of presence of fiber and volume content itself in shear capacity and load-deformation relationship of beams.

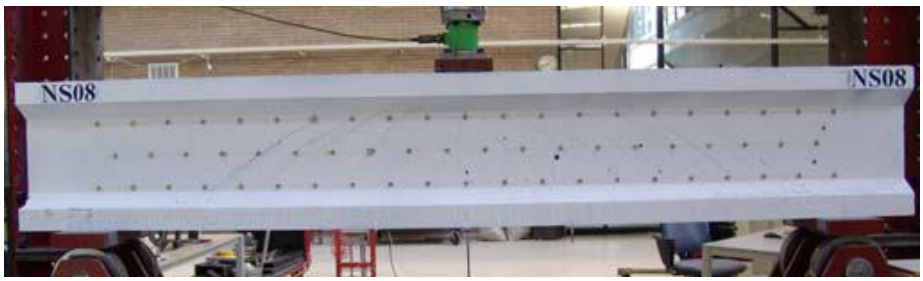

Figure 4.6: Test set up for I-beam failed by shear

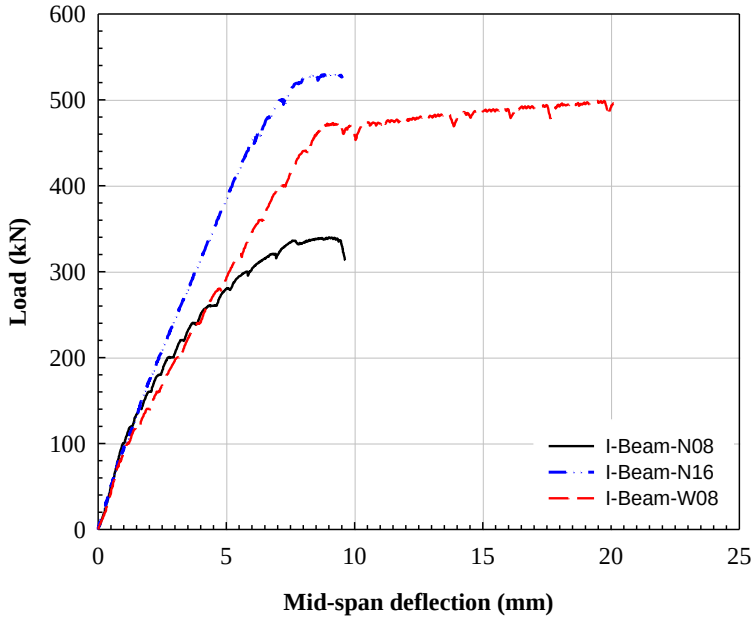

Figure 4.7: Load- mid-span deflection curves

The cracks pattern of testing beam can be observed in Figure 4.8. Many cracks including flexural cracks and diagonal shear cracks formed across the span and propagated toward the top flange. And finally, compressive failure of compressive zone near loading point could be observed and the test was concluded.

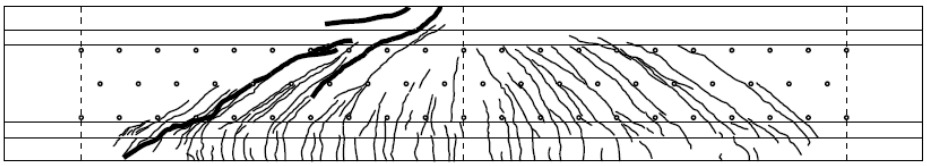

Figure 4.8: Cracks pattern of testing beam

Strain gages were attached to observe strain in the stirrup, positions of strain gages and reference number of stirrups are presented in Figure 4.9. The plotted strains were averaged from 2 locations of the stirrups in the tested part of the beam. Figure 4.10 shows applied load-strain curve observed from stirrup No.4.

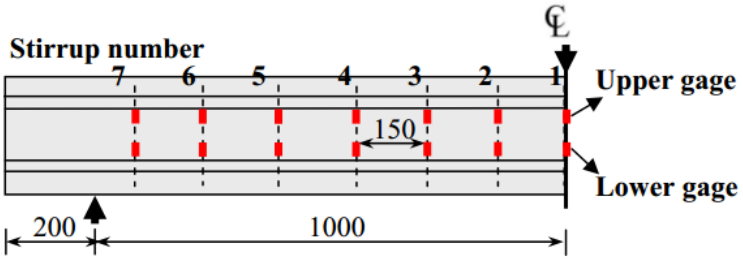

Figure 4.9: Locations and reference number of stirrups whose strains were measured

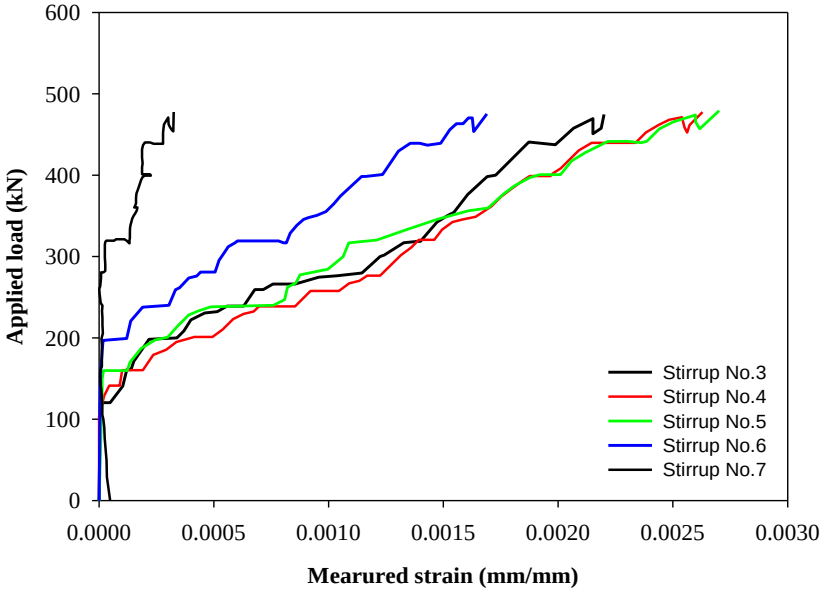

Figure 4.10: Measured strains in stirrups

4.2.2. Model procedure

In this study, three beams of I-shape sections were modelled, including one beam with 0.8% and with stirrup (named as W08), one beam with 0.8% and without stirrup (N08), one beam with 1.8% and without stirrup (N16). The result from the first beam includes load-deflection behavior, cracks pattern and especially is strain in stirrup could be used to compare with experimental results.

Creating input material properties and model procedure were presented in the flowchart in Figure 4.11. The analysis was divided into three main steps with the purpose of validating the proposed material model in considering effect of fiber

orientation. The first step is creating material model for UHPFRC, including for tension and compression behavior of concrete and steel bar. The second step is applying the material constitutive law to finite element model. Tensile behavior in the case of random distribution of concrete obtained from the experiment were used to simulate tested beam as the original model.

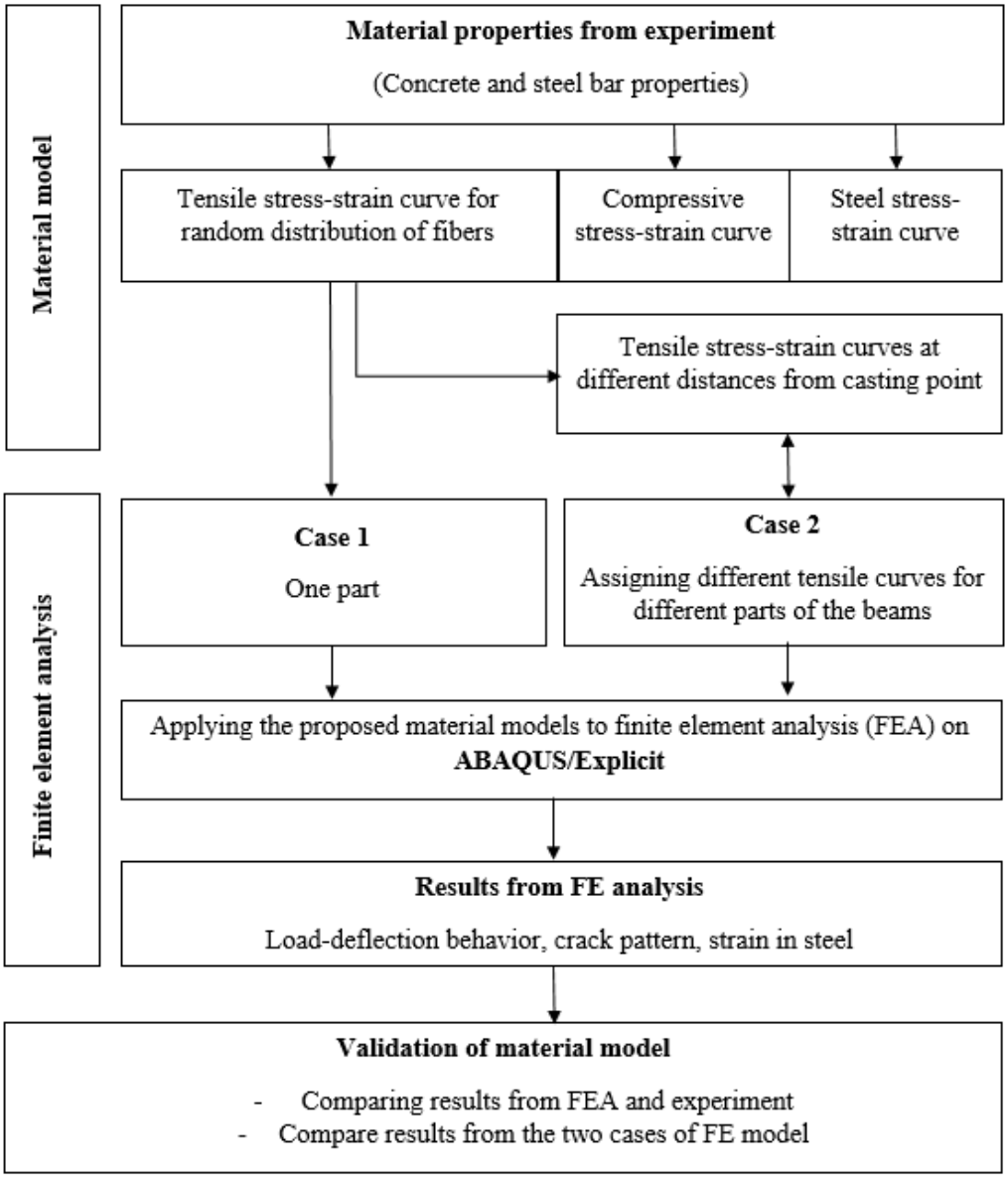

Figure 4.11: Model procedure

The mesh size was studied in this model as a parameter. Analysis and experimental results were compared to verify the accuracy of CDP model in ABAQUS/Explicit and fix a set of parameters used for other models. In the other hand, the proposed material model that based on distance from casting position was applied to beam model as a new approach model.

The beam was divided into a specified number of parts to assign different tensile properties. These properties were assumed to be the properties at the middle section of each part based on the distance from the casting position. Two modes of division and assigning properties were performed with different numbers of divided parts, including 12 and 18 parts (Figure 4.12). Then the reasonable number with accepted result would be used for the others. Comparison of the original and new model results was conducted to figure out the effect of fiber orientation on the beams.

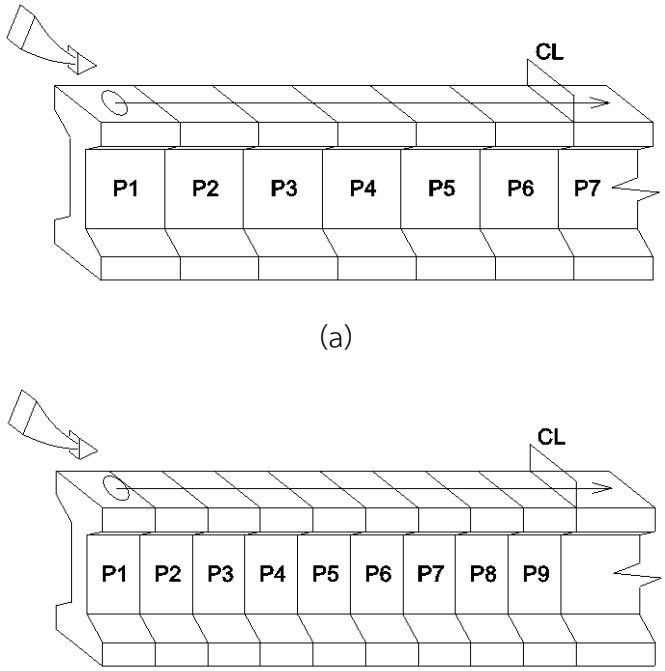

Figure 4.12: Different manners for division and assignment of different tensile constitutive models: (a) 12 divided parts and (b) 18 divided parts

4.2.3. Finite element analysis

a) Geometry model and boundary conditions

The 3D models were carried out in ABAQUS/Explicit using concrete damage plasticity model. The tested beams were simply supported on two sides by resisting displacement in vertical direction. Owing to symmetry, only one-fourth of the beam could be modelled, but the material properties were changed along the beam, so a half were simulated (Figure 4.13).

Afterward, symmetric conditions were applied to symmetric surface. The applied load was simulated by uniform distributed load over a steel plate. The interaction of this plate and the beam was represented as frictionless in tangential direction, and hard contact in normal direction. At the supports, vertical movement was resisted, displacements in the other directions were free.

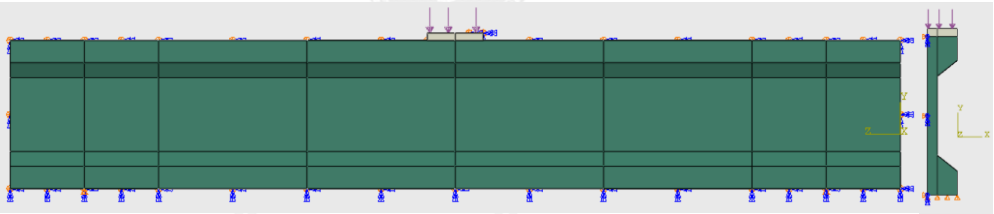

Figure 4.13: Beam model in ABAQUS/Explicit

b) Element selection and element size

8-node brick element (C3D8) which available in ABAQUS/Explicit was used to represent concrete element, and 2-node truss element used for steel bar reinforcement. Steel bars were simulated as embedded in concrete element at the specified location in the beam without bond-slip between two elements. The stresses of embedded steel bar are obtained from the displacement field of host elements. The other consideration is that there is no bending stiffness in embedded truss

elements, therefore, dowel action mechanism of the longitudinal steel reinforcement does not contribute to shear behavior.

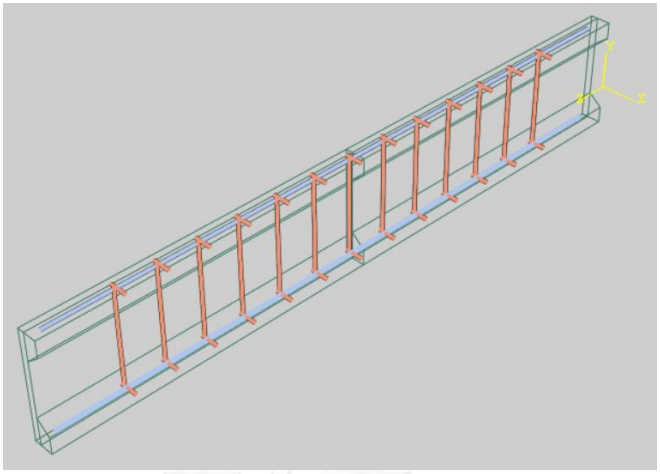

Figure 4.14: Representation of steel bar in the model of beam W08

Many previous studies showed that the ABAQUS concrete model is highly mesh dependence [47, 66], therefore, study of mesh optimization was performed to find optimal mesh size. The mesh sizes of 3D elements were varied with an approximate aspect ratio of 1. The beam N08 was used to study mesh parameter. Mesh size was varied with 10 mm, 15 mm, and 25 mm. The suitable mesh size that shown clearly shear behavior of beam and best fit with experimental results was used to model the other beams. Steel bars were meshed as same size with concrete element.

c) Numerical parameters

All of numerical parameters were set as the default value such as damage parameters in tension and compression.

d) Input material model

As mentioned before in previous subchapter, random distribution of fiber was created in direct tensile test, therefore, the tensile stress-strain responses for this case were taken from the experimental results and idealized by following three-part curve

as proposed before. The data of the tensile model of three beams are described in Table 4.1, and Figure 4.15.

The analysis was performed in two cases, including model without considering fiber orientation (original model), and with considering fiber orientation (new approach model).

Table 4.1: Parameters for creating tensile model

	N08	W08	N16	Unit
f_c'	147.7	144.1	146.7	MPa
f_{cr}	3.77	3.72	3.75	MPa
$f_{ct\ random}$	6.11	6.0	9.2	MPa
$w_{ft\ random}$	0.228		0.355	mm
η_{random}	0.707			-
f_{1D}	17.70	17.38	26.08	MPa
w_{1D}	0.45		0.7	mm
L (*)	110			mm

(*) Length of measurement of the direct tensile test specimens

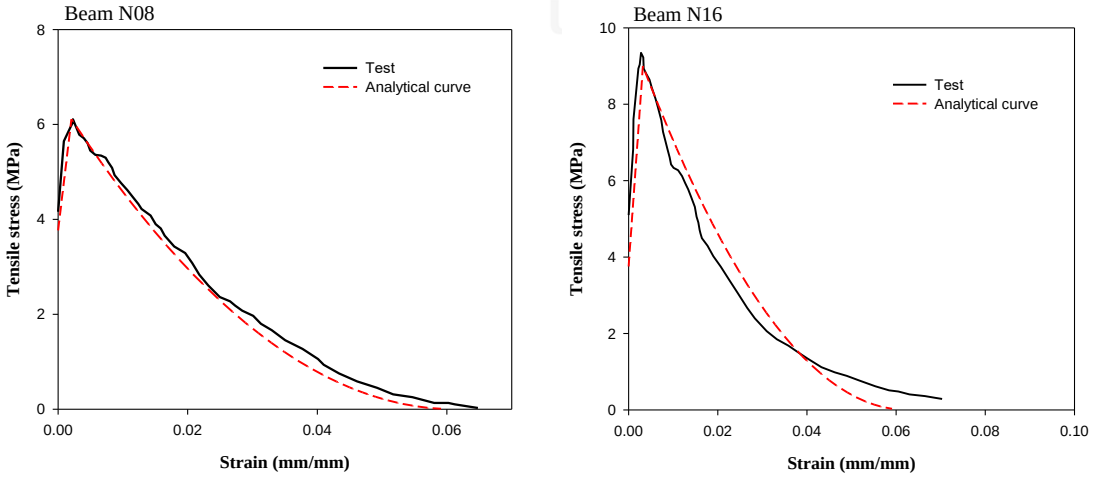

(a) (b)

Figure 4.15: Tensile stress-strain curve from experiment and model of beam (a) N08 and (b) N16

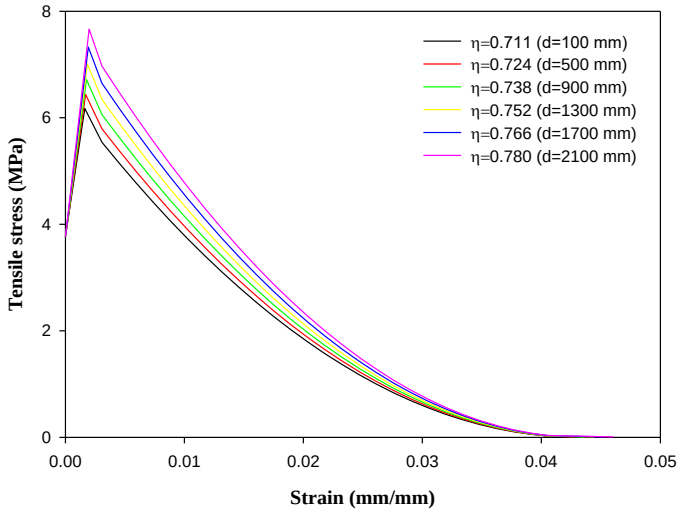

Figure 4.16: Tensile stress-strain curves of a UHPFRC material with different fiber orientation factors

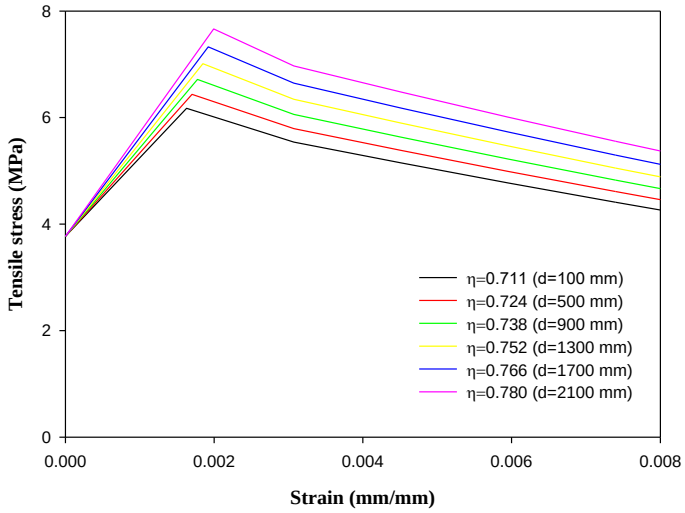

Figure 4.17: Tensile hardening part of different tensile stress-strain curves

When the mixture flowed, fiber tried to align along the casting direction. In this case, for the beam, inclination of fiber changed along the length of the beam from casting point. The formulas shown the tensile behavior corresponding to distance from casting position (named as “d” from now on) were presented in the previous chapter. The finite element model presents this characteristic by dividing into many part along the beam and assigning different properties which represented by different tensile behaviors. Number of parts of beam was considered as a parameter to decide sufficient

divided parts. In the beam model, numbers of divided part were varied with 12 and 18 parts, which shown in Figure 4.12. This idea was applied to find out the effect of casting position or fiber orientation in this study.

The "***d***" (the distance from casting position) value of each part was determined by the distance between middle of that part and the casting point that at 100mm far from a side surface. For each case of a number of parts, the distance would be calculated and then applied to the proposed model to figure out tensile constitutive curves. Figure 4.16 and Figure 4.17 show different curves according to different fiber orientations at specified distances.

The other material parameters for UHPFRC material that were used in this study are: the modulus of elasticity E_c, the Poisson's ratio **ν**, and the compressive behavior of each slab. The model from Mansur's study [7]was adopted to present compressive behavior of UHPFRC in this study. The strain at maximum compressive stress is a function of strength, fiber volume, and the aspect ratio of fiber. The Poisson's ratio was considered as 0.2 for all beams. Table 4.2 shows the parameters to create compressive stress-strain curve for each beam.

Table 4.2: Parameters for compressive model

	N08	**W08**	**N16**	**Unit**
f'_c	147.7	144.1	146.7	MPa
ε_0	2.87e-3	2.85e-3	2.87e-3	-
E_c	46.7	46.1	46.5	GPa
ν	0.2	0.2	0.2	-

Steel bars were modelled by bilinear curve, including elastic and plastic part. Properties steel were observed from tensile test. The data for steel model are shown in Table 4.3 for both stirrup (D8) and main bar (D25). In CDP model, the dilation angle **ψ** was considered as 40°, the shape factor, K_c = 0:667, the stress ratio σ_{b0}/σ_{c0} = 1.16 and the eccentricity **ε** = 0.1.

Table 4.3: Steel parameters

Diameter	E_s (GPa)	ν	f_y (MPa)	f_u (MPa)	ε_u (-)
D25 (main bar)	200	0.3	535	650	0.13
D8 (stirrup)	200	0.3	650	700	0.17

4.2.4. Analysis results

a) Optimization of mesh sizes

The Figure 4.18 shows load-deflection response for different mesh sizes: 10 mm, 15 mm, and 25mm from the model of beam N08. The load-deflection curves from analysis shown in the figure were cut off the last part when the load drop down to the value of less than 50% of maximum applied load.

The outcome from analysis demonstrates the higher stiffness as small deflection, but then reduce to become smaller than experimental stiffness when deflection increased.

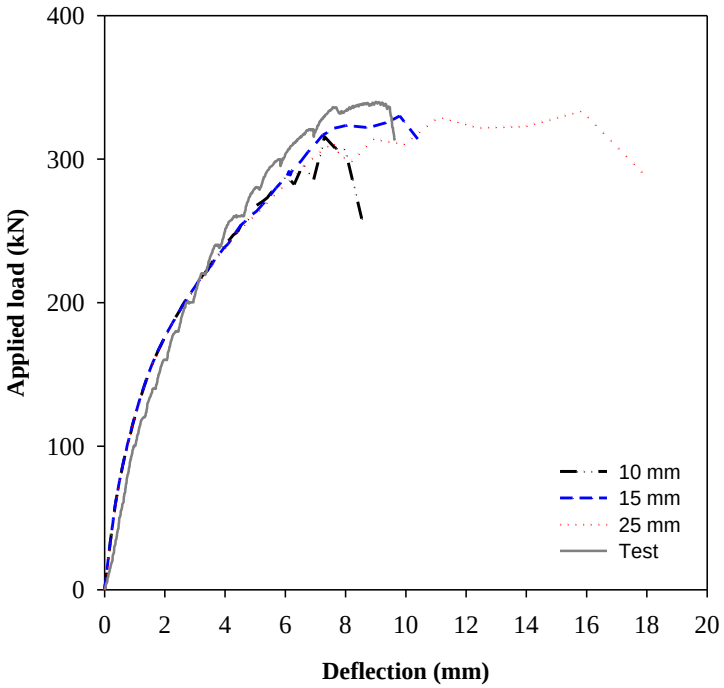

Figure 4.18: Load-deflection response of beam N08 for different mesh sizes

Table 4.4: Comparison of failure load and deflection from test and numerical analysis

Test/ Model	Load capacity (kN)	Difference from test results (%)	Failure deflection (mm)	Difference from test results (%)
Test	340.1	-	9.01	-
10 mm	315.7	-7.2	7.31	-18.9
15 mm	330.1	-2.9	9.80	8.8
25 mm	333.7	-1.9	15.83	75.7

Table 4.4 compares the load and deflection at the failure point from test and those three models. It is clearly that three mesh sizes show similar results in term of failure load and stiffness, the curves are closed to each other before failure. But the analysis results are mesh size dependent if considered in term of failure displacements.

The mesh size of 15 mm gave the most accuracy load-deflection behavior among three, compared to experimental result. While the mesh size of 10 mm shows the earlier failure because of local failure in some elements, the mesh size of 25 seems like too coarse and could not converge to create shear failure instead of ductility. Afterward, the mesh size of 15 mm was chosen in all subsequent simulation of all beams.

b) Verifying material constitutive law

The comparison of analysis and experimental results of three beams were found in Figure 4.18 and Figure 4.19. It is clearly seen that analysis predicted behavior of beam well. Beam N08 and N16 without stirrup failed under shear failure, while the beam W08 with stirrup failed under flexure mode as same as experiment. Table 4.5 shows load capacity (load at yield point for beam W08) and failure deflection (deflection at yield point) of three beams. There are small differences between analysis and experiment in load capacity, but analysis demonstrated good agreement in term of failure point, and failure mode.

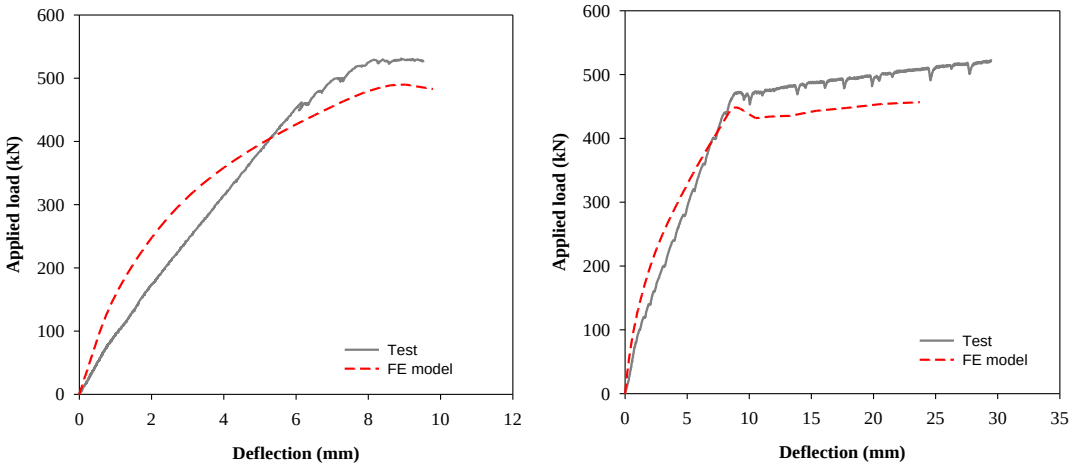

(a) (b)

Figure 4.19: Comparison of load-deflection response from test and model: (a) N16 and (b) W08

Table 4.5: Comparison of FEA and test results

Beam	Load capacity from **FEA**/test (kN)	Difference from test results (%)	Failure deflection from **FEA**/test (mm)
N08	**330.1**/340.1	-2.94	**9.80**/9.01
N16	**489.9**/530.9	-7.72	**8.36**/8.91
W08	**448.4**/472.9	-4.97	**8.99**/9.15

The following part investigated the new model with changing fiber orientation of UHPFRC. At first, suitable number of divided parts were found by comparing results from different models. Figure 4.20 and Figure 4.21 compared the load-deflection responses and cracks patterns from the original model (the model with only one tensile stress-strain curve and without considering fiber orientation effect, which presented in the previous part) (case 1), and the models with different applied materials in considering effect of fiber orientation (case 2).

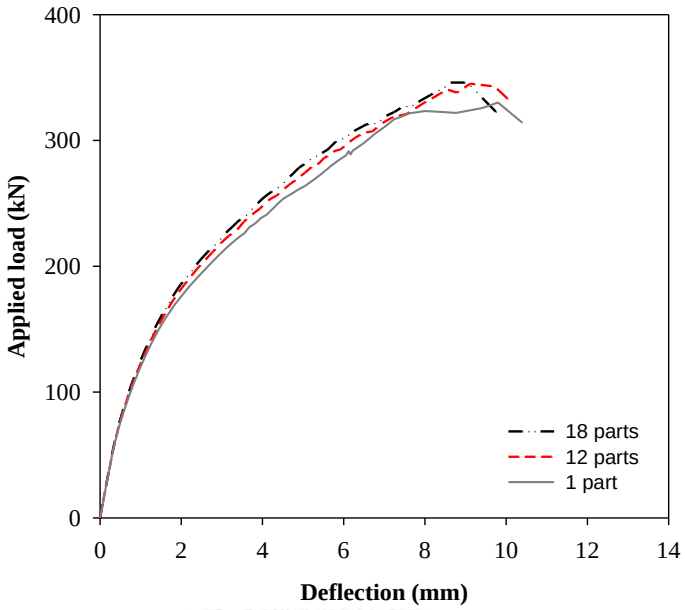

Figure 4.20: Load-deflection response of beam N08 from the different models

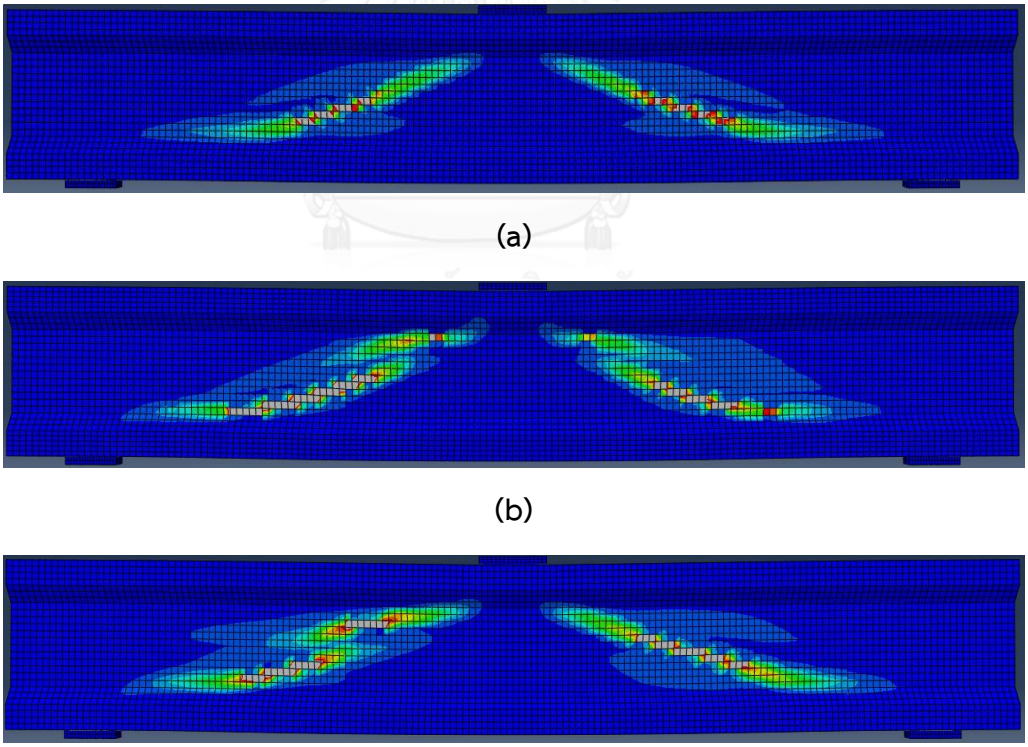

Figure 4.21: Comparison of cracks patterns from the different models: (a) 1 part, (b) 12 parts, and (c) 18 parts

The load-deflection behaviors show the similar in term of maximum load and slightly difference in post-crack stiffness and failure deflection. The model of the finer parts with 12 parts and 18, the failure deflection seems to be same as its value of the original model. The load-deflection curves from 12 parts and 18 parts model presents the same behavior, such as stiffness, load capacity and failure deflection. The cracks patterns shown in Figure 4.20 seem to be similar among three models. Therefore, 12 divided parts could be enough to represent the change of material properties, and it could use for the other analysis.

The same procedure was applied for the beam N16 and W08. The results were shown in Figure 4.22, Figure 4.23, and Table 3.7 for all three beams.

By applying new approach, load-deflection behavior was changed from the original model. Both load capacity and post-crack stiffness increased, while failure deflection did not change. Table 4.6 illustrates the difference in load capacity and failure deflection between two models. By applying different material properties at different distances from casting point, the shear load capacity of the beam without stirrup, N08 and N16, increase 4.5 % and 3.86 %, respectively, while the deflections at failure point are closed to each other. The stiffness from the two models are similar before cracking, then tend to differ as increasing deflection.

Table 4.6: Comparison of shear failure from different models of three beams

Slab	**Random distribution**		**Orientation consideration**		**Difference of load capacity (%)**
	Load capacity (kN)	Failure deflection (mm)	Load capacity (kN)	Failure deflection (mm)	
N08	330.1	9.01	345.1	9.12	4.54
N16	489.9	9.03	508.8	8.36	3.86
W08	448.4	8.99	455.3	8.99	1.56

For the beam W08, because of adding stirrup, the beam was failed in flexure mode. Figure 4.19 depicts the load-deflection responses that obtained from experiment and analysis. The modelled beam failed under flexure and presented the identical load-deflection behavior. It is clearly seen that the applied load at yield point of the steel from the analysis is slightly smaller than the test result, but it occurred at same deflection. For the new approach model in considering fiber orientation effect, the beam was modelled as same procedure with beam N08.

The load-deflection behaviors are illustrated in Figure 4.23 to compare new approach and original model. It looks like there are no different from two models, including stiffness, load capacity and load at yield point of steel. The difference of applied forces at yield point is less than 1%. Cracks patterns in the beam from experiment and models can be found in Figure 4.26. Because of changing fiber orientation along the beam and then asymmetry of material properties, cracks were not symmetrical in the new approach model. But cracks patterns generally meet agreement with the test results. As same as experimental results, many cracks occurred in two sides of the beam, and the huge cracks at the middle of beam finally established caused flexural failure.

Furthermore, because there are observed strains in the stirrups of beam W08, the accuracy of the model and comparison of two models could be carried out. Figure 4.24 compares strain in stirrups obtained from experiment and the models. Due to the asymmetry in material properties of model 2, strains were obtained by averaging the values from two sides of the beam. The comparison showed clearly that the analysis results predicted the stress development in stirrup well. Furthermore, there are not significant differences in strain observed from the models in two cases. It can be concluded that with the presence of an amount of steel as stirrup, the effect of fiber orientation is insignificant.

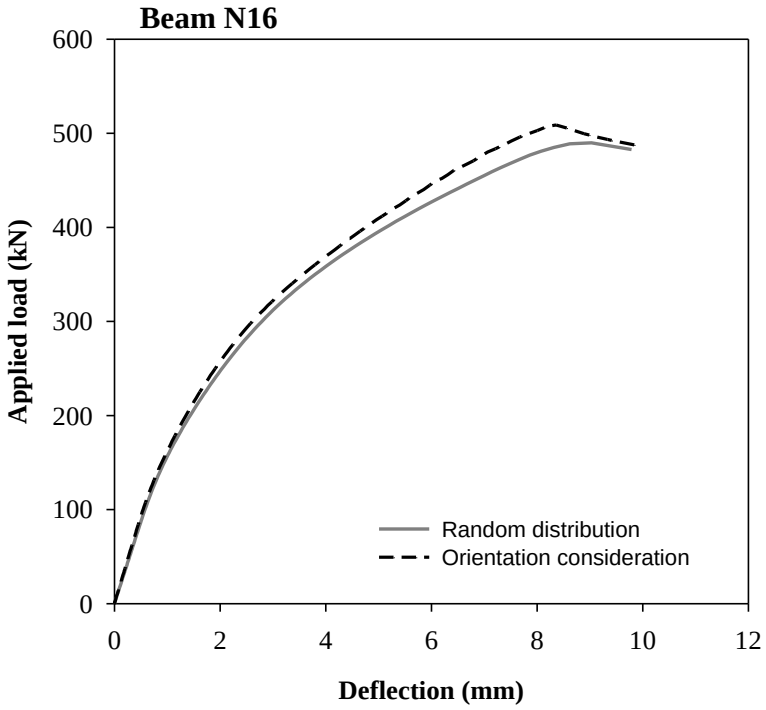

Figure 4.22: Comparison of load-deflection response from original and new approach models.

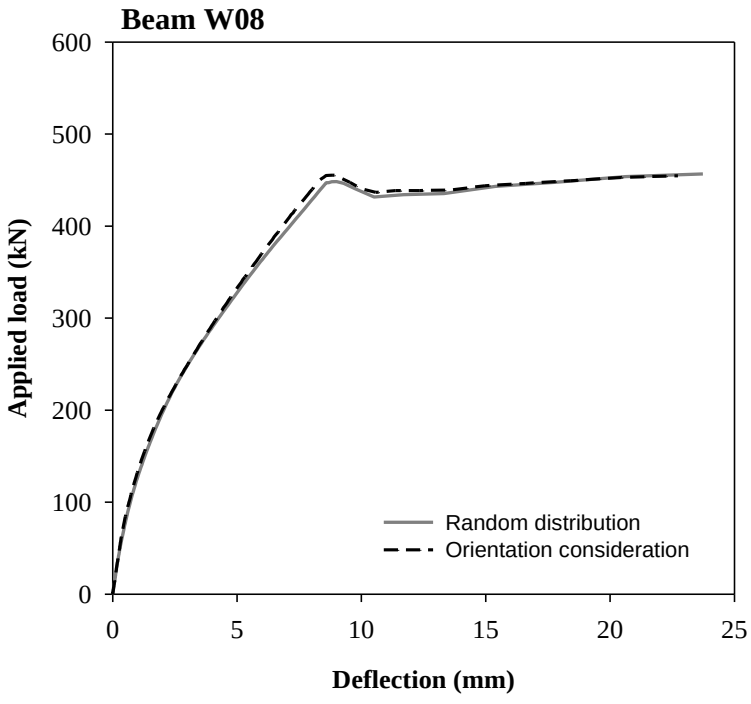

Figure 4.23: Comparison of load-deflection response from original and new approach models.

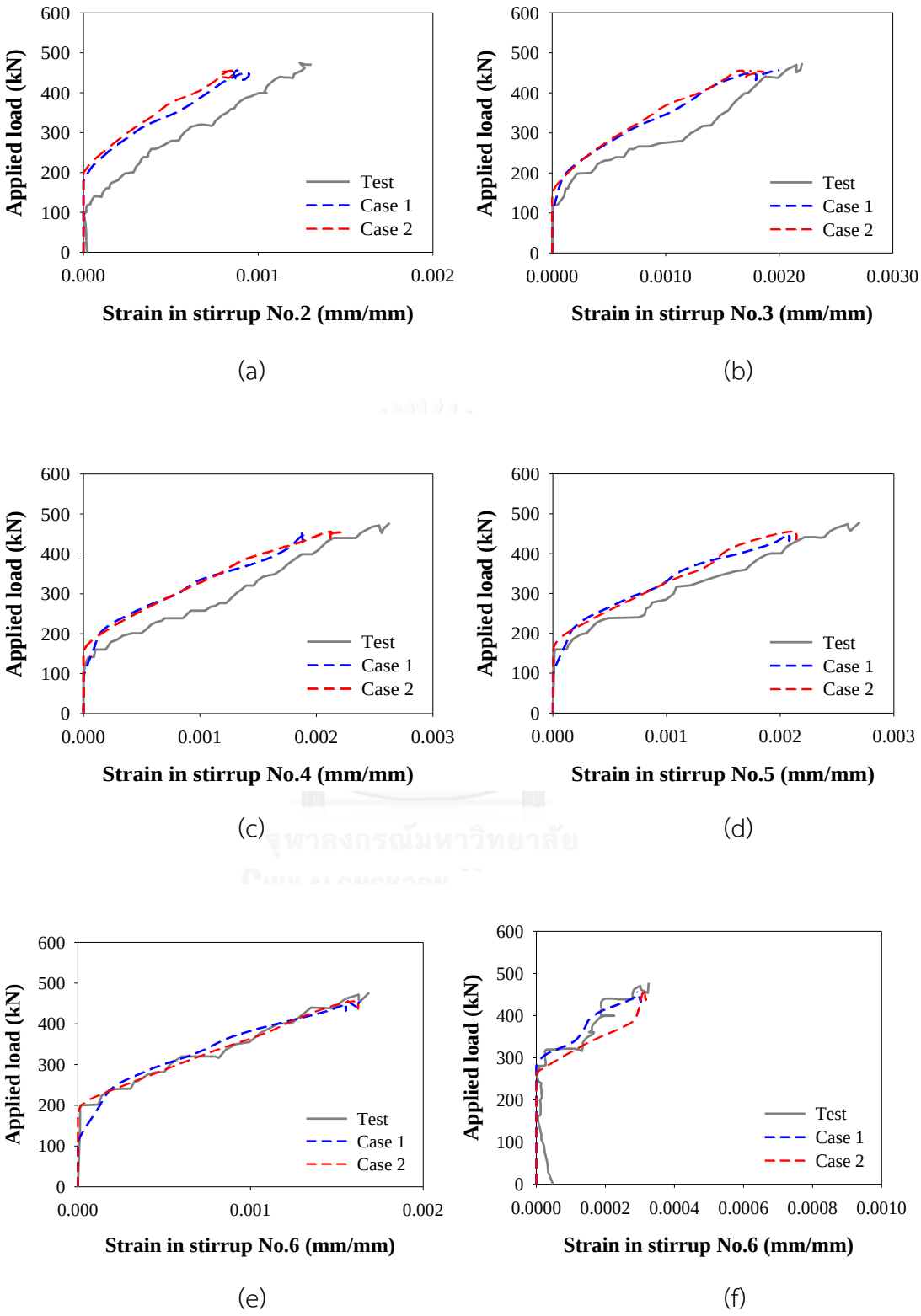

Figure 4.24: Comparison of stirrup strain from the models and experiment

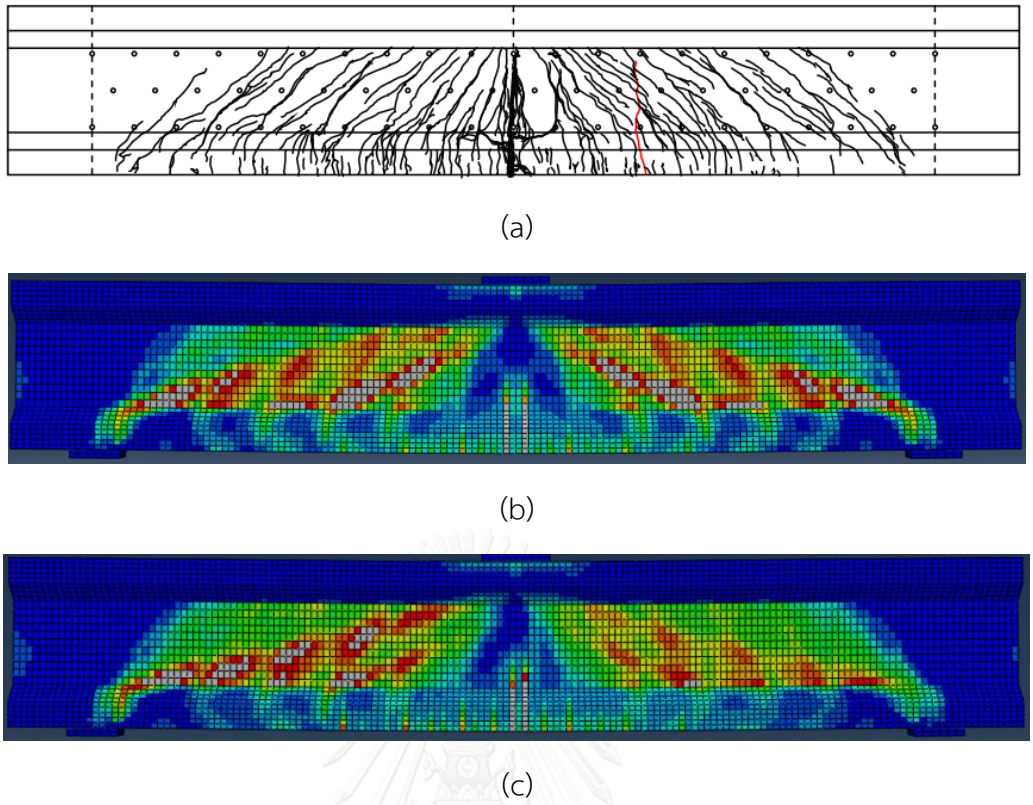

(a)

(b)

(c)

Figure 4.25: Comparison of cracks patterns of beam W08: (a) experiment, (b) original model, and (c) new approach model

4.2.5. Conclusion

All of the results showed that FEA could predict well the behavior of I-beam under three-point bending test, including mode of failure, load deflection behavior, ultimate load capacity, strain in stirrups, and cracks patterns. The following conclusion can be drawn:

- Three mesh dimensions were applied to simulate UHPFRC element with aspect ratio of 1. The mesh size of 15 mm of C3D8 element presented the best results in the prediction behavior of I-beam, while the others (10 mm and 25 mm) are too coarse of too fine. Consequence, size of 15 mm is suitable to simulate behavior of UHPFRC material.
- The analytical model that represents strain hardening behavior of the material, starts at cracking stress and ends at maximum, showed the good agreement

with the curve from direct tensile test. The cracking stress could be calculated from compressive strength, however, the direct tensile test is necessary for determination of ultimate strength. The proposed model demonstrated the distinct curves for each value of fiber orientation according to distance from casting position. As far as casting position, tensile model exhibited higher value of tensile strength and the length of strain hardening part.

- Embedded formulation of steel was used to represent steel in concrete material. It not only gives the simple way to model, but also predict the deformation of steel reinforcement with reasonable results.
- By applying the new approach of material model and assignment manner, the effects of fiber orientation were figured out. For the presented I-beams, compared to the original model, the failure modes are similar, and the load-deflection behavior did not change significantly from the original model. The highest change is nearly 5 % for the beam N08, and there is only 1.6 % difference in the beam W08. It can be concluded that effect of fiber orientation in behavior of the beam is insignificant. However, the change would give a sense of range of load capacity in designing UHPFRC beam under considering the effect of fiber orientation.

4.3. Slab properties

4.3.1. Experimental procedure

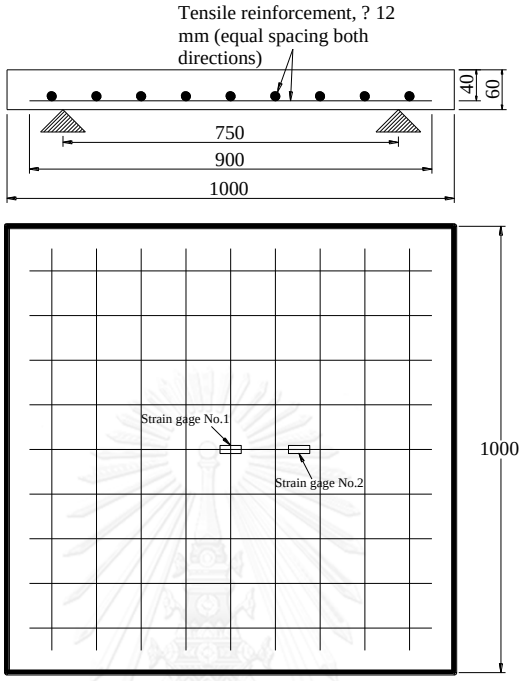

Figure 4.26: Dimensions and reinforcement details

The flat slabs were designed with a dimension of 1000 mm in both side, had the same thickness of 60 mm, tensile reinforcement ratio of 2.54 % and also the same tensile reinforcement configuration. The variable parameters among these specimens are: the fibers volume ratio varying from 0 to 1.6 % and the fibers orientation due to the difference in casting position [65]. The following figure show the casting positions in casting concrete and test setup.

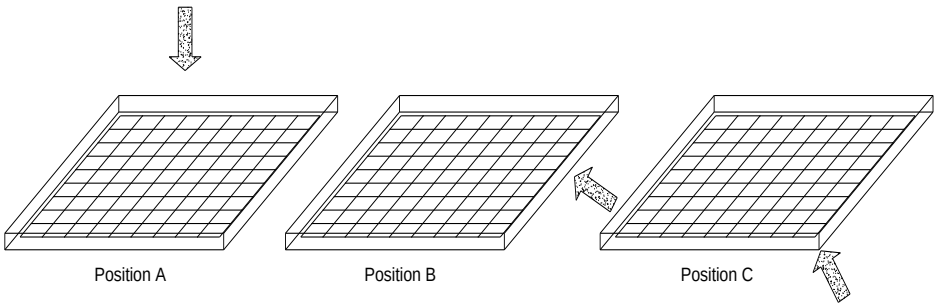

Figure 4.27: The pouring concrete positions [65]

The slabs were simply supported along four edges and the corners were free to move, and the concentrated load was applied at the center of the slab through the 80-mm load link, as shown in Figure 4.28. Due to the symmetry of the slab, five linear variable differential transducers (LVDTs) were installed to determine the vertical deflections of the specimens, one LVDT was attached at the middle point of the bottom surface of the tested slab, and another four LVDTs were positioned on the loading surface, in which two LVDTs were at the quarter of the span of the slabs and the other two were at the corners to determine the movement of the slab corners.

The LVDTs and strain gages on steel reinforcement were connected to a control system and recorded by a data logger model EDX-100A produced by Kyowa, Inc. The data were recorded every 0.1 seconds until failure of each slab. All of the equipment and machines are shown in Figure 4.28 and 4.29 as follows.

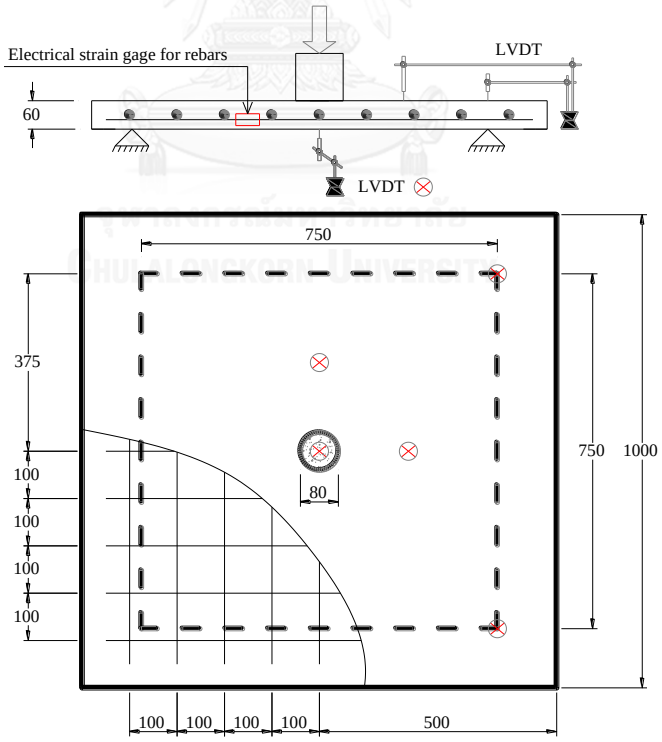

Figure 4.28: Details of the test arrangement

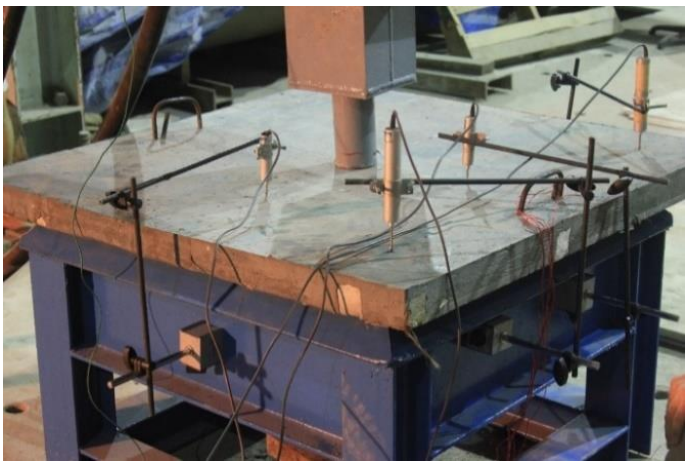

Figure 4.29: Test setup [65]

4.3.2. Material properties

Material properties were determined from cylinder compressive and splitting tensile test, the basic properties are shown in Table 4.7.

Table 4.7: The information of each slab [65]

Slabs No.	f_c (MPa)	f_{spt} (MPa)	E (MPa)	Mearured slab thickness (mm)	Tensile reinforcement ratio ρ (%)	Fibers volume V_f (%)	Casted positions
S-02	97.8	8.2	37.98	59.0	2.54	0.8	Position C
S-03	98.5	8.6	38.11	58.0	2.54	0.8	Position B
S-04	87.8	7.6	35.98	61.5	2.54	0.8	Position C
S-05	86.8	11.7	35.78	60.0	2.54	1.6	Position C
S-06	99.0	12.1	38.21	64.0	2.54	1.6	Position B
S-07	96.5	11.8	37.72	58.25	2.54	1.6	Position A

4.3.3. Test results

From the punching shear tests, load-displacement curves were observed, the results show the difference for each slab, because of difference in properties of mixtures.

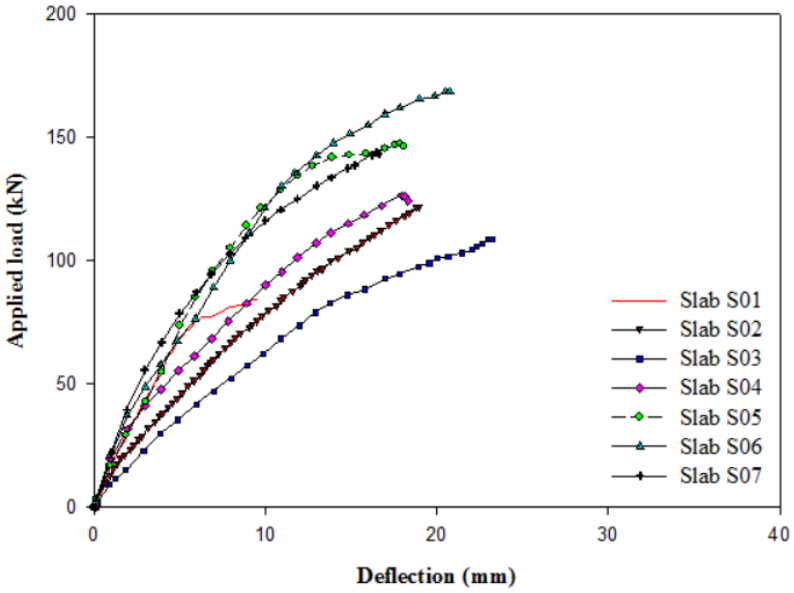

Figure 4.30: Load-displacement curves from experiment [65]

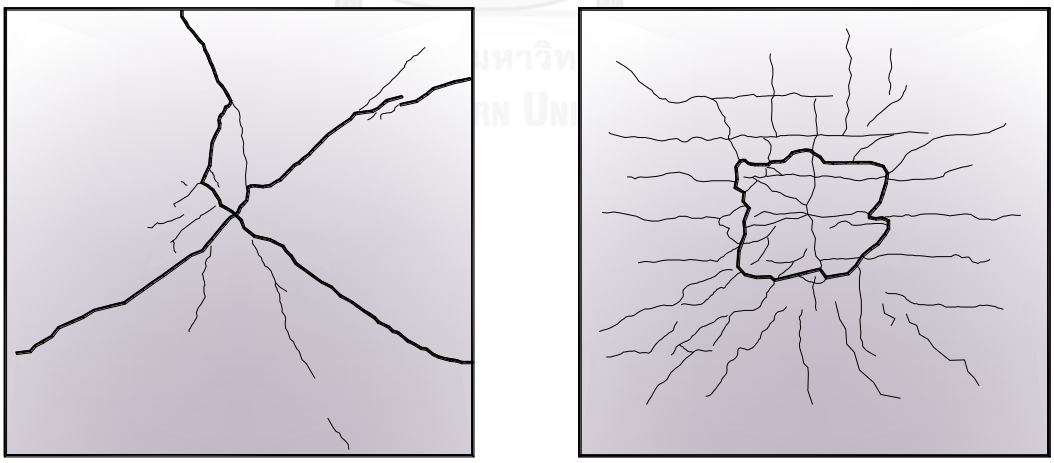

(a) (b)

Figure 4.31: Difference in failure of slabs: (a) slab without steel bar, (b) slabs include both steel fibers and steel bar

When the slabs failed by punching shear, truncated cone appear around the loading area. So the cone shape and size can be observed, which are also different for each slab.

From the test, five strain gauges were tightly bonded to steel bars, which across the center of the slabs, including one at the center and four in four opposite side. Strains in steels were also observed in a slab shown in following figure.

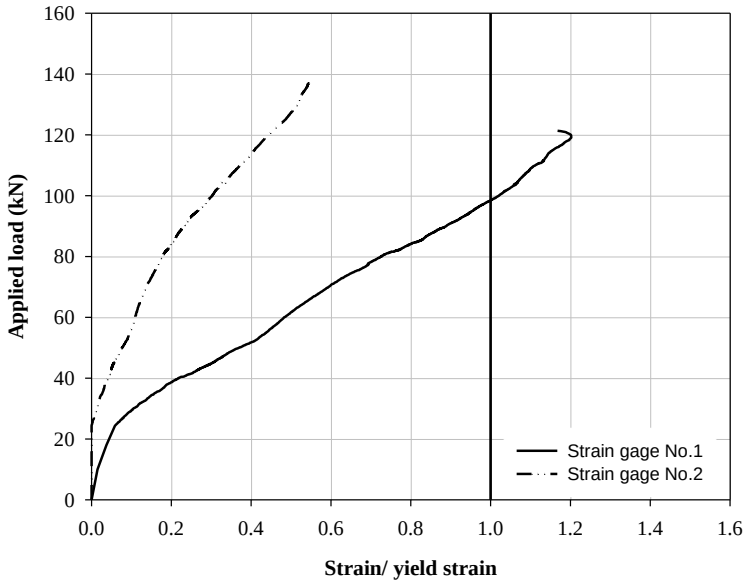

Figure 4.32: Strain in different positions of steel bar according to applied load

4.4. Numerical model of slabs

4.4.1. Fiber orientation in the slabs

As mentioned in literature, when the fresh FRC composite was cast at a position, led to radial spread and flow around that position [31, 32, 67]. The flow of fresh composite then generated the orientation and distribution of fibers, then fibers align along that flow. With the same idea and experience from previous studies, the presented study assumes that fresh concrete spread and flow similarly around casting position. The detail of the fresh concrete flow of each casting position in this study is shown in Figure 4.32.

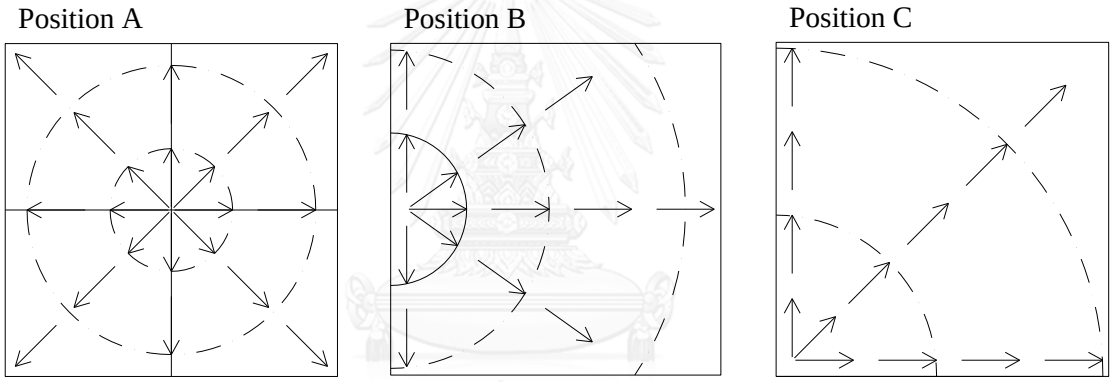

Figure 4.33: Flow of fresh concrete in each casting position case

4.4.2. Model concept

In each case, different distances from casting point induced different material properties, particularly its tensile model. The material model that presented in the previous chapter were applied, and, the same model procedure from the beam modelling would be performed to model punching shear behavior of the slabs. However, the studied slabs were considered as two-way slab, and the fiber orientation at an element represented different values in two directions, so the fiber orientation coefficient in two perpendicular directions would be taken into account. The model with applying fiber orientation of perpendicular sections was named as **case 2**, and

the other model with applying fiber orientation of perpendicular sections was named as **case 3**, as shown in following figure. By applying the results from Grunewald's experiment, different fiber orientations in two directions are created as a function of distance from casting position. Figure 4.34 as following shows the model procedure of the slabs.

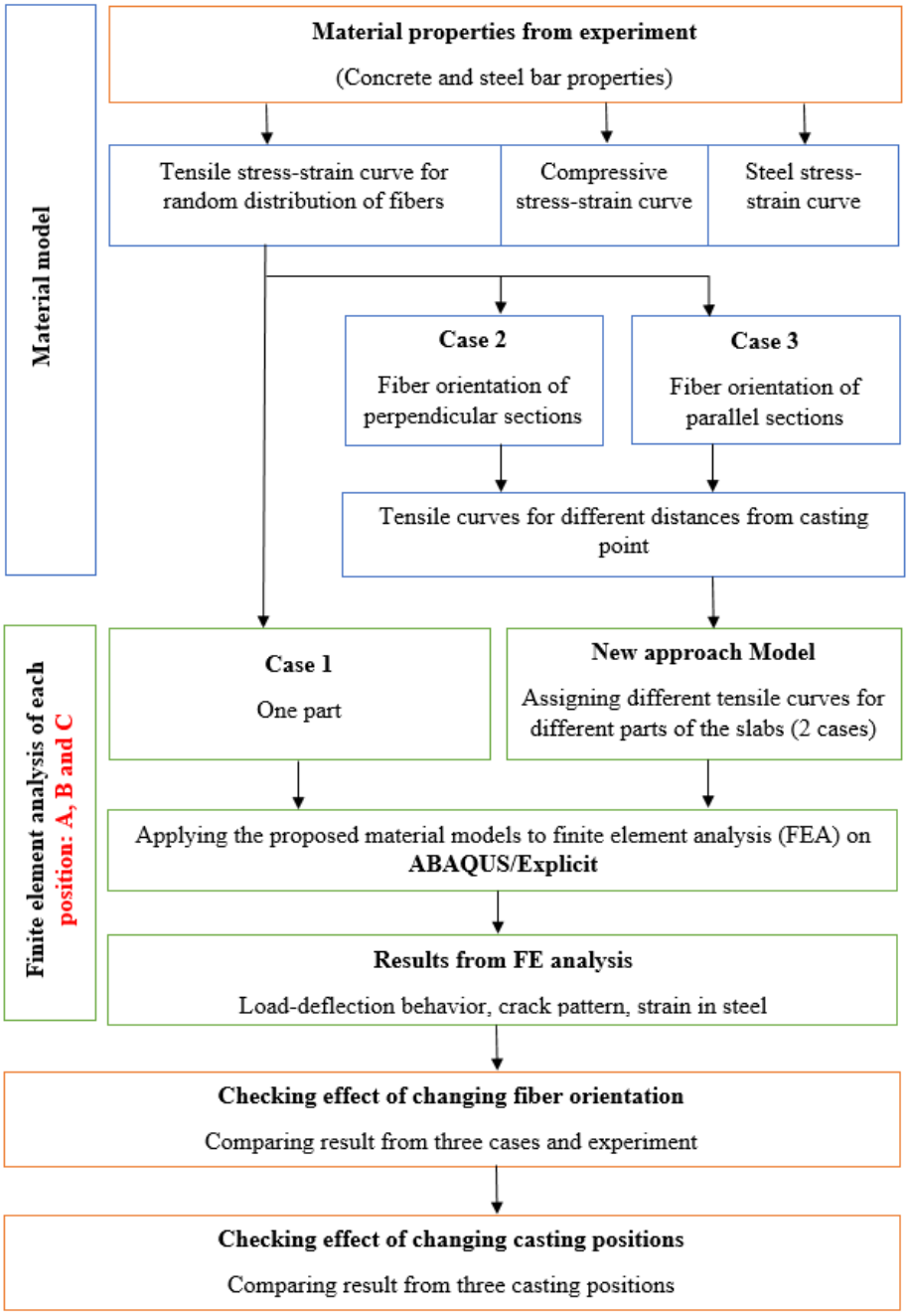

Figure 4.34: Flowchart of model procedure for the slabs

Number of divided parts of slab to assign material properties was considered as a parameter to decide sufficient divided parts. In the beam model, sizes of those divided parts were varied within 2 models: 100x100 mm (25 parts), 200x200 mm (100 parts), which shown in Figure 4.35 as follows.

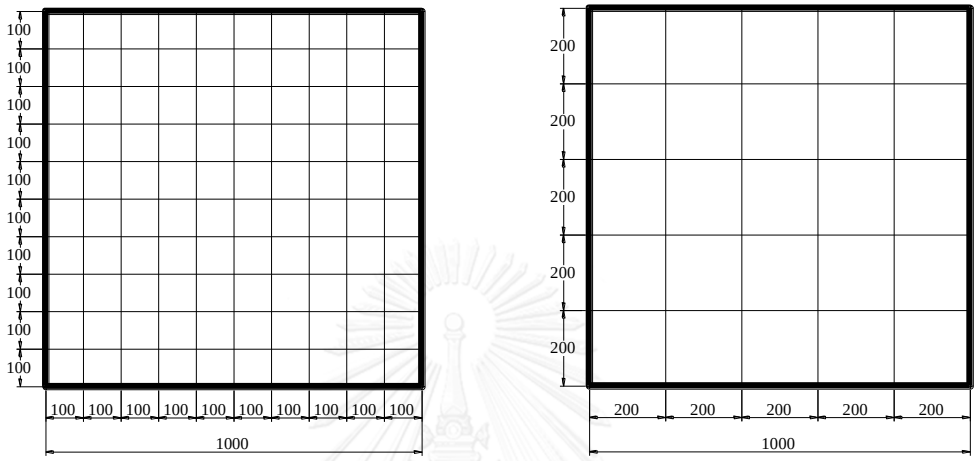

Figure 4.35: Schema of slab divisions with: (a) 100 parts and (b) 25 parts

In each case of division, the distances from casting position to each part were calculated (shown in Figure 4.36) then applied to the material model determine input data. With each value of distance, two tensile curves were created for two different directions. Modelling concrete in ABAQUS normally uses concrete homogeneous element with unique material property. Therefore, each tensile stress-strain curve was applied separately as considering a critical behavior of material in tension.

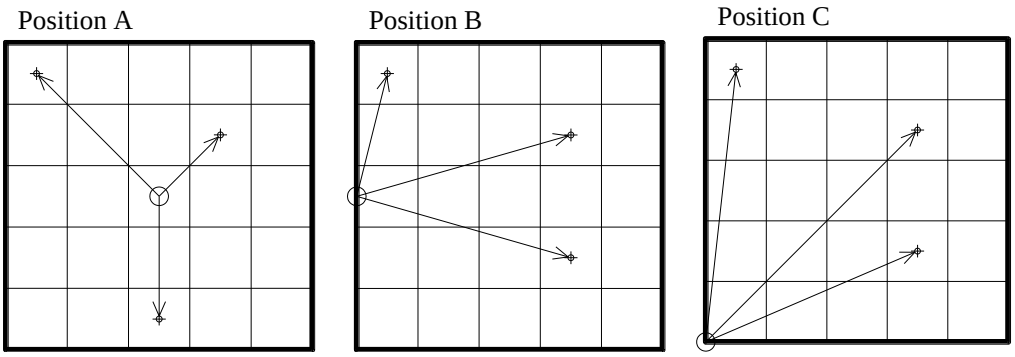

Figure 4.36: Schema of distance calculation

4.4.3. In ABAQUS/Explicit

a) Geometry and boundary condition

The slabs were simply supported along four edges and the corners were free to lift up. Though the slabs are symmetrical in geometry, properties of material in each position in each slab are different, therefore, the whole slab was modelled (see Figure 4.37). The concentrated load was applied at the center of the slab through the 80-mm load link. It was simulated by uniformly distributed load over the element representing the steel plate, and the supports were represented by four cylinders at four sides. The interaction of the plate or cylinder and the slab was represented as frictionless in tangential direction, and hard contact in normal direction. This interaction allows slab could move up and slide on the supports.

b) Element type and mesh size

8-node brick element (C3D8) which available in ABAQUS/Explicit was used to represent concrete element, and 2-node truss element used for steel bar reinforcement. Steel bars were simulated as embedded in concrete element at the specified location in the beam without bond-slip between two elements. The other consideration is that there is no bending stiffness in embedded truss elements, therefore, dowel action mechanism of the longitudinal steel reinforcement does not contribute to shear behavior.

As same as the beam model, study in mesh dependence was performed to figure out the optimal mesh size. The mesh sizes of 3D elements were varied with an approximate aspect ratio of 1. Three mesh sizes were applied in this part: 10 mm, 15 mm, and 20 mm. The best mesh size that shown the best fit with experimental results was used for the others. Steel bars were meshed with the size of 10 mm. Figure 4.39 shows an example of the mesh mapping of the slabs.

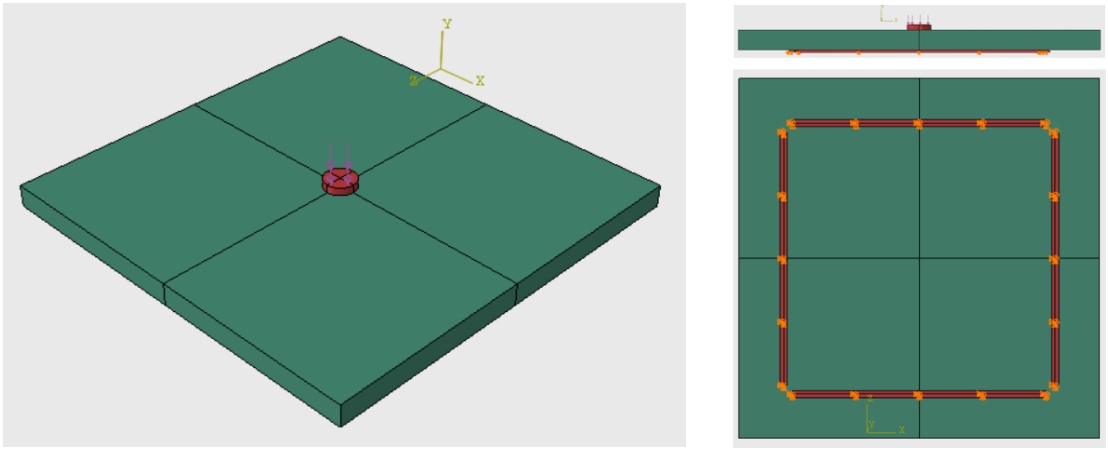

Figure 4.37: Model in ABAQUS

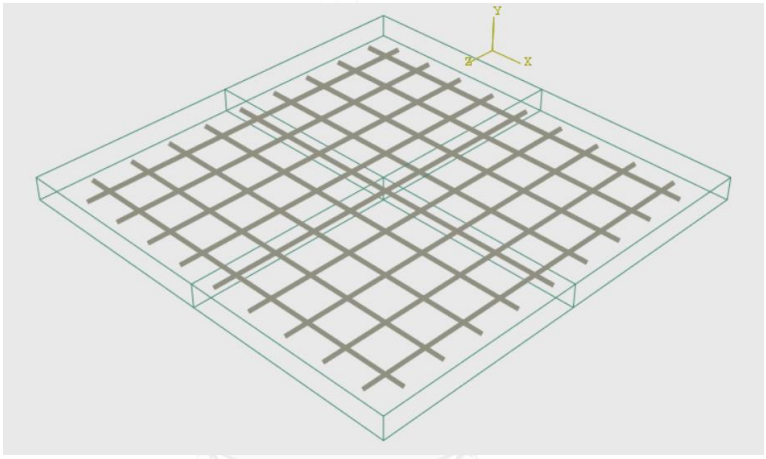

Figure 4.38: Present of tensile steel bar in slab model

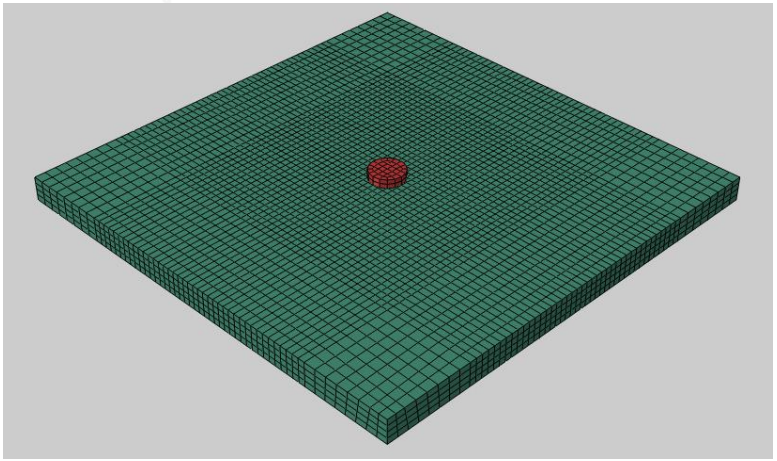

Figure 4.39:: An example in mesh mapping

4.4.4. Material model

a) Tensile behavior

In the experiment of the slabs, the direct tensile test was not performed, led to lack of tensile strength that need to create tensile model. However, the compressive test and splitting tensile test were carried out. Based on the ratio of tensile strength and splitting tensile strength of the beam for each percentage of fiber, the tensile strengths of the slabs were calculated from those ratios and splitting tensile strengths observed from the test. The following table presents estimated tensile strength of the all slabs.

Table 4.8: Calculated tensile strength of the slabs

0.8% of fiber				**1.6% of fiber**				
Beam test	S02	S03	S04	**Beam test**	S01	S05	S06	S07
15	8.2	8.6	7.6	**16.4**	12.5	11.7	12.1	11.8
6.06	3.31	3.47	3.07	**9.00**	6.86	6.42	6.64	6.48

The other two parameters used to create tensile model were strain at peak stress, and cracking strain. In this part of study, stress at peak stress was considered to be same as the tensile model of the beam models, and, cracking stress of composite was simply determined by cracking stress of concrete. Table 4.9 presents basic data for creating tensile model for the case with random distribution of fiber, then developing for varying fiber orientation.

The "***d***" value (the distance from casting position) of each part are determined by the distance between middle of that part and the casting point that at a corner, mid-point of a side or at the middle of the slabs. For each case of number of parts,

the distance would be calculated and then applied to the proposed model to figure out tensile constitutive curves.

Table 4.9: Parameters for creating tensile model

	S02-S04	S05	S06	S07
f_{cr} *(MPa)*	2.90	2.89	3.08	2.96
$f_{ct\ random}$ *(MPa)*	3.14	6.42	6.64	6.48
$w_{ct\ random}$ *(mm)*	0.228	0.355		
η_{random}	0.707			
f_{1D} *(MPa)*	9.1	18.60	19.24	18.76
w_{1D} *(mm)*	0.45	0.7	0.7	0.7
L (mm) (*)	110			

(*) Length of measurement of the direct tensile test specimens

b) The other numerical parameters in slab model

The other material parameters for UHPFRC material that were used in this study are: the modulus of elasticity E_c, the Poisson's ratio **ν**, and the compressive behavior of each slabs. The model from Mansur's study [7]was adopted to present compressive behavior of UHPFRC in this study. The strain at maximum compressive stress is a function of strength, fiber volume, and the aspect ratio of fiber. The Poisson's ratio was considered as 0.2 for all beams. Table 3.5 shows the parameters to create compressive stress-strain curve for each beam.

The other material parameters for UHPFRC material that were used in this study are: the modulus of elasticity E_0, the Poisson's ratio **ν**, and the compressive behavior of each slabs. Constitutive model in compression was presented in the previous chapter, by using Mansur model [7]. Table 4.10 shows the parameters to create compressive stress-strain curve for each beam. Steel bars were modelled by bilinear curve, including elastic and plastic part. The data for steel model are taken from tensile test of used steel bar, and shown in Table 4.11.

Table 4.10: Parameters for compressive model

	S05	**S06**	**S07**
f'_c *(MPa)*	99.0	86.9	96.5
ε_0 *(-)*	2.50e-3	2.39e-3	2.48e-3
E_c *(MPa)*	47.2	31.48	38.47
ν *(-)*	0.2	0.2	0.2

Table 4.11: Material parameters of steel bar

Diameter	**E_s (GPa)**	**ν**	**f_y (MPa)**	**f_u (MPa)**	**ε_u (-)**
D12 (main bar)	200	0.3	535	650	0.13

In CDP model, the dilation angle ψ was considered as 40°, the shape factor, K_c = 0:667, the stress ratio σ_{b0}/σ_{c0} = 1.16 and the eccentricity ε = 0.1.

4.5. Results and discussion

4.5.1. Case 1: The slabs with 1.6% of fiber: random distribution of fibers

a) Mesh dimensions

Slab with random distribution of fiber were modelled with different mesh sizes (10 mm, 15 mm, and 20 mm) to figure out the mesh dependence, and choose the best for further models. The slab S05 was used to model in this part of the study. The results were shown in Figure 4.40, Figure 4.41 and Table 4.12.

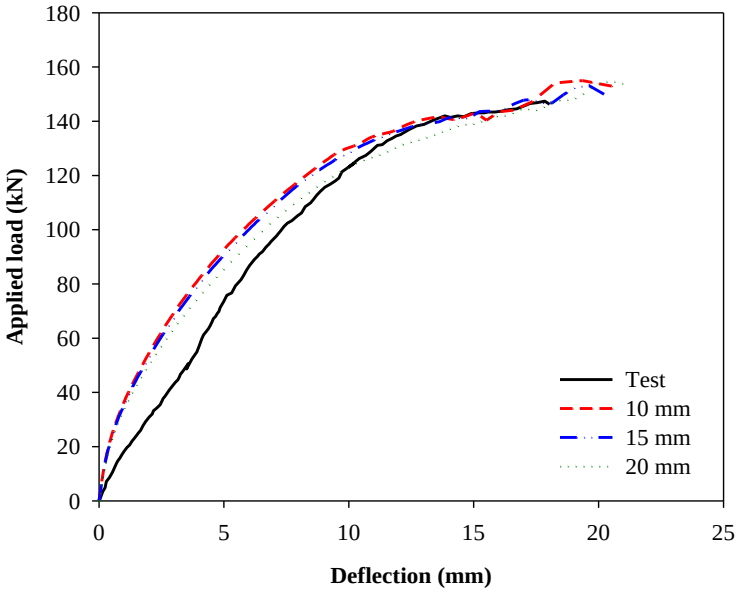

Figure 4.40: Load-deflection response from model of different mesh sizes

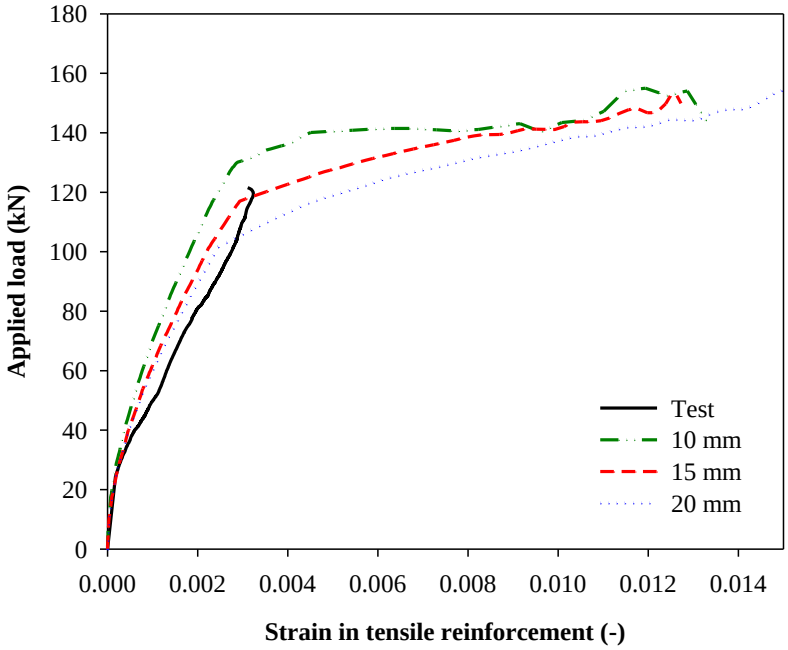

Figure 4.41: Load-strain in tensile steel bar response from model of different mesh sizes

Table 4.12: Comparison of failure point from test and numerical analysis of slab S05

Test/ Model	Punching shear capacity (kN)	Difference from test results (%)	Failure deflection (mm)	Difference from test results (%)
Test	147.4	-	17.8	-
10 mm	155.0	5.16	19.4	8.99
15 mm	153.2	3.93	19.6	10.11
25 mm	154.7	4.95	20.5	15.17

The responses of applied load-deflection at the middle of slab from different mesh sizes show the similarity in failure load and deflection. The responses are similar from model of 10 mm and 15 mm, while the model of 20 mm shows smaller stiffness than the others. However, the responses from deformation of steel are significantly different from three mesh sizes. The model of 20 mm presents lower value of applied load at yielding of steel, while the model of 10 mm shows the higher value, compared to experimental response. The model of 15 mm gives the best fit with experimental results. Afterward, the mesh size of 15 mm was used to simulate the further model.

b) Analysis results

Figure 4.42 and Table 4.13 compare the results between experiment and analysis in term of load-deflection responses plotted at the center and a corner of the slab. It is clearly seen that the applied load-deflection behaviors from analysis shown higher stiffness, compared to experimental responses. It can be explained that there are the gaps between slabs and support in the experiment, therefore, the deflection increased quickly at small applied load, and became stable when the applied load increased. On the other hand, the measured deflection at the corner of the slab from the experiment is larger than that value from FE model.

From the experiment, stresses in steel bar were measured at two positions as shown in Figure 4.26. Figure 4.43 compares strains in tensile reinforcement observed from experiment and model. At both two positions, experimental curve and analysis curve are closed to each other. The results showed that the analysis predicted the strain in steel bar well with the same trend of deformation and yielding point of steel.

Cracks patterns of slab observed from the FEA and experiment was illustrated in Figure 4.44 as following. Both testing and modelling results shows that the cracks started at the middle of the slab and propagate to four sides of the slab, then huge cracks formed at the center in directions according to direction of tensile reinforcement. Finally, slabs failed under flexural punching shear because of crushing of material in compressive zone, and cone failure could be observed. The failure of material observed from the bottom surface of the slab was shown in Figure 4.45, and the cone size could be observed from this visualization.

Table 4.13: Comparison of punching shear capacity and failure deflection between testing and modelling of three slabs

Slab	**Test**		**Finite element analysis**		**Difference of load capacity (%)**
	Load capacity (kN)	Failure deflection (mm)	Load capacity (kN)	Failure deflection (mm)	
S05/C	147.4	17.8	153.2	19.6	3.9
S06/B	168.4	20.5	159.3	19.5	-5.4
S07/A	143.9	16.5	153.7	19.6	6.8

Figure 4.44 demonstrates the principal stressed at different sections of the slab. It shows the high compressive stresses at the top surface and the high tensile stresses at bottom surface, the highest stresses focus at the center and becomes smaller as far

as the center. The principal stress of an element is definitely perpendicular to the direction from the center point to that element. Figure 4.45 captures the principal strains at the step before failure. The maximum principal stresses are perpendicular to direction of inclined critical shear cracks, therefore, the cone failure would form by increasing applied load and led to the failure of all of the slab.

In term of the cracks patterns, Figure 4.46 and Figure 4.47 demonstrate the visualization of cracks patterns at bottom surface in FE model at two steps of the slab before and after failure, compared to experiment results. The FE results shows the similarity to experiment, the principal cracks formed at the center and led to two sides of the slab. By increasing applied, cone failure formed and led to sudden failure of the slab.

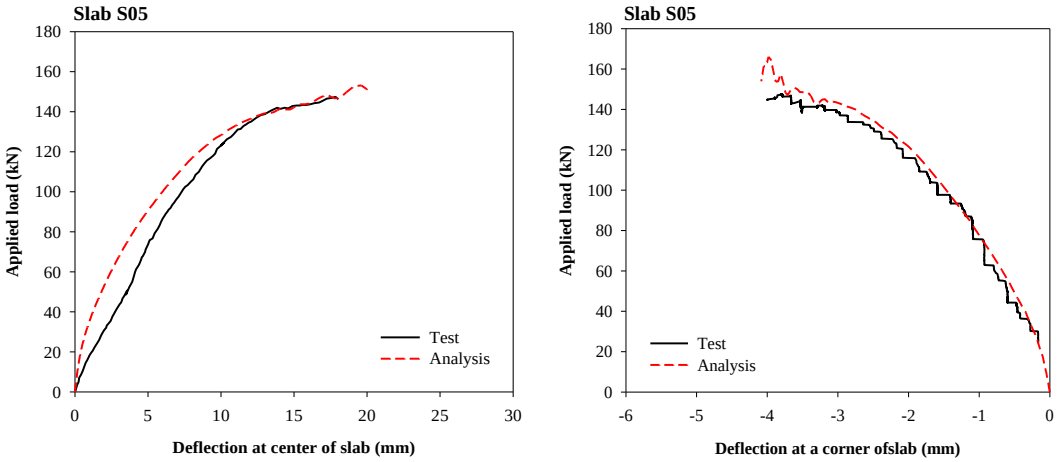

(a)

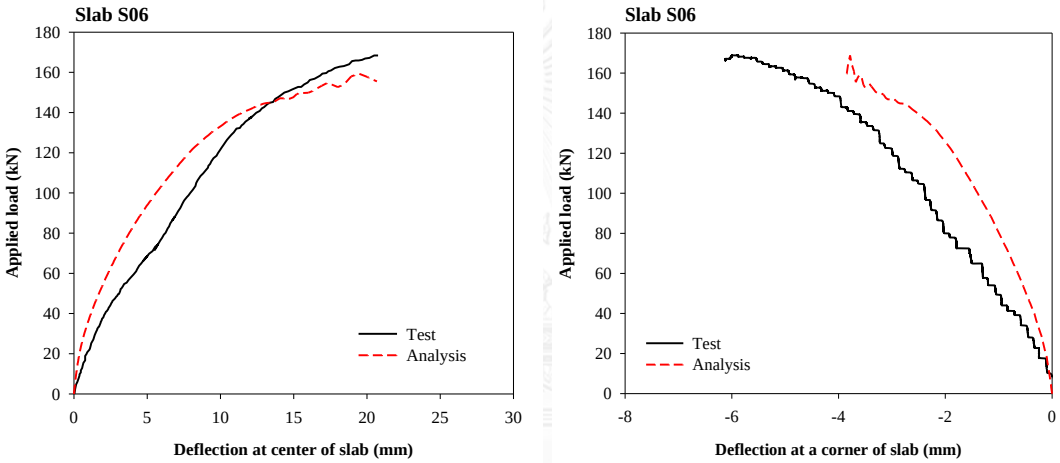

(b)

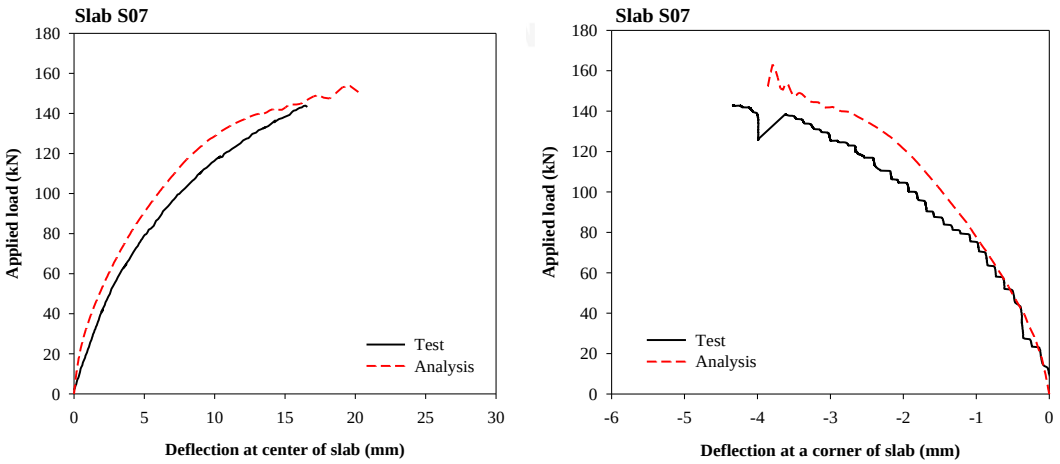

(c)

Figure 4.42: Comparison of responses of load-deflection at the center and at a corner from experiment and analysis of three slabs: (a) S05, (b) S06, and (c) S07

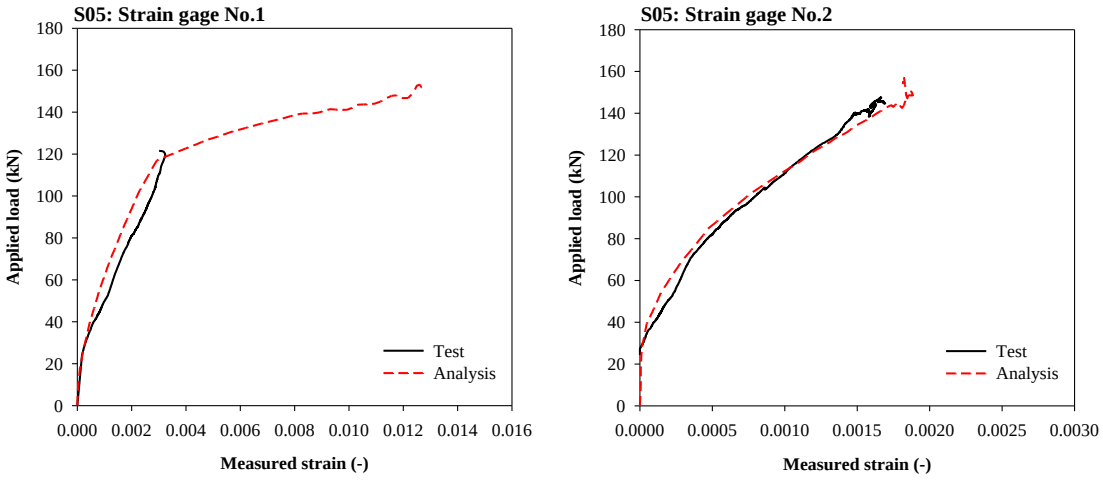

(a)

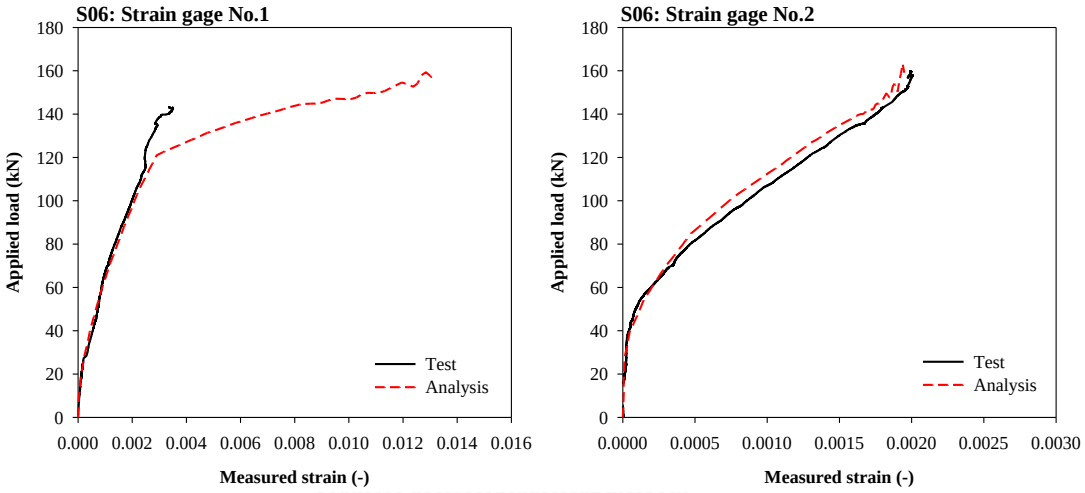

(b)

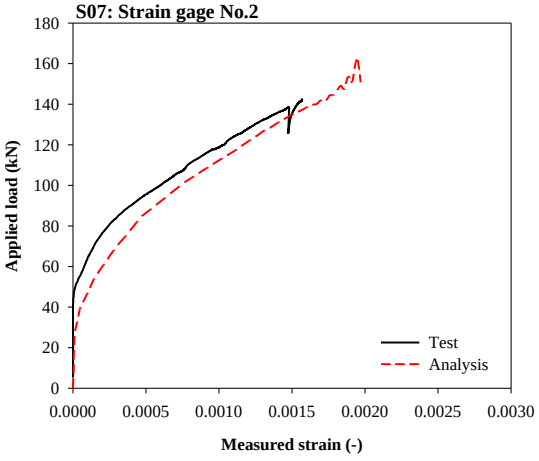

(c)

Figure 4.43: Comparison of steel stresses from experiment and analysis at different positions of steel bar of slab (a) S05, (b) S06, and (c) S07

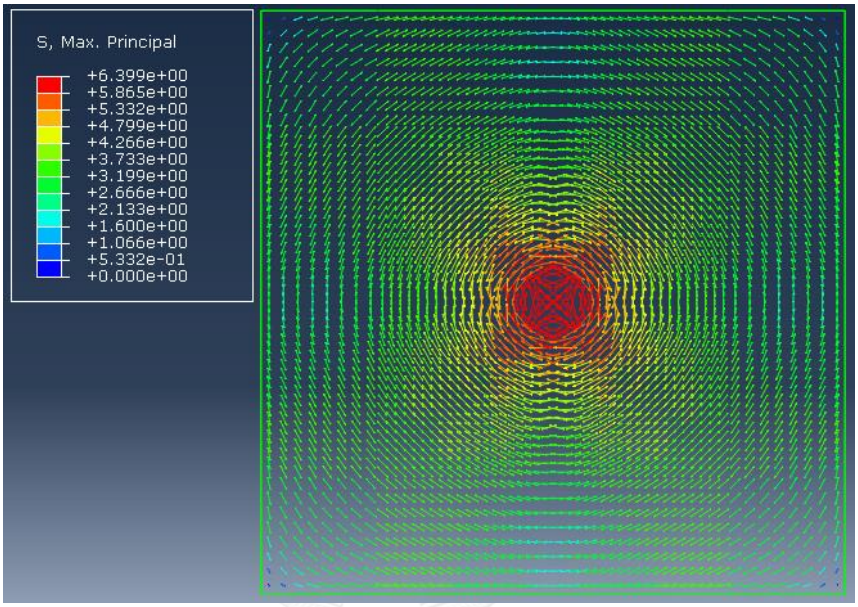

(a)

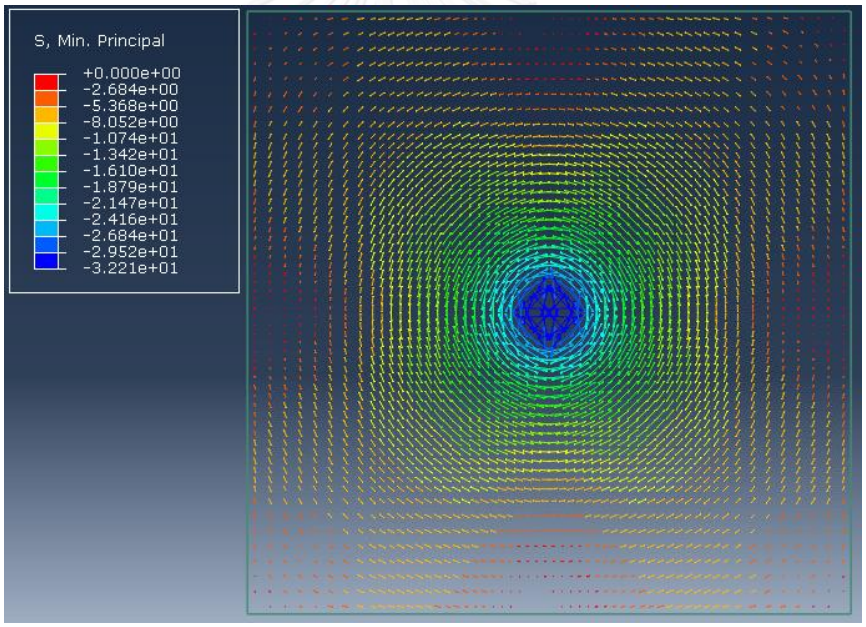

(b)

Figure 4.44: Principal stresses at the (a) bottom surface and (b) top surface of the slab

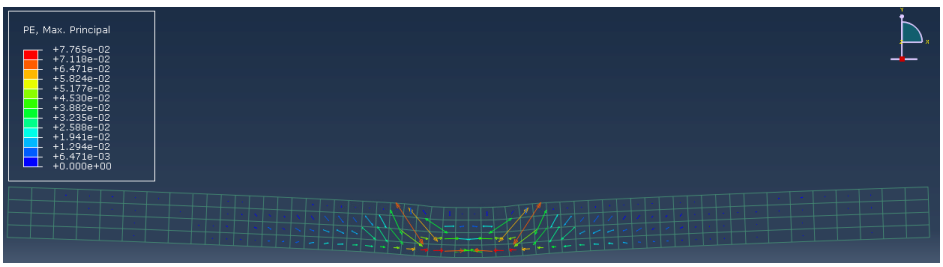

Figure 4.45: Principal cracking strain at the mid-span elements layer before failure

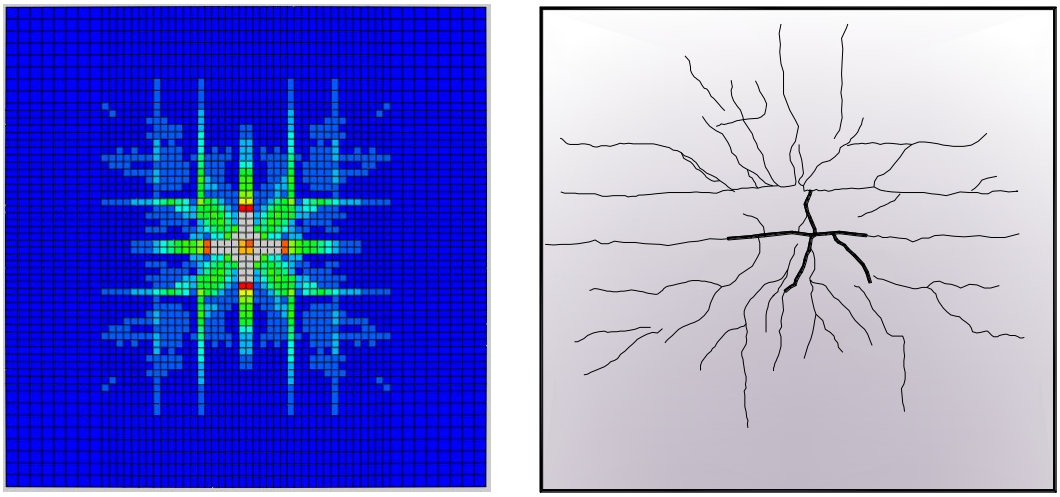

Figure 4.46: Comparison of cracks patterns from FE model and experiment

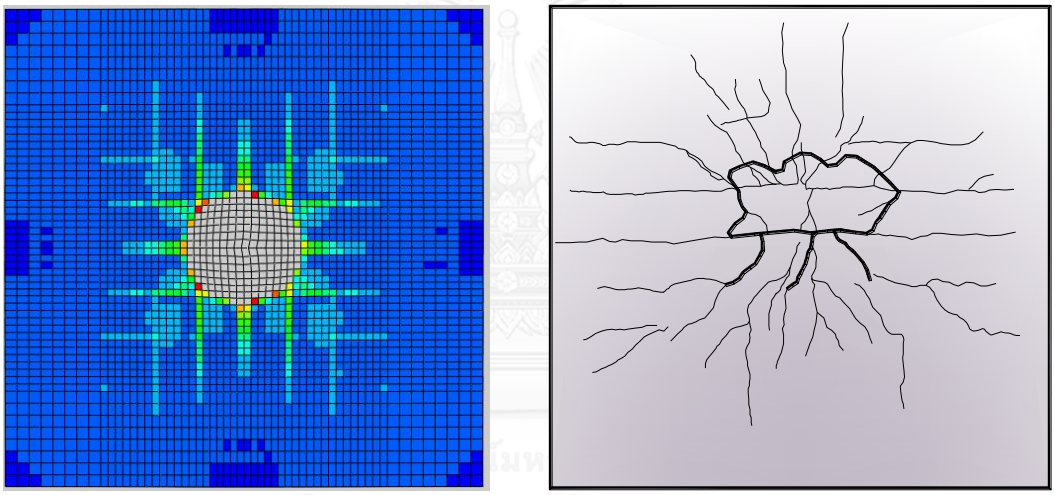

Figure 4.47: Failure of the elements at bottom surface of slab from FE model and experiment

4.5.2. Case 2: The slabs with 1.6% of fiber: changing fiber orientation

To apply different properties induced from different fiber orientation factors, the slabs were divided to many part to assign their properties. The fine divided part would lead to an accuracy result, compared to the coarse divided part. However, the fine divided part takes more time to perform analysis. In this part, two schemas of properties assignment were applied for comparison and choose the suitable schematic for further models.

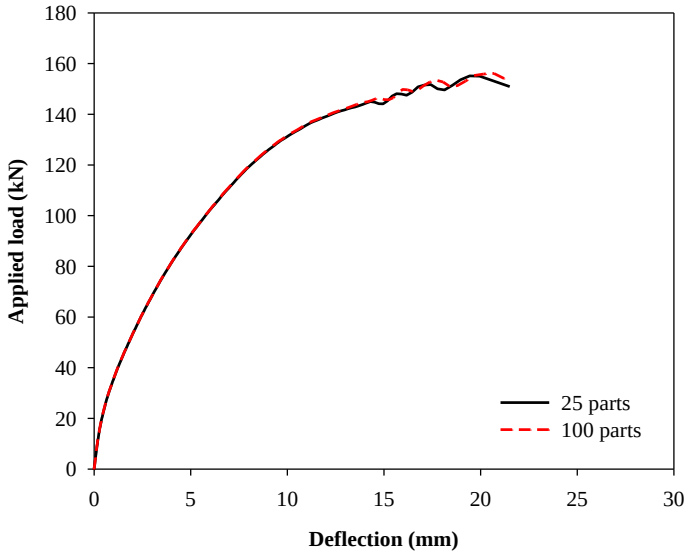

Figure 4.48: Load-deflection behavior from different schematics of properties assignment

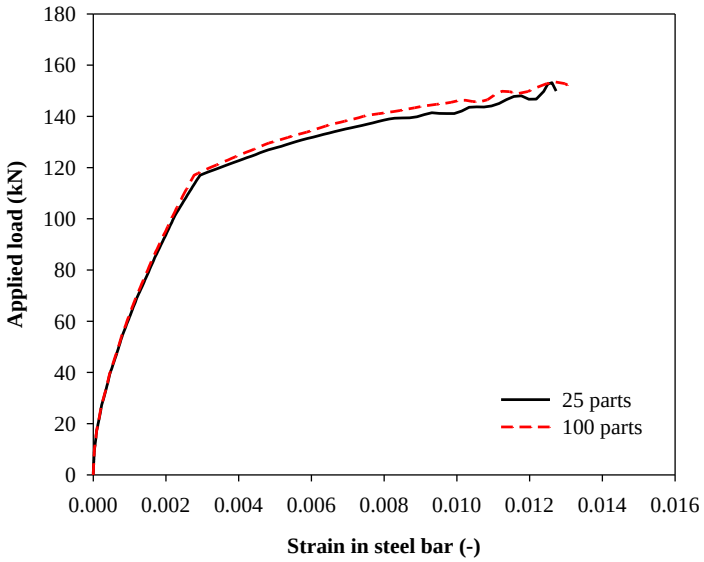

Figure 4.49: Load-strain in tensile reinforcement behavior from different schematics of properties assignment

Figure 4.46 and Figure 4.47 show load-deflection and load-strain in steel response of different schemas of properties assignment. It is clearly seen that there is no different between model of 25 parts and 100 parts in both load-deflection response

and load-strain in steel response. From this result, model of 25 parts of different tensile properties could give reasonable results to represent the purpose of changing fiber orientation in the slabs, and it should use for further models.

As mentioned in previous subchapter, two cases of fiber distribution, such as the increase and decrease trend of fiber orientation coefficient corresponding to fiber orientation of perpendicular and parallel sections, respectively, were applied to finite element analysis of each slab. In addition, the random case represents the case without changing fiber orientation in the slab, the properties of random distribution of fiber were used for analysis.

Table 4.14: Comparison of punching shear capacity and failure deflection between the models of different distributions of fiber of three slabs

Slab	Random distribution		Perpendicular section (case 2)		Parallel section (case 3)		Variation* (%)
	Load (kN)	Failure deflection (mm)	Load (kN)	Failure deflection (mm)	Load (kN)	Failure deflection (mm)	
S05/C	153.2	19.6	155.1	19.4	146.0	20.1	6.2
S06/B	159.3	19.5	160.6	19.5	157.8	19.3	1.8
S07/A	153.7	19.6	154.0	19.3	153.4	19.4	0.4
*Variation of load capacity of case 2 and case 3 model							

The punching shear capacity and failure deflection of different models of three beams were presented in Table 4.14 and Figure 4.48. Among three positions of casting, casting at position C at a corner of slab shows the biggest effect of changing fiber orientation, while there is no effect in the case casting at the center of the slab. It could be because casting at a corner gave the long distance to orient fiber in the slab.

In the case concrete casted at a corner of the slab, the change of punching shear capacity if fiber orientation coefficient increased and decreased along flow direction is 6.2 %. The slab with the decrease trend of fiber orientation factor according to fiber orientation of parallel sections induced more effect than the slab with the trend of increase. That change in the case of casting at a side or at the center of the slab are 1.8 and 0.4, respectively. When concrete casted at the center of slab, the load-deflection behaviors in two cases of increase and decrease fiber orientation factor seem to be similar to the case of random distribution of fiber. It means that casting at the center of slab induce no effect of fiber orientation, neither increase nor decrease punching shear capacity.

Note: "Perpendicular section" and "parallel section" is the model applied relation between fiber orientation and distance of perpendicular and parallel section, respectively.

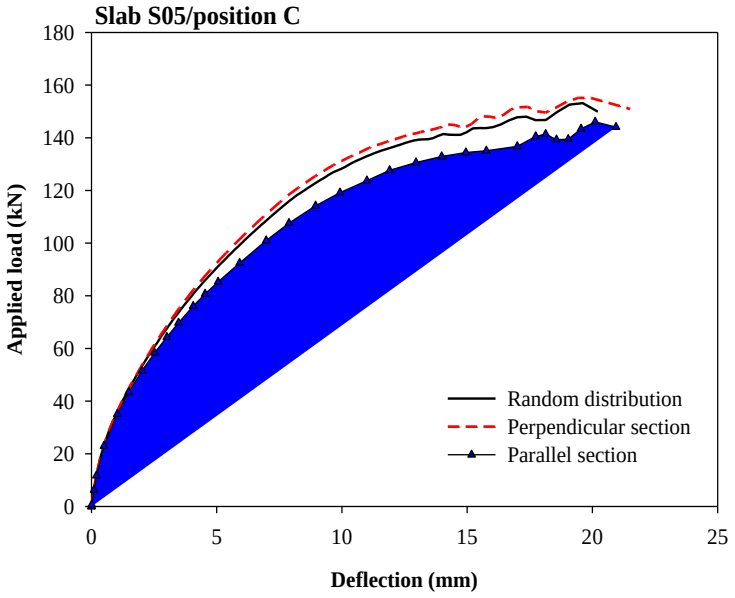

(a)

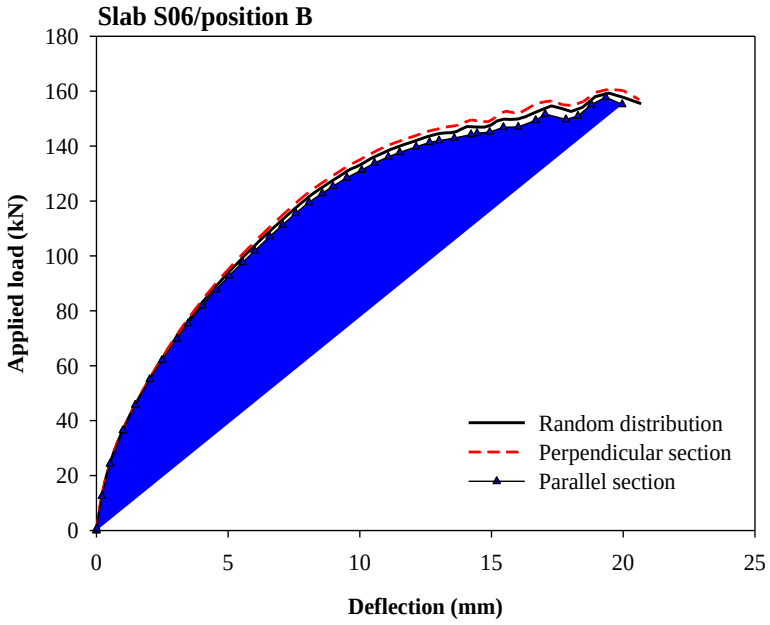

(b)

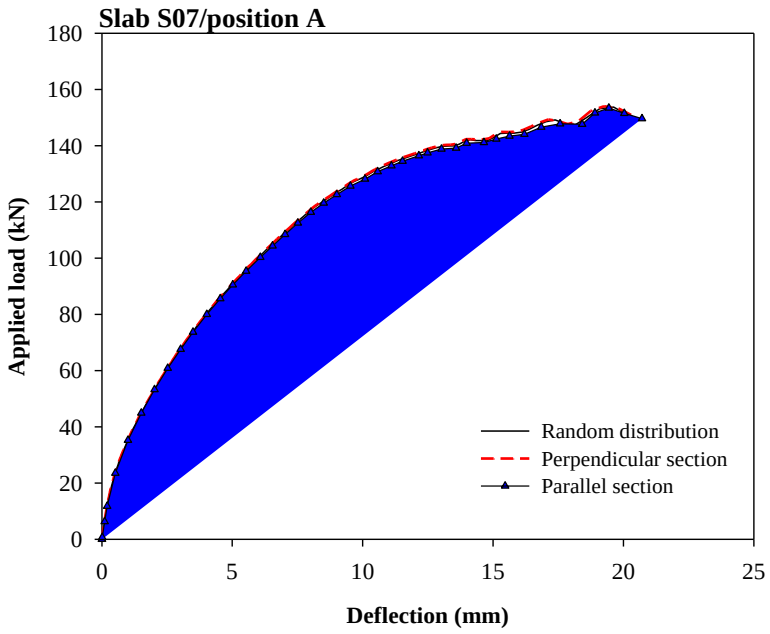

(c)

Figure 4.50: Comparison of effect of three trends of fiber orientation in the models of different casting positions: (a) Position C, (b) Position B, and (c) Position A

To highlight the effect of fiber orientation if changing casting position, the load-deflection response from two models of increase or decrease fiber orientation relation

were averaged, and the comparison among the three slabs were shown in Figure 4.51 as follows. The highest punching shear capacity is of the slab cast at the center, while slab cast at a corner shows the lowest capacity. This can be explained because the slab cast at a corner varied with the larger range of capacity and load-deflection behavior, therefore, the capacity is not stable.

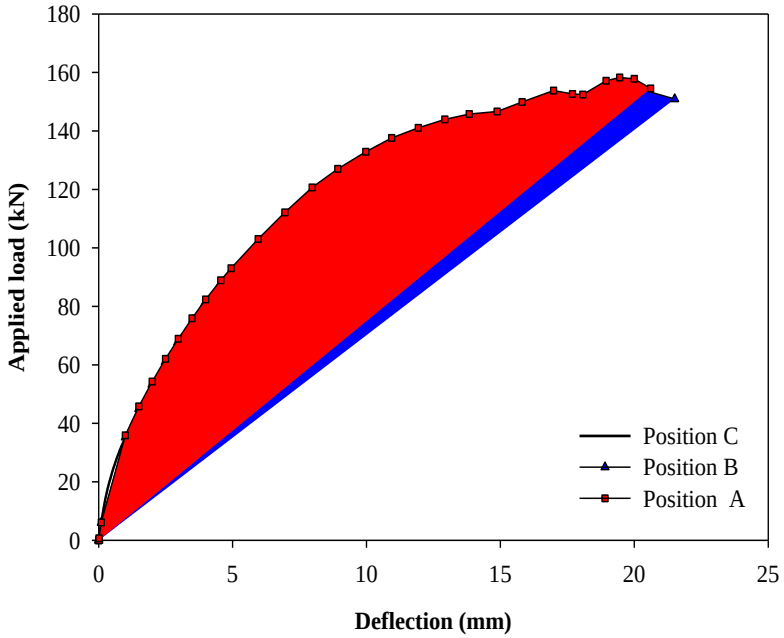

Figure 4.51: Comparison of effect of fiber orientation in three casting positions

4.5.3. The slabs with 0.8% fiber

By applying the same procedure as the previous models, the slabs with 0.8% of fiber were simulated to check the effect of fiber orientation if reducing fiber content. The material properties presented in previous part were also adopted. The agreement of FEA and experimental results were shown in Figure 4.52 as follows.

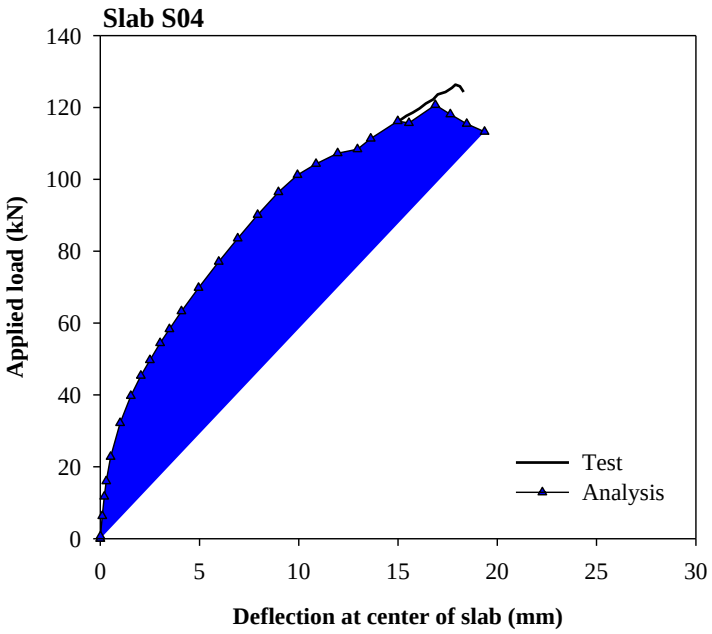

Figure 4.52: Comparison of load-deflection responses from experiment and analysis

FEA curve presents the higher stiffness comparing to experimental curve, but obtained ultimate load and displacement at moment of failure was similar. In the experiment, the slab failed at a load of 126.3 kN at the deflection of 17.9 mm, while the analysis slab failed at the load of 120.7 kN at the deflection of 16.9 mm. The difference in the ultimate loads is less than 5%.

In term of consideration fiber orientation effect, the slab was simulated for each position of casting, with different relationship between fiber orientation and the distance. Figure 4.53 shows the load-the center displacement from three slabs model of three casting positions: position A, B, and C. As same point from the models of beam with 1.6% of fiber, the highest effect of fiber orientation belongs to the slab cast at a corner, and the lowest effect is the slab cast at the center.

Note: “Perpendicular section” and “parallel section” in following figure is the model applied relation between fiber orientation and distance of perpendicular and parallel section, respectively.

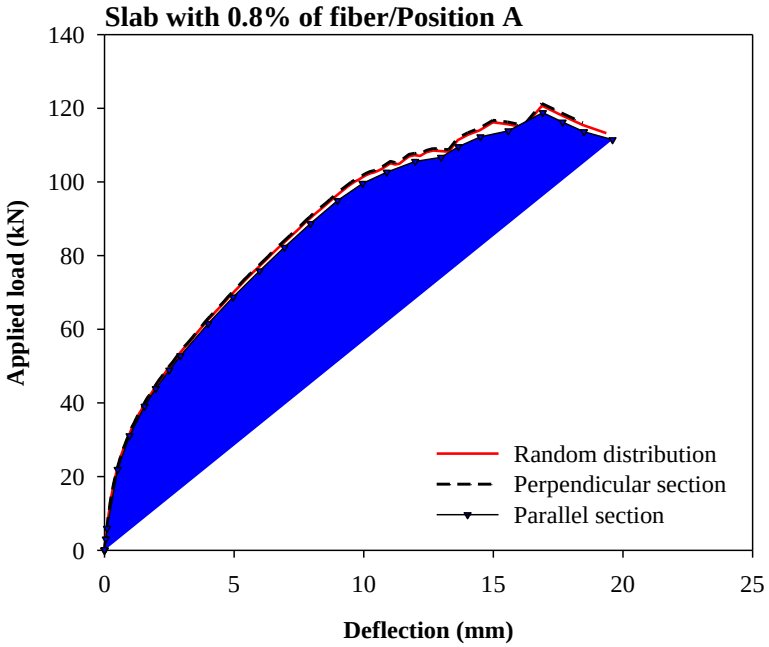
Slab with 0.8% of fiber/Position A
Applied load (kN)
Deflection (mm)
Random distribution
Perpendicular section
Parallel section

(a)

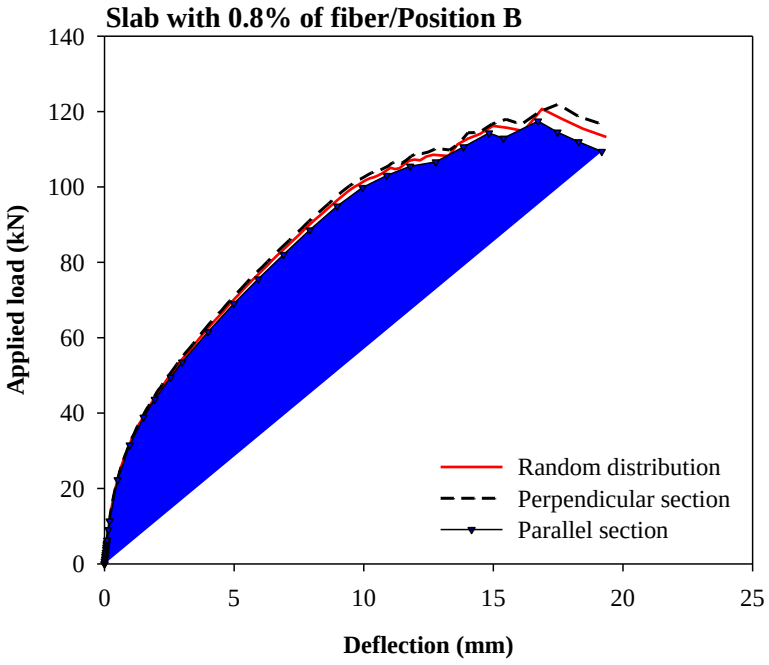
Slab with 0.8% of fiber/Position B
Applied load (kN)
Deflection (mm)
Random distribution
Perpendicular section
Parallel section

(b)

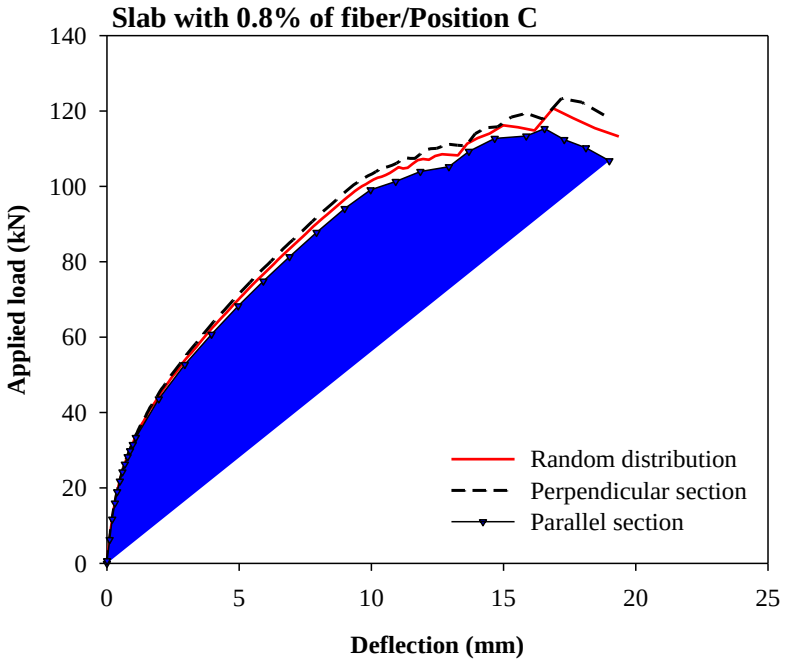

(c)

Figure 4.53: Comparison of effect of three trends of fiber orientation in the models of different casting positions: (a) Position C, (b) Position B, and (c) Position A

Table 4.15: Comparison of punching shear capacity and failure deflection between the models of different distributions of fiber of three slabs (0.8% of fiber)

Slab	Random distribution		Perpendicular section (case 2)		Parallel section (case 3)		Variation* (%)
	Load (kN)	Failure deflection (mm)	Load (kN)	Failure deflection (mm)	Load (kN)	Failure deflection (mm)	
S02/C	120.7	16.9	123.3	17.2	115.3	16.6	6.5
S03/B	120.7	16.9	121.9	17.5	117.5	16.7	3.6
S04/A	120.7	16.9	121.3	19.3	118.9	16.9	2.0
*Variation of load capacity of case 2 and case 3 model							

4.6. Parametric study

4.6.1. Changing the relation between fiber orientation and the distance

To consider the effect of fiber orientation, the relationships between fiber orientation were adopted from the study of Grunewald [64] that presented in the previous chapter. Those relations could change depending on many factors such as type of fibers, presence of steel bar, and flowable properties of the mix. With the purpose of figure out the whole picture of the fiber orientation effect if the relationship is changed, the other relationships would be proposed and applied to the FE model.

The maximum fiber orientation factor at the distance of 2.85 of section perpendicular to casting direction was assumed to be 1, as fibers perfectly orient along the casting direction. From previous chapter, the magnitude of slope of relationship line of cross-section parallel to casting direction was closed to that value of perpendicular section. Therefore, those value would be assumed to be similar in this part. The data of fiber orientation and the formula for its relation to distance from casting position were shown in Table 4.15 and Figure 4.54 for different cutting sections. The other material properties were similar to the previous analysis. The effect of fiber orientation of the slab S05 that cast at a corner is the most significant among the three slabs, therefore, in this part, the slab S05 was used for simulations.

Table 4.16: Assumed fiber orientation coefficient at different cutting sections

Parallel sections		Perpendicular sections	
Distance d (mm)	η	Distance d (mm)	η
0	0.707	0	0.707
3050	0.397	2800	1
$\eta = -10.19\times10^{-5}d + 0.707$		$\eta = 10.19\times10^{-5}d + 0.707$	

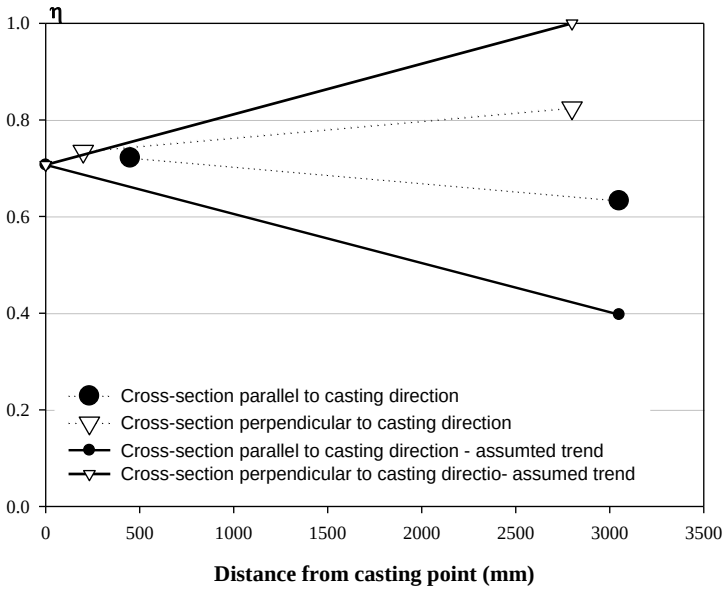

Figure 4.54: Fiber orientation in the beam at different distances from casting position: original trend and assumed trend

Table 4.15 and Figure 4.55 show the results from FEA, including the model of the slab of increase and decrease trend of fiber orientation. With the assumed relationship of fiber orientation and distance from casting position, the effect of fiber orientation is significant. The load-deflection behaviors of the two models seem to be similar in stage before cracks occur. After cracking, the load-displacement paths differ from each other, the model with the increasing trend of fiber orientation presents higher stiffness in this part. Both two model gave the same value of failure deflection. However, the difference of load capacity between the two models is 22 %, particularly is nearly 32 kN of applied load. It means that fiber orientation strongly effects to the behavior of the slabs in this particular relation with distance, such as load-deflection behavior and load capacity.

Figure 4.52 shows that those two load-displacement response could cover the responses plotted from the experiment of the three slabs. Therefore, these two models could be used to predict behavior of slabs, and give a good range for the change of load-deflection behavior and load capacity if casting position is changed.

Note: "Perpendicular section" and "parallel section" in following figure is the model applied relation between fiber orientation and distance of perpendicular and parallel section, respectively.

Table 4.17: Comparison of punching shear capacity and failure deflection between the models of different assumed distributions of fiber of the slab

Model	Perpendicular section	Parallel section	Variation (%)
Load (kN)	174.0	142.3	22.3
Failure deflection(mm)	22.6	23.0	1.8

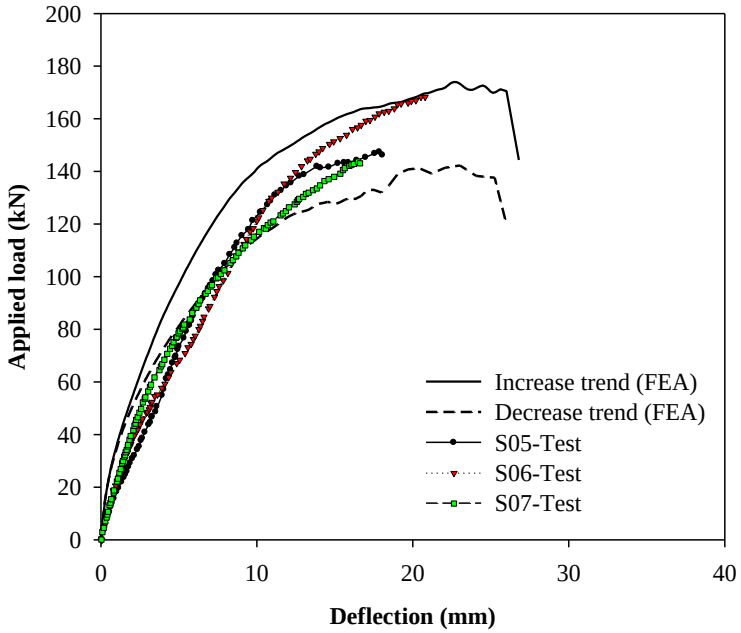

Figure 4.55: Load-deflection responses of FE models and experiment

4.6.2. Changing the size of the slab

To consider effect of fiber orientation in the case of realistic design of a flab slab, this part performed the study with the square slab with a size of 4000 mm and thickness of 100 mm to figure out the effect of fiber orientation in realistic structure. The full detail of slab dimensions and arrangement of tensile reinforcement are shown in Figure 4.56 as follows.

The relation of fiber orientation and distance from casting point was similar to the relation from Grunewald's research [64]. By applying same procedure as the previous part, the slab was simulated in ABAQUS in the case of casting at a corner of slab to consider effect of fiber orientation. The result was shown in Figure 4.57 and Table 4.18. In this designed slab, because of large width and length and small thickness, the slab failed under flexural mode, therefore, the slab induced the yield point and increased the failure deflection.

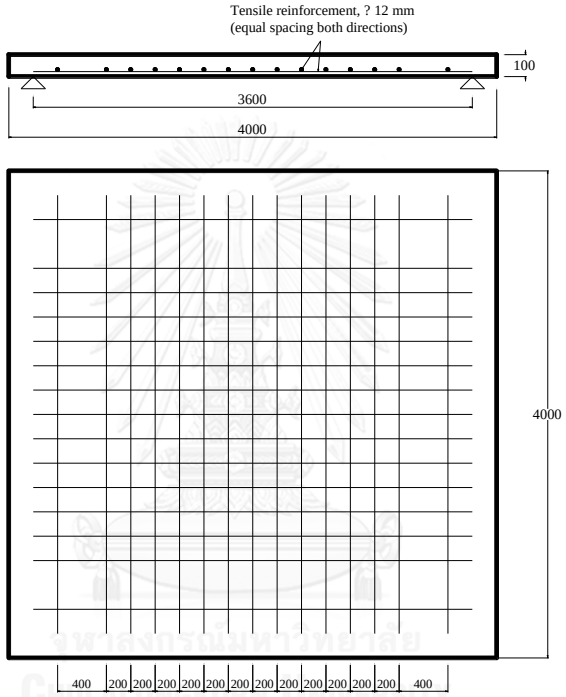

Figure 4.56: Design of the slab

In term of consideration of fiber orientation, due to larger size of slab induced higher distance from casting point corresponding to higher value of fiber orientation coefficient, the difference of material properties along casting direction are higher than the small slab from the previous part. From analysis results of the models with different trends of fiber orientation induced from fiber orientation of perpendicular section and parallel section, the difference in term of load capacity between 2 models is 44%. It shows that capacity of the slab with properties of perpendicular sections equal nearly two times the slab with properties of parallel sections. In conclusion, the effect of fiber orientation in this particular designed slab was very high. Casting as far from loading zone may induce high or very low load capacity of slab comparing to the

slab with random distribution of fiber. Therefore, it is better to cast concrete near by the loading zone to reduce effect of fiber orientation.

Table 4.18: Comparison of load capacity and failure deflection between the models of different distributions of fiber of the designed slab

Slab	Random distribution		Perpendicular section (case 2)		Parallel section (case 3)		Variation* (%)
	Load (kN)	Failure deflection (mm)	Load (kN)	Failure deflection (mm)	Load (kN)	Failure deflection (mm)	
S-/C	145.8	68	197.5	70.3	110.1	50.1	6.5
*Variation of load capacity of case 2 and case 3 model							

Note: "Perpendicular section" and "parallel section" in following figure is the model applied relation between fiber orientation and distance of perpendicular and parallel section, respectively.

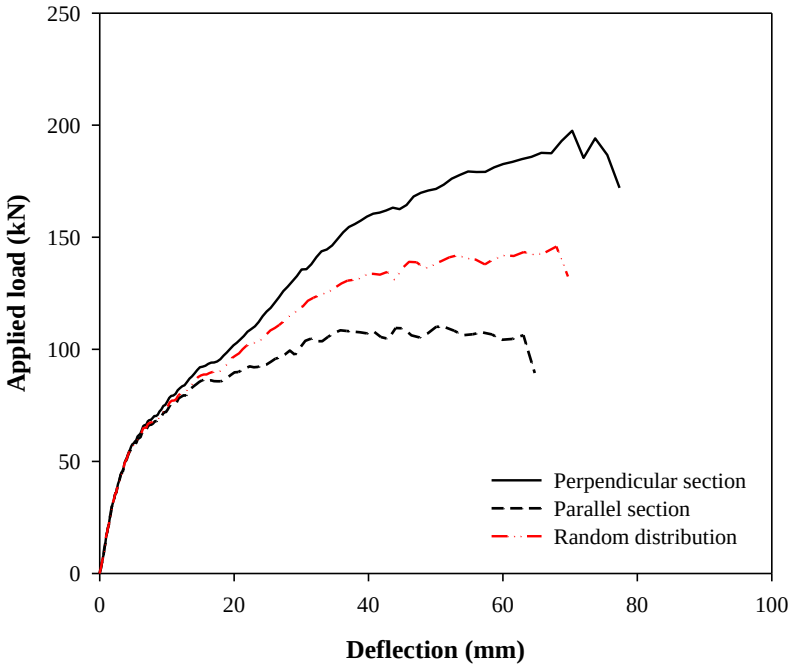

Figure 4.57: Load-deflection responses of three FE models

CHAPTER 5

CONCLUSIONS AND RECOMMENDATIONS

5.1. Conclusions

This thesis presents a study of finite element model of punching shear behavior of UHPFRC slab, combines with consideration of fiber orientation effect. Through the study, finite element analysis gives a good prediction of behavior of slab under concentrated loading, and shows the effect of fiber orientation in each position of casting, then can be used with confidence in practice. From analysis results, the following conclusion can be drawn:

1) The good agreement of analysis and experimental result of both the beam and slab demonstrates that the adopted material models used for analysis, including tensile and compressive behavior of concrete, and stress-strain response of steel reinforcement, are the reasonable models to represent behavior of UHPFRC material. These material model can be used in future for further analysis of UHPFRC structures.

2) In FEA of the slabs, the slab cast at a corner present the highest effect of changing fiber orientation, while the slab cast at the center is almost not affected. By applying two relationships between fiber orientation and distance from casting position, including increase and decrease fiber orientation along casting direction according to two models of one slab, the results give range of punching shear capacity if changing fiber orientation. The difference in ultimate load of two models of the slab cast at a corner is 6.2%, while that difference for the slab cast at a side or at the center of slab are just 1.8% and 0.4%, respectively. In the other view, if averaging load-deflection response from the two models, the slab cast at the center presents the stability of punching shear capacity when fiber orientation is changed, comparing to the other positions.

3) With the different fiber content, particularly 0.8% of fiber, the effect of fiber orientation is similar to the slab of 1.6% of fiber, therefore, with using low volume of fiber, the effect of fiber orientation should be similar.

4) Parametric study gives a sense of effect of fiber orientation in a critical case of fiber distribution and with the particular size of slab. By changing the fiber orientation along casting point from original case of Grunewald, the variation of punching shear strength is up to 22.3%. By increase the size of slab to the width of 4000 mm, the difference of load capacity of two critical case is up to 44.3%. Therefore, in application of real structure, the UHPFRC material should not cast at far from the loading zone.

5.2. Recommendations for future works

Regarding the result of this study, the following points are recommended for future research:

1) The direct tensile test for UHPFRC material: there is the high dependence of mixture on tensile strength of UHPFRC material, therefore, the direct tensile test should be performed for each mix of material to apply to finite element model.

2) Study effect of fiber orientation on flexural structures: this study investigated the effect of fiber orientation on punching shear behavior of slab, afterward, the study on flexural structure should be conducted to figure out general view of this effect.

3) Study effect of fiber orientation with changing size of flat slab, or other slab structure: the work can clearly be extended to the analysis of the other dimension of slab or the other slab with different boundary condition.

4) Study in slab with high volume of fiber: this study gave a sense of fiber orientation effect of slab with low volume of fiber, then in future research, this effect of slab with high volume of fiber should be worked out.

REFERENCES

1. Habel, K., *Structural behaviour of elements combining ultra-high performance fibre reinforced concretes (UHPFRC) and reinforced concrete.* 2004.
2. Richard, P. and M. Cheyrezy, *Composition of reactive powder concretes.* Cement and concrete research, 1995. **25**(7): p. 1501-1511.
3. Spasojevic, A., *Structural implications of ultra-high performance fibre-reinforced concrete in bridge design.* 2008.
4. Carreira, D.J. and K.-H. Chu. *Stress-strain relationship for plain concrete in compression*. in *ACI Journal proceedings*. 1985. ACI.
5. Ezeldin, A.S. and P.N. Balaguru, *Normal-and High-Strength Fiber-Reinforced Concrete under Compression.* Journal of materials in civil engineering, 1992.
6. Hsu, L.S. and C.T. Hsu, *Stress-strain behavior of steel-fiber high-strength concrete under compression.* ACI structural journal, 1994. **91**(4).
7. Mansur, M., M. Chin, and T. Wee, *Stress-strain relationship of high-strength fiber concrete in compression.* Journal of materials in civil engineering, 1999. **11**(1): p. 21-29.
8. Nataraja, M., N. Dhang, and A. Gupta, *Stress–strain curves for steel-fiber reinforced concrete under compression.* Cement and concrete composites, 1999. **21**(5): p. 383-390.
9. Barros, J.A. and J.A. Figueiras, *Flexural behavior of SFRC: testing and modeling.* Journal of materials in civil engineering, 1999. **11**(4): p. 331-339.
10. Committee, A. *Building code requirements for structural concrete (ACI 318-05) and commentary (ACI 318R-05)*. 2005. American Concrete Institute.
11. 363, A.C. *State of the Art Report on High-Strength Concrete*. in *ACI Journal Proceedings*. 1984. ACI.
12. Ma, J., et al. *Comparative investigations on ultra-high performance concrete with and without coarse aggregates*. in *Proceedings International Symposium on Ultra High Performance Concrete (UHPC), Kassel, Germany*. 2004.

13. Graybeal, B.A., *Compressive behavior of ultra-high-performance fiber-reinforced concrete.* ACI Materials Journal, 2007. **104**(2).
14. Ozyildirim, C. *Evaluation of Ultra-high-performance Fiber-reinforced Concrete*. 2011.
15. Eldin, H.K.S., et al., *Mechanical Properties ofUltra-High Performance Fiber Reinforced Concrete.* 2004.
16. Wille, K. and A. Naaman. *Fracture energy of UHPFRC under direct tensile loading*. in *FraMCoS-7 international conference, Jeju, Korea*. 2010.
17. Wille, K., S. El-Tawil, and A. Naaman, *Properties of strain hardening ultra high performance fiber reinforced concrete (UHP-FRC) under direct tensile loading.* Cement and Concrete Composites, 2014. **48**: p. 53-66.
18. Markovic, I., *High-performance hybrid-fibre concrete: development and utilisation*. 2006, TU Delft, Delft University of Technology.
19. Wille, K., D.J. Kim, and A.E. Naaman, *Strain-hardening UHP-FRC with low fiber contents.* Materials and Structures, 2011. **44**(3): p. 583-598.
20. Park, S.H., et al., *Tensile behavior of ultra high performance hybrid fiber reinforced concrete.* Cement and Concrete Composites, 2012. **34**(2): p. 172-184.
21. Rilem, T., *162-TDF. Test and design methods for steel fibre reinforced concrete.* Materials and structures, 2002. **35**: p. 579-582.
22. Naaman, A. and H. Reinhardt, *Proposed classification of HPFRC composites based on their tensile response.* Materials and structures, 2006. **39**(5): p. 547-555.
23. Stang, H., *Evaluation of properties of cementitious fiber composite materials.* High Performance Fibre Reinforced Cement Composites, 1992. **1**: p. 388-406.
24. Kang, S.-T. and J.-K. Kim, *The relation between fiber orientation and tensile behavior in an Ultra High Performance Fiber Reinforced Cementitious Composites (UHPFRCC).* Cement and Concrete Research, 2011. **41**(10): p. 1001-1014.
25. Lataste, J.-f., S.J. Barnett, and T. Parry, *Determination of fibres orientation in UHPFRC and evaluation of their effect on mechanical properties.*

26. Gettu, R., et al., *Study of the distribution and orientation of fibers in SFRC specimens.* Materials and Structures, 2005. **38**(1): p. 31-37.
27. Şanal, İ. and N.Ö. Zihnioğlu, *To what extent does the fiber orientation affect mechanical performance?* Construction and Building Materials, 2013. **44**: p. 671-681.
28. Sebaibi, N., M. Benzerzour, and N.E. Abriak, *Influence of the distribution and orientation of fibres in a reinforced concrete with waste fibres and powders.* Construction and Building Materials, 2014. **65**: p. 254-263.
29. Soroushian, P. and C.-D. Lee, *Distribution and orientation of fibers in steel fiber reinforced concrete.* ACI Materials Journal, 1990. **87**(5).
30. Van Mier, J., et al., *FIBER ORIENTATION IN ULTRA HIGH PERFORMANCE FIBER REINFORCED CONCRETE AND ITS VISUALIZATION.*
31. Ferrara, L., N. Ozyurt, and M. Di Prisco, *High mechanical performance of fibre reinforced cementitious composites: the role of "casting-flow induced" fibre orientation.* Materials and Structures, 2011. **44**(1): p. 109-128.
32. Barnett, S.J., et al., *Assessment of fibre orientation in ultra high performance fibre reinforced concrete and its effect on flexural strength.* Materials and Structures, 2010. **43**(7): p. 1009-1023.
33. C. Li, V., *Postcrack scaling relations for fiber reinforced cementitious composites.* Journal of Materials in Civil Engineering, 1992. **4**(1): p. 41-57.
34. Li, V.C., H. Stang, and H. Krenchel, *Micromechanics of crack bridging in fibre-reinforced concrete.* Materials and structures, 1993. **26**(8): p. 486-494.
35. Li, V.C., Y. Wang, and S. Backer, *A micromechanical model of tension-softening and bridging toughening of short random fiber reinforced brittle matrix composites.* Journal of the Mechanics and Physics of Solids, 1991. **39**(5): p. 607-625.
36. S. Delsol, J.-P.C. *Numerical modeling of UHPFRC mechanical behavior based on fibre orientation*. in *RILEM-fib-AFGC International Symposium on Ultra-High Performance Fibre-Reinforced Concrete*. 2014.

37. Wuest, J., E. Denarié, and E. Brühwiler. *Model for predicting the UHPFRC tensile hardening response*. in *Second International Symposium on Ultra High Performance Concrete*. 2008. University of Kassel.

38. Wuest, J., *Comportement structural des bétons de fibres ultra performants en traction dans des éléments composés.* 2007.

39. Frettlöhr, B., *Bemessung von Bauteilen aus ultrahochfestem Faserfeinkornbeton (UHFFB)*. 2011, Universität Stuttgart.

40. Frettlöhr, B. *Theoretical model for size and shape effect of UHPFRC in flexural tension considering tensile behaviour influenced by fibre orientation*. in *RILEM-fib-AFGC International Symposium on Ultra-High Performance Fibre-Reinforced Concrete*. 2013.

41. Kinnunen, S. and H. Nylander, *Punching of concrete slabs without shear reinforcement*. 1960: Elander.

42. Muttoni, A., *Punching shear strength of reinforced concrete slabs without transverse reinforcement.* ACI Structural Journal, 2008. **105**(EPFL-ARTICLE-116123): p. 440-450.

43. Muttoni, A. and M. Fernández Ruiz, *MC2010: The Critical Shear Crack Theory as a mechanical model for punching shear design and its application to code provisions.* fib Bulletin, 2010. **57**: p. 31-60.

44. Narayanan, R. and I. Darwish, *Punching shear tests on steel-fibre-reinforced micro-concrete slabs.* Magazine of Concrete Research, 1987. **39**(138): p. 42-50.

45. Harajli, M., D. Maalouf, and H. Khatib, *Effect of fibers on the punching shear strength of slab-column connections.* cement and concrete composites, 1995. **17**(2): p. 161-170.

46. Higashiyama, H., A. Ota, and M. Mizukoshi, *Design equation for punching shear capacity of SFRC slabs.* International Journal of Concrete Structures and Materials, 2011. **5**(1): p. 35-42.

47. Genikomsou, A.S. and M.A. Polak, *Finite element analysis of punching shear of concrete slabs using damaged plasticity model in ABAQUS.* Engineering Structures, 2015. **98**: p. 38-48.

48. Negele, A., et al., *Finite-element simulations on punching tests of shear-retrofitted slab-column connections.* Fracture Mechanics of Concrete and Concrete Structures, 2007: p. 911-918.

49. Polak, M.A., *Modeling punching shear of reinforced concrete slabs using layered finite elements.* ACI structural Journal, 1998. **95**(1).

50. Vacev, T., et al., *Testing and finite element analysis of reinforced concrete column footings failing by punching shear.* Engineering Structures, 2015. **92**: p. 1-14.

51. Wosatko, A., J. Pamin, and M.A. Polak, *Application of damage–plasticity models in finite element analysis of punching shear.* Computers & Structures, 2015. **151**: p. 73-85.

52. Teixeira, M.D., et al., *Numerical simulation of the punching shear behaviour of self-compacting fibre reinforced flat slabs.* Construction and Building Materials, 2015. **74**: p. 25-36.

53. Ragab, K.S., *Study Punching Shear of Steel Fiber Reinforced Self Compacting Concrete Slabs by Nonlinear Analysis.* World Academy of Science, Engineering and Technology, 2013.

54. Alam, A. and K.M. Amanat, *Finite Element Simulation on Punching Shear Behavior of Reinforced Concrete Slabs.* ISRN Civil Engineering, 2012. **2012**.

55. William, K. and E. Warnke, *Constitutive model for the triaxial behavior of concrete.* 1975.

56. Lubliner, J., et al., *A plastic-damage model for concrete.* International Journal of solids and structures, 1989. **25**(3): p. 299-326.

57. Lee, J. and G.L. Fenves, *Plastic-damage model for cyclic loading of concrete structures.* Journal of engineering mechanics, 1998. **124**(8): p. 892-900.

58. Barros, J.A., et al., *Post-cracking behaviour of steel fibre reinforced concrete.* Materials and Structures, 2005. **38**(1): p. 47-56.

59. Simulia, D., *Abaqus 6.13 User's Manual.* Dassault Systems, Providence, RI, 2013.

60. PANSUK, W., *Shear Capacity of RC and Ultra High Strength Fiber Reinforced Concrete Flanged Beams*, in *Division of Structural and Geotechnical Engineering*. 2007, Hokkaido University.

61. Wang, T. and T.T. Hsu, *Nonlinear finite element analysis of concrete structures using new constitutive models.* Computers & structures, 2001. **79**(32): p. 2781-2791.

62. Belarbi, A., L. Zhang, and T.T. Hsu. *Constitutive Laws of Reinforced Concrete Membrane Elements*. in *Eleventh World Conference of Earthquake Engineering*. 1996.

63. Stang, H., V.C. Li, and H. Krenchel, *Design and structural applications of stress-crack width relations in fibre reinforced concrete.* Materials and Structures, 1995. **28**(4): p. 210-219.

64. Grünewald, S., *Performance-based design of self-compacting fibre reinforced concrete*. 2004: TU Delft, Delft University of Technology.

65. Thanh, T.N., *EFFECTS OF CASTING DIRECTION ON PUNCHING SHEAR STRENGTH OF ULTRA HIGH PERFORMANCE FIBER REINFORCED CONCRETE SLABS*, in *Department of Civil Engineering, Faculty of Engineering*. 2014, Chulalongkorn University.

66. Lim, B.T., *Punching shear capacity of flat slab-column junctions (a study by 3-D non-linear finite element analysis)*. 1997, University of Glasgow.

67. Tanikella, P., R. Gettu, and R. Gettu. *On the distribution of fibers in self compacting concrete*. in *7th RILEM Symposium on Fibre-Reinforced Concretes-BEFIB, RILEM Publications SARL Chennai, India*. 2008.

APPENDIX

VITA